Remote sensing of atmospheric water vapor over land areas using MERIS measurements and application to numerical weather prediction model validation

DISSERTATION

zur Erlangung des akademischen Grades eines
Doktors der Naturwissenschaften
am Fachbereich für Geowissenschaften
der Freien Universität Berlin

vorgelegt von

RONNY LEINWEBER

June 22, 2010

1. Gutachter: Prof. Dr. Jürgen Fischer

2. Gutachter: Prof. Dr. Ralf Bennartz

Tag der Disputation: 18. Juni 2010

Contents

1 Introduction

Climate change has been described as one of the most pressing challenges to humankind in this century. It has been widely discussed in the political and scientific society. The most important and well known aspect of climate change is global warming. Global warming is defined as the increase in the average temperature of air near the Earth's surface and the oceans since the mid 20th century, and its projected continuation. The Intergovernmental Panel on Climate Change IPCC (2007) report documented a global surface temperature increase of 0.74 ± 0.18 °C between the start and the end of the 20th century. The IPCC concludes that most of the observed temperature increase was caused by an amplification of the natural greenhouse effect called the anthropogenic/enhanced greenhouse effect.

The natural greenhouse effect is a natural process that aids in heating the Earth's surface and atmosphere. It results from the fact that the atmosphere is relatively transparent to solar radiation, but highly opaque to thermal radiation. About 50% of the solar radiation is absorbed at the Earth's surface, the rest is reflected or absorbed by the atmosphere. The absorbed energy warms the surface, leading to thermal radiation. Greenhouse gases in the atmosphere that are transparent to incoming solar radiation but more absorbent to thermal radiation, absorb and re-radiate the thermal radiation in all directions, both upwards and downwards. This results in an increasing warming of lower atmospheric layers. Without the greenhouse effect the Earth's average global temperature would be -18° Celsius, rather than the present 15° Celsius.

During the industrial revolution, atmospheric concentrations of carbon dioxide began to rise. Due to increasing world industrialization in the 21st century, this trend is likely to continue (Nakicenovic et al., 2000). Changes in the atmospheric composition, especially for greenhouse gases like water vapor (H_2O), carbon dioxide (CO_2) and methane (CH_4), can enhance the natural greenhouse effect. It is a stated fact that it results in net warming of the earth's atmosphere (anthropogenic/enhanced greenhouse effect). The primarily contributors of the greenhouse effect are not the main constituents of the atmosphere like nitrogen (N_2) and oxygen (O_2), but rather greenhouse gases like water vapor and carbon dioxide, which are less than 1% of global air mass. Despite its very small volume,

water vapor is the most important gaseous source of infrared opacity in the atmosphere, accounting for about 60% of the natural greenhouse effect for clear skies (Kiehl and Trenberth, 1997).

Water inhabits the Earth's atmosphere in all three possible phases: solid (ice), liquid (water droplets), and gas (water vapor). Water vapor is continuously produced in the atmosphere from the evaporation of liquid water and from the sublimation of ice, and it is continuously removed by condensation processes. The condensation of water vapor is responsible for cloud development and precipitation (Ramanathan et al., 1989). In the lower troposphere, condensation of water vapor into precipitation provides latent heating which dominates the structure of tropospheric diabatic heating (Trenberth and Stepaniak, 2003).

Imperfect understanding of feedback processes is a major cause of uncertainties about global warming. Open questions in the current scientific community are the feedback processes of water vapor, clouds and aerosols to global warming. Soden et al. (2002); IPCC (2001) stated the important role of water vapor due to it's strong feedback mechanisms for global warming. Water vapor is dependent on temperature for its amount. The increase of other greenhouse gases like carbon dioxide raises the temperature, leading to more evaporation. Consequently the atmospheric water vapor amount is enhanced. The increased atmospheric water vapor further absorbs heat, and raises the temperature again. This is the direct positive feedback process of water vapor. Additionally more water vapor in the atmosphere could tend to an increased development of clouds. Some clouds absorb and emit infrared radiation and thus generate the indirect positive feedback effect of water vapor. But the contribution of water vapor to this process is hard to quantify because other parameters (aerosols, thermodynamical processes and micro physics) are also involved. Moreover there are also clouds that reflects more solar radiation back to space leading to an indirect negative feedback effect of water vapor.

Therefore water vapor plays a major role in the weather, the Earth climate, and the energy transfer. Due to its important role in the energy balance of the Earth, and thus the general circulation of the atmosphere system (Starr and Melfi, 1991), it is important that water vapor is closely monitored. Water vapor is, however, highly variable, and this makes the task of monitoring it quite challenging. The complex spatial distribution of tropospheric water vapor is determined by the local hydrological cycle, via evaporation, condensation and precipitation, and by large scale advective transport processes (Liou, 2002). Therefore, frequently sampled, accurate, measurements with high spacial resolution and world wide coverage are needed.

On a global scale, water vapor is retrieved using diverse remote sensing techniques.

Since the 1960s, when satellite remote sensing of the Earth's atmosphere began, the geographical patterns of water vapor have been continuously observed over large areas or even the whole globe. Today, operational satellite based remote sensing of water vapor is used to study weather and climate (Trenberth et al., 2005; Vonder Haar et al., 2005). Most of the analysis have focused on water vapor trends, processes, and interactions, in order to improve the understanding of the important role played by water vapor in the climate system.

The different remote sensing techniques available are based on nadir (downward looking) or limb geometries; as well as geostationary or sun-synchronous, near-polar orbits. Instruments of most interest for water vapor are passive imagers. Passive methods for retrieving atmospheric water vapor exploit the water vapor absorption and emissions bands in the visible (VIS), the infrared (IR) including the near and thermal infrared (NIR, TIR), and the microwave (MW) spectral range[1].

Microwave techniques (MW) typically exploit water vapor absorption lines around 23GHz and 30GHz, and have the advantage that they are not affected by clouds, in contrast to methods in other spectral ranges. However, for accurate water vapor measurements, microwave retrievals are limited to low emissivity water surfaces (Schluessel and Emery, 1990). Examples for MW satellite instruments for water vapor retrieval are the passive Special Sensor Microwave Imager SSM/I and the Advanced Microwave Sounding Unit (AMSU). The accuracy of the retrieval was estimated by comparison with radiosondes performed by Sohn and Smith (2003). They found for a seasonal scale of three month mean difference between SSM/I and radiosondes of 1.0mm bias and a root mean error of 2.5mm. AMSU observations are operational and continuous. It flies on the NOAA KLM and N satellites as well as NASA's Aqua and SSM/I on-board the Defense Meteorological Satellite Program (DMSP) series of polar orbiting satellites.

Methods exploiting the TIR spectral range use the absorption and emission bands of water vapor between 6.5μm and 14μm. One example is the High Resolution Infrared Sounder HIRS-4, a polar orbiting IR-MW sensor on board the NOAA satellites. The accuracy of methods in the TIR depends on the knowledge of the Earth surface emissivity. The Surface emission largely depends on soil type, conditions (wet or dry) and coverage (vegetation). It can undergo large diurnal and regional variations. Therefore inaccuracies for methods using this spectral range, arise due to the required estimation of temperature and water vapor profiles as well as surface temperature (Gao et al., 1993). Another TIR instrument for the retrieval of atmospheric water besides HIRS is the Spinning Enhanced Visible and Infrared Imager (SEVIRI) on board the geostationary satellite Meteosat

[1] spectral regions: VIS 0.4-0.7μm; NIR 0.7-4μm and TIR 4-50μm

Second Generation (MSG-8). It allows the retrieval of the atmospheric water vapor with a very high temporal resolution of 15 minutes, allowing the study of atmospheric dynamics. However, there are similar restrictions as for the HIRS instrument.

Finally, methods based on back scattered solar radiation in the near infrared (NIR) that rely on the absorption in the $\rho\sigma\tau-$water vapor absorption band between about 0.9μm and 1.0μm (Gao and Kaufman, 2003; Fischer and Bennartz, 1997; Fischer, 1988). The method applied is the differential absorption technique. This technique uses a ratio of radiances between neighboring wavelengths, of which one is located in the water vapor absorption band and the other in a window band. In contrast to the microwave and thermal spectral range, the radiation in the NIR spectral range is not affected by surface emissivity, but it is affected by clouds, aerosols and the surface albedo. Regardless of this, the differential absorption technique is a particularly accurate method for the retrieval of water vapor over cloud free land areas.

While water vapor differential absorption lidars, which are active instruments, have only reached demonstration stage, a number of passive working radiometers are actually in space. These instruments are the Medium Resolution Imaging Spectrometer (MERIS) on board the European satellite ENVISAT and the Moderate Resolution Imaging Spectrometer (MODIS) on board the Terra and Aqua satellites.

Due to the important role of water vapor in the weather, the Earth climate, and the energy transfer, it is one of the key variables in a whole set of prognostic variables in numerical weather prediction (NWP) models as well for climate models. The quality of today's numerical weather prediction systems is driven by the quality of data that is used to determine the present state of the atmosphere and the quality of the representation of physical processes in the model (Bauer et al., 2007). The Deutsche Wetterdienst (DWD) uses the 1D-Var and nudging assimilation method for the regional NWP models COSMO-DE and COSMO-EU. The Deutsche Wetterdienst experimentally assimilates GPS water vapor measurements directly data into the regional NWP models. Water vapor has a very high temporal and spatial variability. Therefore accurate measurements in high temporal and spacial resolution are essential for the initialization of NWP models leading to the necessity of accurate global monitoring of water vapor from satellites. Additionally, satellite based observations are used to verify the forecast accuracy of NWP models. The validation also includes the verification of the quality of representation of physical processes within the model system. For the validation independent water vapor data is needed.

This work presents the development and the extensive validation of an advanced water vapor retrieval from MERIS observations, as well as its application to regional NWP

model validation. Chapter 2 of this thesis discusses the fundamentals of radiative transfer in relation to water vapor in the Earth's atmosphere. Chapter 3 comprises all the data used within this study; i.e., MERIS instrument and regional NWP models. In chapter 4 the focus is on the development of the enhanced algorithm for the retrieval of atmospheric water vapor over cloud-free land areas from MERIS satellite measurements. Key of the extended algorithm is the consideration of the variability of the spectral Earth surface albedo, which is the major improvement compared to the former algorithm (Albert, 2005; Fischer and Bennartz, 1997). The water vapor algorithm is validated with the in situ datasets of GPS, microwave radiometer and radio sounding, for a multi year period. The validation results are presented in chapter 5. The new water vapor product is then used to evaluate the water vapor analyses of the two NWP models COSMO-DE and COSMO-EU. Chapter 6 presents the results of the 3 and 4.5 years intercomparisons in which the new water vapor product serves as independent validation data. This work closes with with a summary and an outlook. The application of the new water vapor retrieval within the standard ESA MERIS processing is discussed, as well as its potential implementation in NWP model assimilation systems.

2 Fundamentals

2.1 Radiative quantities and radiative transport equation

All remote sensing techniques for atmospheric properties are based on the modification of radiation by different atmospheric constituents. When electromagnetic radiation passes through matter its intensity and spectral composition is modified by absorption, emission and scattering. Absorption and scattering describes the attenuation of radiation by matter absorbing photons and scattering photons out of their direct path, respectively.

One can characterize the relative contributions of scattering and absorption to the total extinction k_e by considering the extinction coefficient to be the sum of the absorption coefficient k_a and the scattering coefficient k_s, with dimension [length^{-1}] or [mass^{-1}].

$$k_e = k_a + k_s \tag{2.1.1}$$

It has to be noted that all radiative quantities described in this chapter are monochromatic, spectral dependent quantities in term of wavelength. The extinction of the monochromatic radiation L along its infinitesimal path ds can therefore be described by:

$$dL = -k_e L ds \tag{2.1.2}$$

L is the spectral radiance, which is the energy per unit area, unit solid angle, and spectral unit in [W/m^{2}sr nm]. In order to describe the extinction over an extended path between points s_1 and s_2, we integrate 2.1.2. This equation gives a general form of Beer´s law.

$$L(s_2) = L(s_1) exp[-\int_{s_1}^{s_2} k_e(s) ds] \tag{2.1.3}$$

From Beer´s law, also referred as the Lambert-Bouguer law, follow several important definitions. The integral quantities inside the brackets define the optical depth or τ of the medium along a path:

$$\tau(s_1, s_2) = \int_{s_1}^{s_2} k_e(s)ds, \tag{2.1.4}$$

The transmittance T between s_1 and s_2 is defined by the exponent of the of the optical path τ:

$$T = e^{-\tau(s_1,s_2)}. \tag{2.1.5}$$

The transmittance is a dimensionless quantity ranging from zero ($\tau \to \propto$) to one ($\tau \to 0$). For reasons of energy conservation, attenuation has to be balanced by sources of radiation. Setting a source term J, that define the sources of radiation into Eq. 2.1.2 leads to the differential radiative transfer equation (RTE)

$$\frac{dL}{k_e ds} = \frac{dL}{d\tau} = -L + J. \tag{2.1.6}$$

The integral form of the radiative transport equation is given by:

$$L(\tau) = L(0)e^{-\tau} + \int_0^{\tau} J(\tau')e^{-\tau'}d\tau'. \tag{2.1.7}$$

The source term J applies the multiple scattering source term J_{MS}, the single scattering term J_{SS} and the emission term J_{EM}:

$$J = J_{MS} + J_{SS} + J_{EM} \tag{2.1.8}$$

J_{MS} results from multiple scattered radiation and J_{SS} from the single scattered radiation. The thermal emission term J_{EM} can be expressed by the product of the emissivity and the Planck function:

$$J_{EM} = \epsilon_\lambda B_\lambda(T) \tag{2.1.9}$$

with ϵ_λ is the emissivity of the atmospheric matter or of the soil and B_λ the monochromatic Planck function that represents the thermal emission of a black body at the temperature T:

$$B_\lambda(T) = \frac{2hc^2}{\lambda^5} \frac{1}{e^{\frac{hc}{\lambda kT}} - 1} \tag{2.1.10}$$

where h and k denotes the Planck´s and Boltzmann´s constant, c the speed of light and λ the wavelength.

A complete description of interaction between radiation and matter is only possible by considering polarization. However in this work, radiation is only discussed in terms

of scalar intensity. It is a good approximation to most tasks in radiative transfer and modeling and atmospheric remote sensing.

2.2 Composition of the Earth's atmosphere

The Earth's atmosphere consists of four different main layers according to their thermal state. The lowest layer, the troposphere is characterized by a decreasing temperature up to the tropopause (~ 8 - 15km) with respect to height. It is followed by the stratosphere that is characterized by an increase of temperature up to 50km due to very strong ozone absorption. Between around 50 - 90km altitude, in the so called mesosphere, the temperature decreases again. The most upper layer in the atmosphere is the thermosphere. The temperatures in the thermosphere reaches up to 2000K caused by absorption of ultraviolet and X-ray radiation.

Also pressure, density and chemical composition have a vertical structure. Due to gravity, the pressure and air density decrease exponential with height.

$$p(z) \approx p(z_0) \exp(-(z - z_0)/H) \tag{2.2.1}$$

where H is the scale height in the atmosphere (6-8km).

The atmosphere is a mixture of several gases. Its main constituents are nitrogen (78%), oxygen (21%) and argon (0.9%). In contrast carbon dioxide (0.03%) and water vapor (0 - 0.04%) together accounting only 0.07% of the air´s volume. In fact, the so called permanent gases, such as nitrogen and oxygen alone are responsible for approximately 99% of the total mass and nearly unvarying concentrations, such that partial density and pressure follow Eq. 2.2.1. Many others gases like water vapor, carbon dioxide, methane and ozone are only present in trace amounts but can vary widely from one time and location to another. Many of these constituents have a disproportionally large influence on atmospheric transmittance and thus for atmospheric radiation, a fact that has implications for climate variability.

2.3 Water vapor in the atmosphere

Water vapor is the major radiative and dynamic element in the Earth's atmosphere. It is part of the hydrological cycle. The water vapor concentration varies significantly with time and space. Under typical atmospheric conditions, water vapor is continuously generated by evaporation and the sublimation of ice and removed by condensation. The

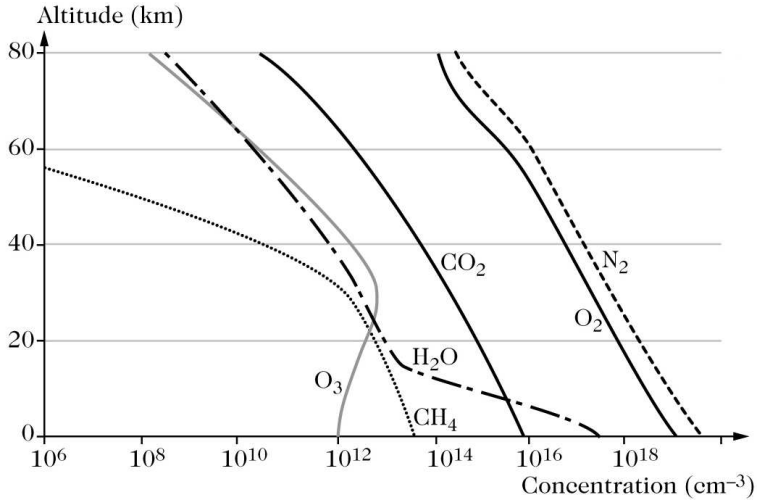

Figure 2.3.1: Typically vertical distribution of atmospheric constituents: water vapor (H_2O), methane (CH_4), ozone (O_3), carbon dioxide (CO_2), oxygen (O_2) and nitrogen (N_2) in $[\frac{molecules}{cm^3}]$ (Delmas et al. (2005))

condensation of water vapor to liquid or ice is responsible for the developments of clouds and therefore for rain, snow, and other precipitation.

Approximately 99.13% of water vapor is located in the troposphere. The vertical structure of water vapor is dominated by an almost exponential decrease along with pressure. Figure 2.3.1 show the vertical profile of water vapor and other atmospheric gases in the troposphere and stratosphere. More than 50% of water vapor is concentrated in the boundary layer below a pressure level of 850hPa (~1.5km) while more than 90% is confined over the 500hPa pressure level (~6.2km) (Liou, 2002). The global distribution of water vapor over ocean is shown in Figure 2.3.2 (left). High water vapor values are shown in the tropics and low water vapor is observable in the polar regions. The variability of water vapor shows a maximum in the subtropics of both hemispheres, Figure 2.3.2 (right). In the equatorial region and poleward of 60° the variability of water vapor is very small.

The water vapor concentration in the stratosphere is with 3-4 ppmv[1] very small. Most of the stratospheric water vapor is located in the lower stratosphere. It has been suggested that this water vapor is controlled by the temperature of the tropopause, and by the formation and dissipation of cirrus anvils due to outflow from cumulonimbus.

[1] parts per million by volume

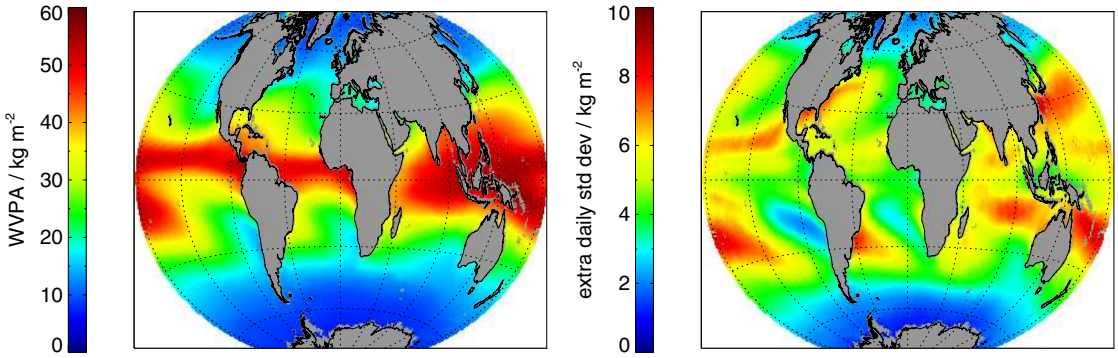

Figure 2.3.2: EUMETSAT CM-SAF SSM/I derived integrated water vapor (left) and associated variability (right), averaged over the time series from 1987 until 2006 [provided by Dr. Marc Schröder, DWD]

2.3.1 Definitions of humidity

Since water vapor is a gas, its partial pressure defines its concentration in the air. The letter "e" describes the partial pressure of water vapor (p_{wv}) in pascal, Pa. A lower case describes a partial pressure (ex:p_{wv}) and an upper case describes the pressure of the air (ex:P_{air}). The sum of the partial pressures of all atmospheric gases yields to the air pressure of the atmosphere :

$$P_{air} = e + p_d \tag{2.3.1}$$

with p_d: the partial pressure of dry air.

The equilibrium vapor pressure is defined as e for which the water vapor is in thermodynamic equilibrium state with its condensed phase. This value depends only on the temperature (T in Kelvin: K). The partial pressure of water vapor in an air parcel at a temperature T can not be higher than $e_s(T)$. More water vapor in this air parcel, will instantaneously condense and form liquid water. The empirically accurate relationship of Bolton (1980) describes the equilibrium vapor pressure as a function of T:

$$e_s(T) = 0.6112 \times \exp\left(\frac{17.67 \times T}{T + 243.5}\right) \quad in\ hpa \tag{2.3.2}$$

The relative humidity (RH) is defined as a ratio [%] between the water vapor's partial pressure and the equilibrium vapor pressure:

$$RH = \frac{e}{e_s} \times 100\% \tag{2.3.3}$$

The relative humidity describes how far from the saturation (i.e. condensation) the water vapor is in the air, that in terms of partial pressure.

Another way to characterize the humidity of the air is to define the mixing ratio, r in g/kg of an air parcel:

$$r = 1000 \times \frac{m_w}{m_d} \quad in \;\; g/kg \tag{2.3.4}$$

where m_w denotes the mass of water vapor and m_d the mass of dry air in the air parcel. In terms of partial pressure it is defined as:

$$r = 1000 \times \frac{M_{\text{vap}}}{M_{\text{air}}} \frac{e}{P_{air} - e} \tag{2.3.5}$$

with the molar weight of water vapor: M_{vap} (about 18g/mol) and of dry air: M_{air} (about 29g/mol), the pressure of air P_{air} and the partial pressure of water vapor: e. The ratio $\frac{M_{\text{vap}}}{M_{\text{air}}}$ is usually noted as δ:

$$\delta = \frac{M_{\text{vap}}}{M_{\text{air}}} = 0.62197 \tag{2.3.6}$$

The specific humidity describes the part (in mass) of water vapor in an air particle:

$$SH = 1000 \times \frac{m_w}{m_a} \quad in \;\; g/kg \tag{2.3.7}$$

with m_w, the mass of water vapor and m_a, the mass of the whole humid air, in the air parcel. The specific humidity can be linked to the mixing ratio r:

$$SH = \frac{1000 \times r}{r + 1000} \tag{2.3.8}$$

The mass of water vapor in a given volume of air is named the absolute humidity, and is expressed in kg/m^3:

$$AH = \frac{m_w}{V_a} = e \times \frac{M_w}{RT} \quad in \;\; kg/m^3 \tag{2.3.9}$$

2.3.2 Definition of integrated water vapor

Integrated water vapor defines how many water vapor is in a column between two levels of height. This quantity is written as IWV and expressed in kg/m^2. The integrated water vapor content between the altitudes z_1 and z_2 is defined as:

$$IWV(z_1, z_2) = \int_{z_1}^{z_2} AH(z)\,\mathrm{d}z \quad in \;\; kg/m^2 \tag{2.3.10}$$

The integrated water vapor content between the pressure levels P_1 and P_2 is:

$$IWV(P_1, P_2) = \int_{P_1}^{P_2} \frac{AH(P)}{\rho_{air}(P)g}\,\mathrm{d}P = \frac{1}{1000g}\int_{P_1}^{P_2} SH(P)\,\mathrm{d}P = \frac{1}{g}\int_{P_1}^{P_2} \frac{r(P)}{1000 + r(P)}\,\mathrm{d}P \tag{2.3.11}$$

where, g is the Earth's gravity and ρ_{air} is the density of air. SH and r are expressed in g/kg. It can also expressed in terms of water vapor's partial pressure and temperature:

$$\Delta IWV(z_1, z_2) = \int_{z_1}^{z_2} \frac{e(z)M_w}{RT(z)}\,\mathrm{d}z \tag{2.3.12}$$

where $R = 8.314472\ JK^{-1}mol^{-1}$ is the ideal gas constant and T is the air temperature in K.

It can be comfortable to convert the integrated water vapor content in cm of column because most of the absorption quantities are given in $[cm^{-1}]$. The quantity u describes the water vapor column in cm:

$$u = 100 \times \frac{IWV}{\rho_{lw}} \quad in\ \ cm \tag{2.3.13}$$

Because the volume mass of liquid water is $\rho_{lw} = 1000\ kg/m^3$, it can be written:

$$u = 0.1 \times IWV \tag{2.3.14}$$

So the water vapor column in cm above an altitude z_1 or a pressure level $P_1 = P(z_1)$ is:

$$u(z_1) = 0.1 \times \int_{z_1}^{\infty} \frac{e(z)M_w}{RT(z)}\,\mathrm{d}z = \frac{1}{10^4 g}\int_0^{P_1} SH(P)\,\mathrm{d}P = \frac{0.1}{g}\int_0^{P_1} \frac{r(P)}{1000 + r(P)}\,\mathrm{d}P \quad in\ \ cm \tag{2.3.15}$$

and, the water vapor column in cm in a thin layer at the pressure level is:

$$\Delta u(P) = 0.1 \times \Delta IWV(P) = \frac{SH(P)\Delta P}{10^4 \times g} = \frac{0.1}{g} \times \frac{r(P)\Delta P}{1000 + r(P)} \quad in\ \ cm \tag{2.3.16}$$

The different units of integrated water vapor can be converted as described in Table 2.1:

	mm	cm	$\frac{g}{cm^2}$	$\frac{kg}{m^2}$
mm	1	10	10	1
cm	0.1	1	1	0.1
$\frac{g}{cm^2}$	0.1	1	1	0.1
$\frac{kg}{m^2}$	1	10	10	1

Table 2.1: Units for integrated water vapor

2.3.3 Water vapor absorption

As indicated in section 2.2 the atmosphere is composed of different gases. The molecules of all these gases can be in several quantum states. The change from one quantum state *(a)* to another *(b)* corresponds to an exchange of energy between radiation and matter (absorbing or emitting photons). The wavelength λ of the absorbed or emitted radiation is linked to the energy gap between the quantum states *(*a*)* and *(b)* by the Einstein law:

$$\Delta E = E_b - E_a = \frac{hc}{\lambda} \tag{2.3.17}$$

with h denoting the Planck´s constant, c is speed of light.

Except for the ultraviolet (UV) and visible (VIS) wavelength, where scattering by air molecules occurs, the overall transmittance of cloud free atmosphere is mainly controlled by absorption and emission due to the constituent gases. Where absorption is strong the transmittance is small; where absorption is weak or absent the transmittance is close to 1.

Figure 2.3.3 shows that throughout the most of the visible (VIS), atmospheric water vapor is quite transparent. In the near infrared (NIR) the transmittance is varying a lot due to the absorption of water vapor. In the thermal infrared (TIR) there is another broad band of near-total absorption due to water vapor and increasing absorption by it beyond 12μm. In the far TIR water vapor absorption is dominant.

As water vapor is highly variable in the atmosphere the transmittance of it is strongly linked to the concentration of water vapor. Figure 2.3.4 shows the transmittance between 895nm and 905nm for a mid latitude summer and an arctic winter atmosphere. Both were calculated from HITRAN-2000 data (Rothman et al., 2003). One can see that the transmittance is high for the arctic winter atmosphere that has very low atmospheric water vapor, and the transmittance is low for the mid latitude summer atmosphere.

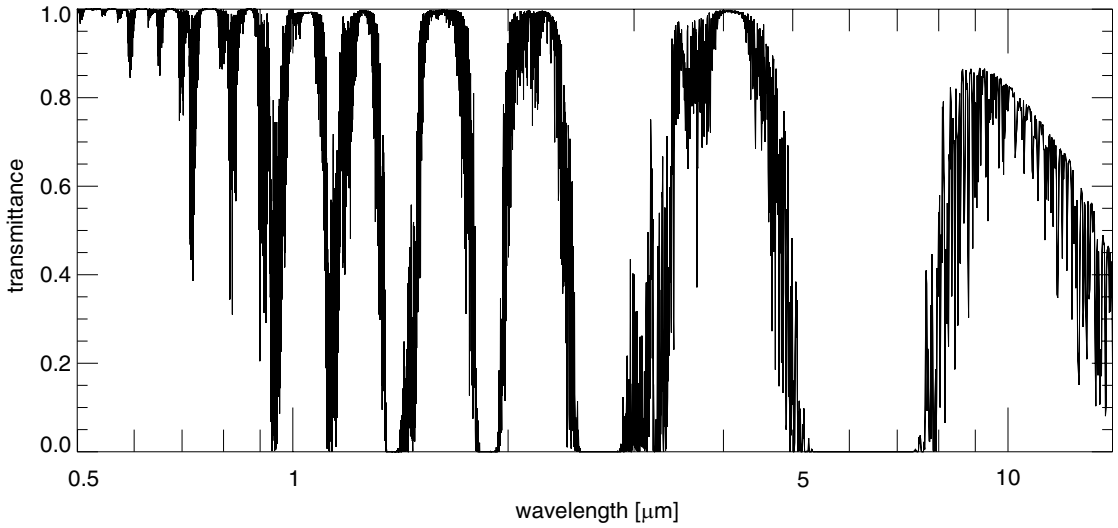

Figure 2.3.3: Transmittance of water vapor of an US-standard atmospheric profile (air mass 1). The x-axes denotes the wavelength for the UV - VIS - NIR and the TIR spectral region in [μm] while the y-axes show the transmittance.

2.4 Aerosols in the atmosphere

In addition to gaseous constituents, the atmosphere contains countless small particles of dust, salt, water, and other materials. A gaseous or airborne cloud of these particulate matter, either as a solid, liquid, or gas are named aerosols. Aerosols can be of natural origin like volcanic, salt and dust or produced by human activities. The classification of the aerosols can be done in terms of their origin (maritime, continental, urban, desert, ...) or of their composition (soot, sulfate, dust ...).

We can also classify the aerosols by their particle size. For large aerosol types the mean radius is in the order of 10μm, while other aerosol types typically are smaller than 1μm. Depending on size and composition, these particles scatter or scatter and absorb radiation. Radiative properties of aerosols strongly depend on the refractive index of the components as well as on the effective size or size parameter of the mixture.

2.4.1 Particle scattering and absorption

Absorption and scattering properties of particulate matter can be estimated by the size parameter x and complex refractive index $m = m_r - im_i$. The real part m_r of the refractive index is a measure of the scattering behavior while the imaginary part m_i

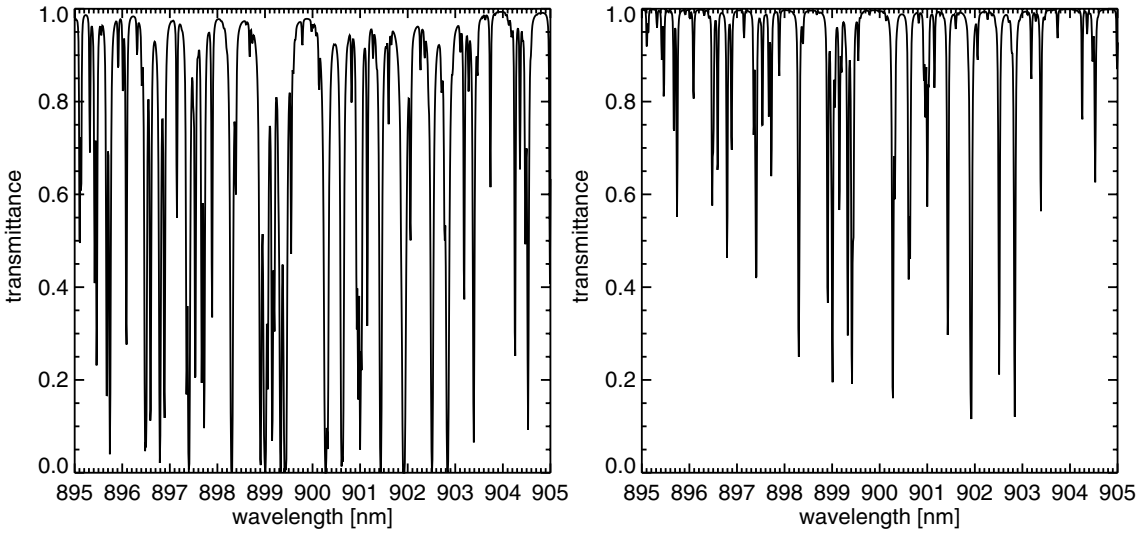

Figure 2.3.4: Atmospheric transmittance between 895nm and 905nm for two standard atmospheres (left: mid latitude summer, right: arctic winter) calculated from the HITRAN-2000 database.

represents the importance of absorption. The size parameter is defined as:

$$x = \frac{2\pi a}{\lambda} \tag{2.4.1}$$

It relates the particle size to the wavelength λ of the incident radiation where a denotes the geometrical size of the particle, e.g. the radius r of a sphere. For particles with $x \ll 1$ Rayleigh scattering is applicable. For spherical particles with $x \gtrsim 1$, Mie theory is characterizing the scattering, while optical properties of particles with $x \gg 1$ can be calculated with geometric optics.

The Mie theory is valid for homogeneous spherical particles and describes its optical properties. The directional dependency of scattering is given by the phase function $P(\Theta)$,where Θ denotes the scattering angle. The phase function basically depends on incident and scattering direction explicitly, for spherical particles the angular dependency is reduced to the scattering angle because of the spherical symmetry of the particles. For these particles the typical phase function show a strong forward peak and a slighter peak in backward direction.

In contrast to Rayleigh scattering, where extinction efficiency is proportional to λ^4, Mie scattering is linearly varying with wavelength. For large particles, compared to the wavelength of radiation, rapid fluctuations of the phase function occur due to interference

effects. For non spherical particles with an arbitrary size and shape no practical solution for scattering of light exists.

2.4.2 Radiative properties of aerosols

The previously described optical properties have been derived for single particles. Realistic atmospheres contain a mixture of particles with different sizes, shapes and chemical compositions (aerosols). Commonly, the size of particles in a poly-dispersion is described by the particle size distribution $n(a)$. It describes the number of particles per unit volume, with respect to their size a. There are different size distributions for different particle regimes. The most widely used size distributions are log-normal distributions. The basic form of these distributions is:

$$n(a) = \frac{C}{a\sigma_0} \exp[\frac{-(\log a - \log a_m)^2}{2\sigma_0^2}], \tag{2.4.2}$$

where C is a constant, $\sigma_0$the width of the distribution, and a_m denotes the modal diameter. The total number of particles is defined by:

$$N = \int_{a_{min}}^{a_{max}} n(a)da, \tag{2.4.3}$$

where a_{min} and a_{max} are the minimum and maximum particle size considering by the distribution, respectively.

Scattering by aerosols is assumed to be incoherent, that mean a scattering event at one particle does not interfere with those other particles. Therefore, scattered intensities may be added without regard to the phases of the individual scattered waves. In consequence, bulk optical properties can be obtained by a weighted mean of single particle properties. The extinction coefficient of a bulk of particles is given by

$$\beta_e = \int_{a_{min}}^{a_{max}} n(a)\sigma_e(a)da \tag{2.4.4}$$

,where σ_e is the extinction cross section of a single particle. Scattering as well as absorption can be calculated analogously. The phase function of a poly-dispersion is derived from

$$\beta_s P(\theta) = \int_{a_{min}}^{a_{max}} n(a)\sigma_e(a)P(\theta, a)da \tag{2.4.5}$$

The relation of scattering to extinction by a sample of particles is defined as the single

scattering albedo

$$\varpi_0 = \beta_s/\beta_e. \tag{2.4.6}$$

Conservative scattering is characterized by negligible absorption, i.e., $\beta_e \approx \beta_s$ and $\omega_0 \approx 1$.

In the visible spectral region, aerosol scattering is dominating. For oceanic and sulfate particles absorption is small but stronger for mineral, dust like and water soluble components. In the infrared region, size parameter for most of the aerosols become very small.

2.5 Surface albedo

Beside being dependent on atmospheric conditions, the radiative field in the atmosphere is affected by the presence of a lower boundary, which absorbs and reflects incident radiation and thermally emits radiation. The lower boundary surface can be land or water surfaces, or some atmospheric layer like a dense cloud layer. Radiative properties of the surface primarily depend on the soil material, its chemical composition, surface roughness, moisture, surface cover (vegetation) etc. The surface properties are defined as dimensionless ratio of absorbed or scattered intensity to incident energy. Absorption and emission of the surface are usually considered as isotropic, i.e. independent of direction. They are described by the parameters absorptivity A_{surf} and emissivity E_{surf}. When considering no transmission through the surface, from the principle of energy conservation follows

$$A_{surf} + \alpha_{surf} = E_{surf} + \alpha_{surf} = 1 \tag{2.5.1}$$

, where α_{surf} denotes the surface albedo of the surface. It is not possible to measure directly the surface albedo α_{surf} but it can be calculated by integrating the spectral albedo α_λ over the solar spectrum.

The Earth's spectral surface albedo is regularly estimated via Earth observation satellite sensors such as NASA's MODIS instruments onboard the Terra and Aqua satellites. Satellite instruments measure the reflective spectral radiance $L_\lambda(\mathbf{\Omega})$ coming from the surface to the sensor at specific direction ($\mathbf{\Omega}$). Where $\mathbf{\Omega}$ is direction defined by the polar angle ϕ and the zenith angle θ. The ratio ρ is defined by the measured reflected radiance over the known spectral incoming solar radiance $L_\lambda(\mathbf{\Omega'})$. The ratio $\rho_\lambda(\mathbf{\Omega}, \mathbf{\Omega'})$ is the spectral bi-directional reflectivity (BRDF):

$$\rho_\lambda(\mathbf{\Omega}, \mathbf{\Omega'}) = \frac{L_\lambda(\mathbf{\Omega})}{L_\lambda(-\mathbf{\Omega'})\cos\theta' d\Omega'}, \tag{2.5.2}$$

where $d\Omega'$ is the elementary solid angle at the direction $\mathbf{\Omega'}$. Generally, reflection varies with both, direction of incidence ($\mathbf{\Omega'}$) and direction of reflected radiation ($\mathbf{\Omega}$). The spectral albedo is defined as the total reflected upwelling flux over total incoming flux:

$$\alpha_\lambda = \frac{F_{ref}^{up}(\lambda)}{F_{inc}^{down}(\lambda)} = \frac{\int_0^{2\pi} L_\lambda(\mathbf{\Omega}) cos\theta d\Omega}{\int_0^{2\pi} L_\lambda(\mathbf{\Omega'}) cos\theta' d\Omega'}. \tag{2.5.3}$$

It is possible to invert α_λ from ρ_λ by using several techniques depending on the sensor that is used. The spectral albedo α_λ is an essential parameter for the inversion of satellite retrievals, for example the MERIS water vapor retrieval shown in section 4. The spectral albedo is also known as spectral reflectance and varies greatly from surface type to surface type in the VIS and NIR spectral region. An illustration can be found in Figure 4.3.1.

3 The MERIS instrument and the numerical weather prediction models COSMO-DE and COSMO-EU

3.1 The MERIS instrument

The Medium Resolution Imaging Spectrometer MERIS is a programmable, medium-spectral resolution, imaging spectrometer. Is one of ten instruments on board the environmental research satellite ENVISAT that is operated by the European Space Agency (ESA). An illustration of ENVISAT is shown in Figure 3.1.1. ENVISAT was launched in March 2002 flying at 800km in a sun-synchronous orbit with an equator crossing time of 10:00 UTC, descending node, and 98.5° inclination. MERIS has a global coverage every 2-3 days with 14.3 orbits per day.

MERIS was mainly developed for the remote sensing of the ocean color but it has also spectral bands for the remote sensing of atmospheric properties. The instrument consists of five identical pushbroom imaging spectrometers operating in the solar spectral range (390nm to 1040nm), arranged in a fan shape configuration which covers a total field of view of 68.5° and spans a swath width of around 1150km. MERIS has 15 channels which are programmable by ground command in width and in position covering the VIS and NIR spectral region between 400 and 900nm. In operation mode the spatial resolution of MERIS is reduced by a factor of 4 along and across track leading to reduced resolution (RR) of 1km x1km for a nadir pixel. In the full resolution mode, the full spatial resolution (FR) with 300m x 300m is transmitted. The positions and width of these channels given in table 3.1, vary slightly across the field of view of MERIS. This "spectral smile" is caused by curvature of the image of the slit formed in the focal plane array, resulting in viewing angle-dependent central wavelengths of the spectral MERIS channels. In order to accurately determine the spectral smile of MERIS, spectral calibration campaigns are conducted repeatedly, using the full possible spectral resolution in the oxygen A band and solar Fraunhofer lines, Delwart et al. (2007); Lindstrot et al. (in press).

Band #	Band center [nm]	Bandwidth [nm]	Application
1	412.5	10	Yellow substance, turbidity
2	442.5	10	Chlorophyll absorption maximum
3	490	10	Chlorophyll, other pigments
4	510	10	Turbidity, suspended sediment, red tides
5	560	10	Chlorophyll reference, suspended sediment
6	620	10	Suspended sediment
7	665	10	Chlorophyll absorption
8	681.25	7.5	Chlorophyll fluorescence
9	705	10	Atmospheric correction, red edge
10	753.75	7.5	Oxygen absorption reference
11	760	3.75	Oxygen absorption R-branch
12	775	15	Aerosols, vegetation
13	865	20	Aerosols corrections over ocean
14	885	10	Water vapor absorption reference
15	900	10	Water vapor absorption, vegetation

Table 3.1: The MERIS Spectral bands and its main application

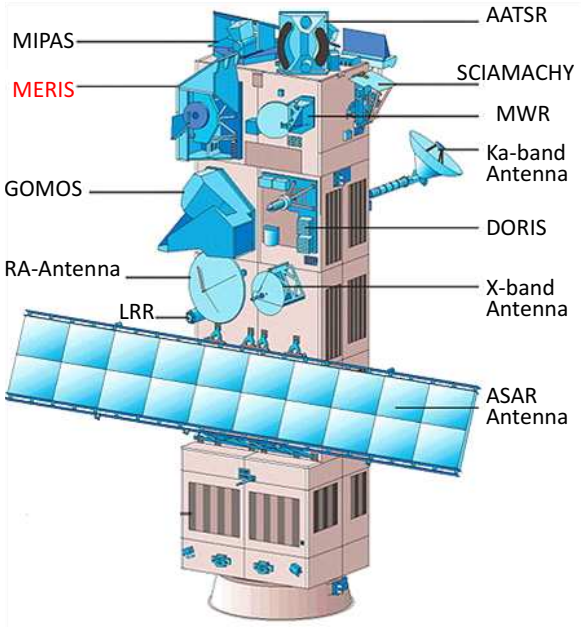

Figure 3.1.1: The ENVISAT satellite and its instruments. Image courtesy of ESA.

3.2 The COSMO numerical weather prediction model system

The Lokal-model (LM) has been developed at the Deutscher Wetterdienst (DWD). It is a non-hydrostatic, fully compressible, limited area atmospheric prediction model and has been designed for operational weather prediction as well as for various scientific applications. Most numerical weather prediction (NWP) models operate on grid spacings down to 10km and therefore lack the spatial resolution required to resolve small-scale weather events. The LM, with its grid resolution of 7km, has been designed for resolving meso-β[1] and meso-γ[2] scale where non-hydrostatic effects begin to play an important role in the evolution of atmospheric flows. The developments of the LM have been organized within COSMO, the COnsortium for small Scale Modeling. At present, the following meteorological services are participating:

- DWD Deutscher Wetterdienst, Offenbach, Germany
- MeteoSwiss Meteo-Schweiz, Zurich, Switzerland
- UGM Ucio Generale per la Meteorologia, Roma, Italy
- HNMS Hellenic National Meteorological Service, Athens, Greece
- IMGW Institute of Meteorology and Water Management, Warsaw, Poland
- ARPA-SIM Il Servizio IdroMeteorologico di ARPA, Bologna, Italy
- ARPA-Piemonte Agenzia Regionale per la Protezione Ambientale, Piemonte, Italy
- AWGeoPhys Amt für Geoinformationswesen der Bundeswehr, Euskirchen, Germany
- NMA National Meteorological Administration, Bukarest, Romania

The further development of the LM model system is organized in working groups that cover: data assimilation, numerical aspects, physical aspects, interpretation and application, verification, and case studies. COSMO-DE and COSMO-EU are two applications of the LM model that have been developed at Deutscher Wetterdienst. Both were used within that work and are described in the following subsections. A full description of the COSMO LM model system can be found in Doms et al. (2002); Doms and Schättler (2002); Schraff and Hess (2003).

[1] meso-β scale: phenomena (δs: 5 km to 50 km)
[2] meso-γ scale: phenomena (δs: 500 m to 5 km)

3.2.1 The COSMO-EU model

In September 2005 the LME[3] model was introduced by the Deutsche Wetterdienst as a new application of the COSMO model system. In 2007, the COSMO consortium conclude a consistent model naming for all operational COSMO model systems leading to a renaming of LME to COSMO-EU. It is a mid range numerical weather prediction model with a forecast range of 78 hours. The current spatial resolution of the COSMO-EU models is covering the meso-β scale using a 7km grid spacing. The key issue is an accurate numerical prediction of near surface weather, focusing on clouds, fog, frontal precipitation, and orographic and thermal forced wind systems. The major changes in comparison to the COSMO model (LM) are:

- the enlarged integration domain covering Europe with 665x657 grid points with a resolution of 0.0625°≈7km,
- the extension from 35 of vertical levels up to 40, with the lowest level 10 meter above ground,
- the north pole has been shifted to 40°N and 170°W (was 32.5°N and 170°W before), which has the advantage that the equator of the rotated longitude-latitude system is in the middle of the model domain,
- the extension of the forecasts up to 78 hours,
- the introduction of prognostic precipitation: With an update in the dynamical scheme it is now possible to take into account the advection of the new prognostic variables rain and snow. In the leapfrog-scheme a semi-Lagrange advection of these hydro-meteors has been implemented. This results in a reduction of precipitation peaks over mountains and shifts precipitation from the windward side of mountains to the lee side.
- Micro-physics: A new version of the micro-physics with major changes in the parametrization of snow has been introduced: It comprises a variable intercept parameter based on Field et al. (2005), temperature-dependent sticking efficiency, and changes in geometry and fall speed of snow.
- Radiation: New external parameter fields have been introduced to specify the fraction of evergreen or deciduous forest in a grid box. These are used to modify the solar albedo for snow covered grid boxes.

[3]LME: Lokal Model Europa

- Turbulence: The ratio of laminar scaling factor for heat over sea has been increased to reduce the sensible and latent heat flux over water. This results in a better simulation of low pressure systems, which have been overestimated before.

- Soil model: The new multi-layer soil model is now used, which takes into account the thermal effects of freezing and thawing of soil water. Also the treatment of snow has been improved, e.g. by computing a prognostic snow density and allowing for an aging of the snow pack. Currently, 7 soil layers are used.

- Diagnostics: With the introduction of an interface to the RTTOV-library (Fast Radiative Transfer Model for TIROS Operational Sounder), it is now possible to calculate synthetic satellite images. Based on model data, the radiances and brightness temperatures measured by satellites can be simulated.

The model is defined on rotated longitude-latitude coordinates with longitude = - 18.0°, latitude = -20.0° of the lower left and longitude = 23.5°, latitude = 21.0° of the upper right corner. Figure 3.2.1 shows the new integration domain, illustrating the topographic height.

Since the COSMO-EU model is a local model, it has to be driven at the boundary. This is done by the global model (GME). The three hour GME forecasts produce the first guess that is used to generate boundary data at one hour intervals for the COSMO-EU assimilation cycle. The data assimilation is based on observation nudging, Schraff and Hess (2003). Assimilated observations are radio soundings (wind, temperature, humidity), aircraft (wind, temperature), and surface level data (SYNOP, SHIP, BUOY: pressure, wind, humidity). The nudging assimilating system produces a continuous analysis stream, where data are assimilated at the time they are observed but using a time-weighting function to spread the information in time. Three hour COSMO-EU assimilation runs are done. Analysis files are written every hour. Besides the analysis by observational nudging, three external analyses are run:

- a sea surface temperature (SST) analysis (00 UTC),

- a snow depth analysis (00, 06, 12 and 18 UTC),

- a variational soil moisture analysis (00 UTC).

A full description of the COSMO-EU model system is given by Schulz and Schättler (2009).

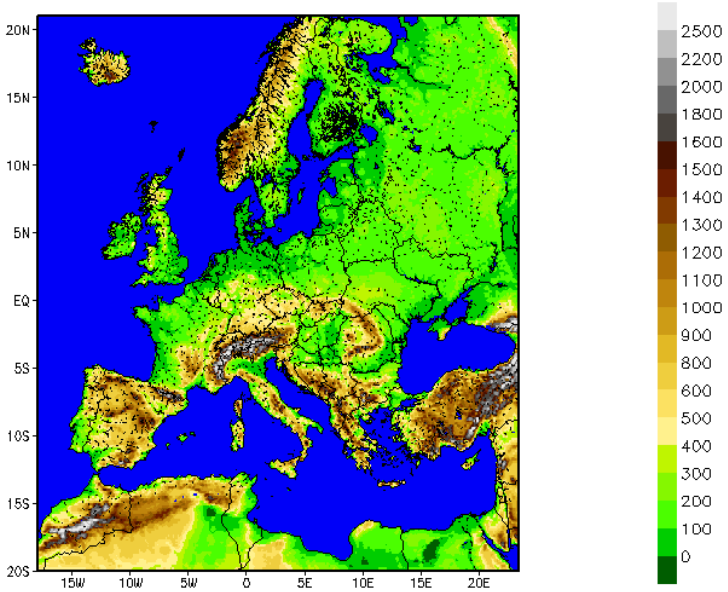

Figure 3.2.1: Topographic height in meter [m] for the COSMO-EU domain.

3.2.2 The COSMO-DE model

Since August 2006 the LMK[4] model completes the GME and COSMO-EU (LME) model system of the Deutsche Wetterdienst. It is the very short-range numerical weather prediction application of the COSMO model system with a forecast range of up to 21h. The LMK was renamed to COSMO-DE in 2007. The most important changes to the COSMO-EU system is the very high spatial resolution of the grid with 2.8km covering the meso-γ scale. That high grid spacing, allows a direct simulation of different weather events that are triggered by deep moist convection because it can be explicitly resolved and the impact of topography on the organization of penetrative convection is represented much more realistic. Further changes to the LM model are:

- the model domain covers whole Germany, most part of the Alps and some smaller parts of the neighboring states (Figure 3.2.2),
- the forecast period is up to 21hours,
- it has 421x461 grid points and with a resolution of 0.025°≈2.8km,
- the extension from 40 vertical levels up to 50, with the lowest level 10 meter above ground,

[4]LMK: Lokal Model Kürzestfrist

- implementation of a two time level dynamical core based on Runge-Kutta methods. This allows the use of more accurate advection algorithms (5th order for horizontal advection), which is desirable for very high resolutions,
- deactivation of parametrization of high convection. The model will resolve this in the dynamics. A modified version of the parametrization for shallow convection is still kept in the model.
- The parametrization of cloud micro-physics includes graupel.
- In the assimilation part, an algorithm for Latent Heat Nudging has been implemented to assimilate very high resolved radar data.

COSMO-DE is defined at the same rotated grid as COSMO-EU, with coordinates of the lower left and the upper right corner of lon = -5.0°, lat = -5.0° and lon = 5.5°, lat = 6.0°, respectively. As a meso-γ model the COSMO-DE model has special requirements concerning data assimilation, and highly resolved, rapidly updated data fields are needed. COSMO-DE runs are initialized from a continuous data assimilation cycle in which the nudging method (described in Schraff and Hess (2003)) is applied. Additionally, the following external analysis are performed for data assimilation:

- a sea surface temperature (SST) analysis (00 UTC),
- a snow depth analysis (00, 06, 12 and 18 UTC),
- assimilating radar data within the nudging at 00, 03, 06, 09, 12, 15, 18, 21 UTC.

A full description of the COSMO-DE model is given by Baldauf et al. (2009).

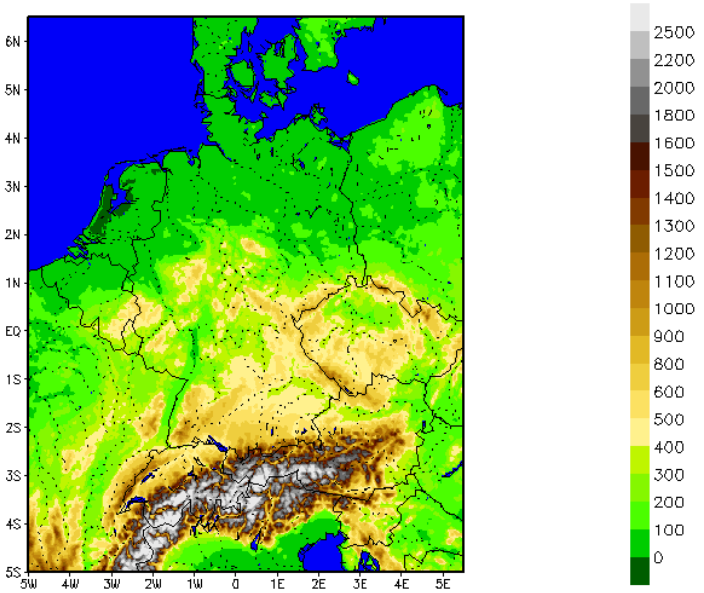

Figure 3.2.2: Topographic height in meter [m] for the COSMO-DE domain.

4 The MERIS water vapor algorithm

This chapter describes the retrieval algorithm for integrated atmospheric water vapor (IWV) from measurements of the satellite based MERIS instrument. The definition of integrated water vapor can be found in 2.3.2. In this work a number of expressions are used synonymously for the denotation of the atmospheric water vapor, e.g. integrated water vapor, columnar water vapor.

4.1 Algorithm overview

The proposed water vapor retrieval is based on the principle of differential absorption (Fischer, 1988). Solar radiation is transmitted through the atmosphere to the surface, reflected at the surface, and transmitted back to space. This signal at sensor height is measured at a specific wavelength λ and is related to the total mass m of the transmitting constituents and their mass extinction coefficient k_λ, briefly the transmittance T (2.1.5). The transmittance for two model atmospheres within the spectral range relevant for MERIS channel 15 is shown in Figure 2.3.4. This spectral region exhibits strong absorption by water vapor. The strength and broadness of individual lines is controlled by total water vapor amount.

For monochromatic radiation and ignoring every diffusion effect (no cloud, no aerosol), the measured spectral radiance L can be written as a function of incoming solar irradiance S^0, atmospheric transmittance T_{atm} and the surface albedo α:

$$L = S^0 T_{atm} \alpha \tag{4.1.1}$$

The atmospheric transmittance is defined as: $T_{atm} = e^{-\tau_{atmo}}$. For wavelengths where water vapor is the only absorber the atmospheric optical depth τ_{atm} can be written as:

$$\tau_{atm} = \int_0^{z_{TOA}} k_{e,wv}(z)\rho_{wv}(z)dz \tag{4.1.2}$$

where z_{TOA} is the altitude of TOA in [m], ρ_{wv} is the density of water vapor in [kg/m^3] and

k_e is the mass extinction coefficient of water vapor at the given wavelength in [m^2/kg]. The mass extinction coefficient is highly dependent on wavelength and the vertical profile of pressure and temperature. Nevertheless, introducing an "average" parameter, named $\bar{k_\lambda}$ corresponding to the presumed (T, P, water vapor) vertical profile, the atmospheric optical depth can be written as:

$$\tau_{atm} = \bar{k_\lambda} \int_0^{z_{TOA}} \rho_{wv}(z) = \bar{k_\lambda}\, IWV \tag{4.1.3}$$

$\bar{k_\lambda}$ only depends on the presumed profile and on the wavelength. The atmospheric transmittance can be linked to the integrated water vapor (IWV) by:

$$T_{atm} = e^{-\bar{k_\lambda}\, IWV} \tag{4.1.4}$$

Since the transmittance can not be measured directly it was derived by the logarithm of the radiance ratio of two spectral channels, one within the water vapor absorption band and one in the window channel with transmittance equal to 1.

$$IWV = \frac{-1}{k_{abs} - k_{win}} \ln\left[\frac{L_{abs}}{L_{win}}\right] \tag{4.1.5}$$

MERIS provides measurements in the water vapor absorption band (MERIS band 15) as well in a non absorbing window channel (MERIS band 14), shown in Figure 4.1.1. Both channels are optimized with respect to the observations of atmospheric water vapor (Fischer, 1988; Fischer and Bennartz, 1997). With $L_{abs} = L_{15}$, $L_{win} = L_{14}$, $k_{abs} = k_{15}$ and $k_{win} = k_{14} = 0$ (no water vapor absorption in this channel) the integrated water vapor is can be written as:

$$IWV = \frac{-1}{k_{15}} \ln\left[\frac{L_{15}}{L_{14}}\right] \tag{4.1.6}$$

The relation between the measured radiance ratio and the integrated water vapor was calculated using a radiative transfer model with a large variety of different atmospheric profiles (subsection 4.3). The algorithm development is based on sensitivity studies, which has been used to define the variable parameters accounted for the retrieval. The inversion of the measured radiances was performed by an artificial neuronal network (ANN) described in subsection 4.4.

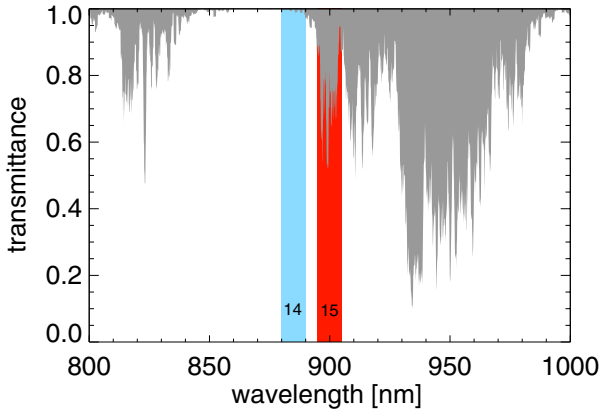

Figure 4.1.1: Transmittance T of a mid latitude summer atmosphere. The red and blue boxes indicate the positions and width of MERIS channel 15 at 900nm within the water vapor absorption and channel 14 at 885nm, which is the window channel.

4.2 Sensitivity studies

To determine the sensitivity of MERIS measurements to the individual influencing parameter, radiative transfer calculations were performed. The sensitivity studies were performed by using the radiative transfer model MOMO (Fell and Fischer, 2001; Fischer and Grassl, 1991; Plass et al., 1973). The MOMO Model is described in subsection 4.3. The simulations were analyzed with respect to the influence of the following parameters:

1. spectral albedo: the estimation of the transmittance T from the ratio of two close channels (one within and one outside the absorbing bands of water vapor) can be distorted if the corresponding surface reflectances differ.

2. aerosol optical thickness as well as the aerosol type: the effective photon path length can be shortened or extended in a complex way, depending on the brightness of the surface and the optical thickness of the atmospheric aerosol.

3. pressure and temperature profile: the absorption coefficients depend on pressure and temperature of the atmosphere.

The sensitivity of a measurement is commonly described by the partial differential:

$$\xi_j^i = \frac{\delta \ln s_i}{\delta \ln P_j}. \tag{4.2.1}$$

that quantifies the relative change of a signal s_i due to the relative change of the parameter P_j. In this work the signal is the transmittance of the reflected solar radiation, quantified by the ratio r (Eq. 4.1.6). The sensitivity can be written as:

$$\xi_j = \frac{\delta \ln r}{\delta \ln P_j} \tag{4.2.2}$$

this description is dependent on the absolute scales of the parameter P_j. Since it makes it difficult to compare the different sensitivities, the relative change of the signal is related to a reasonable change of each physical parameter P_j. Thus ξ is calculated as:

$$\xi_j = \frac{\delta \ln r}{\delta \ln P_j} \Delta P_j \tag{4.2.3}$$

with ΔP_j as a relative change or

$$\xi_j = \frac{\delta \ln r}{\delta P_j} \Delta P_j \tag{4.2.4}$$

with ΔP_j as an absolute value. The sensitivities of integrated water vapor IWV was derived (Figure 4.2.1). Additionally the sensitivities of aerosol optical thickness τ, aerosol type, surface albedo α, spectral albedo slope $(\alpha_{15} - \alpha_{14})$, temperature profile T and pressure profile p were derived. For a better interpretation of the following sensitivity studies of each influencing parameter, the individual sensitivity ξ_j is expressed as the equivalent change of integrated water vapor ΔIWV, that is the particular change of IWV causing the same change of signal as the examined parameter ΔP:

$$\Delta IWV = \frac{\frac{\delta \ln r}{\delta \ln P_j} \Delta P_j}{\frac{\delta \ln r}{\delta \ln IWV}}. \tag{4.2.5}$$

The sensitivity to the viewing geometry, has not been considered in order to limit the complexity of the presented results. It is usually known with high precision. All calculations were made for nadir view (viewing zenith angle = 0°) and a sun zenith angle of 35.6°.

4.2.1 Sensitivity of integrated water vapor retrieval to spectral albedo

First the impact of the spectral albedo α was determined by modifying systematically the surface albedos for channel 14 and 15. All calculations were made for a US standard vertical profile; a constant observation geometry (sun zenith angle = 35.6°, viewing zenith

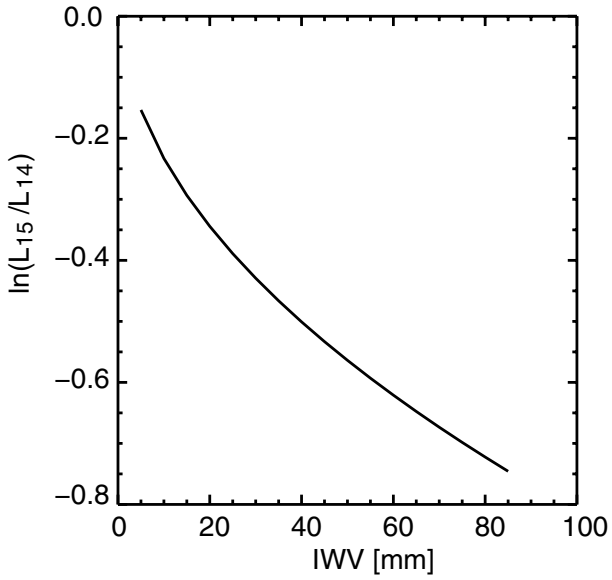

Figure 4.2.1: Integrated water vapor as a function of the natural logarithm of the radiance ratio of MERIS channel 15 and 14. Values are calculated for a sun zenith angle of 35.6° and a viewing zenith angle of 0°.

angle = 0°) and a medium water vapor amount of 30mm. The surface reflectance for band 14 range from 0.01 to 0.9 while for band 15, a spectral slope with a range of -5% to 5% was added. No aerosol properties were taken into account, i.e. the aerosol optical thickness was set to zero ($\tau_a = 0$) for all calculations. Figure 4.2.2 shows the results of the investigations. The x- and y-axes indicates the albedo at 885nm (band 14) and its deviation from the albedo at 900nm (band 15), respectively. The colors show the error in the retrieved water vapor where the albedo difference between band 15 and band 14 is not taken in consideration. The error in derived water vapor increases with increasing albedo. For dark surfaces ($\alpha_{14} = 0.15$) the equivalent change in IWV is small with ±5mm (16.6%), where the relative change is based on the 30mm water vapor set for the calculations. However, for bright surfaces ($\alpha_{14} = 0.9$) the difference of the spectral albedo leads to large differences in the IWV up to ±9mm (30%). This is twice as much as the mean annual changes in IWV for Europe.

4.2.2 Sensitivity of integrated water vapor retrieval to aerosol properties

An analogue study was performed to determine the effect of the aerosols on the IWV retrieval. The same configuration of the spectral albedo case was used, with the aerosol optical thickness (AOT) ranging from 0.0 to 0.3 at 550nm. The aerosol type changes

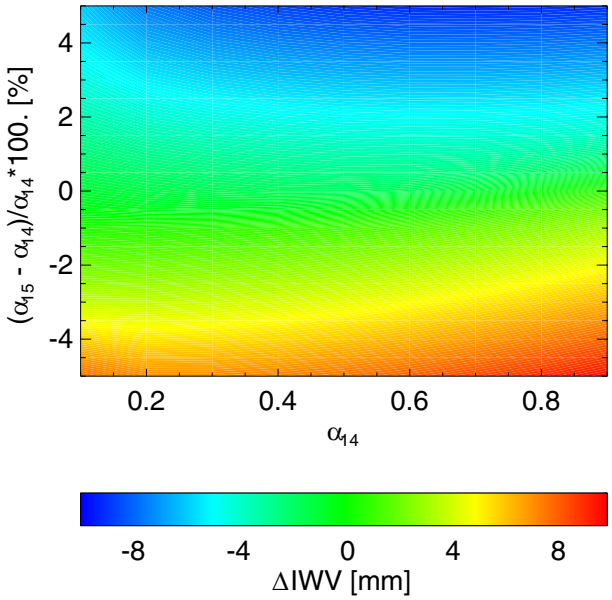

Figure 4.2.2: Equivalent change of IWV in the retrieved water vapor as a function of albedo in MERIS band 14 (α_{14}) and the difference between the spectral albedo for channel 15 and channel 14 in percentage ($(\alpha_{15}-\alpha_{14})/\alpha_{14}*100$). The considered IWV is 30mm.

between continental, maritime, desert and urban. Surface reflectances range from 0.01 to 0.8, but without a spectral slope between band 14 and 15. Figure 4.2.3 shows the sensitivity of the equivalent IWV for four different aerosol types. The x- and y-axes indicates the albedo and the differences in the equivalent change in IWV computed with an aerosol optical thickness of 0 and 0.3, respectively. The impact of aerosol properties on the IWV retrieval is with a maximum of ±1.5mm (5%) weak.

4.2.3 Sensitivity of integrated water vapor retrieval to temperature and pressure profiles

To determine the impact of pressure and temperature profiles the same configuration of the spectral albedo case was used while the vertical pressure and temperature profiles were changed. 1.) US standard pressure profile of ±10%; 2.) temperature desert profile and; 3.) subarctic winter temperature profile (SAW). The difference in the surface temperature is compared to the US-standard atmosphere +30K for the desert and -30K for the subarctic winter profiles. Figure 4.2.4 shows the equivalent change in the IWV as a function of albedo and the change in the temperature and pressure profiles. Variations in

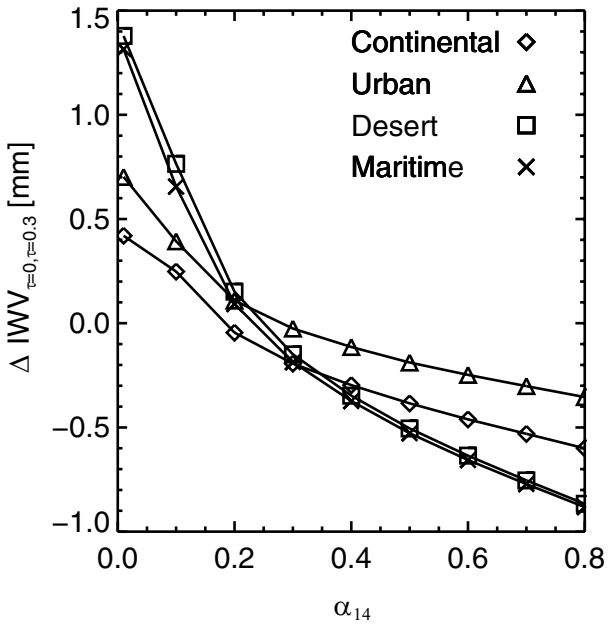

Figure 4.2.3: Equivalent change of IWV without including aerosol for four different aerosol types as a function of albedo in MERIS band 14 (α_{14}). The aerosol optical thickness for all aerosol types was assumed as $\tau = 0.3$. The the considered IWV is 30mm.

	Equivalent change in IWV [mm] to the reference IWV of 30mm
spectral albedo (±5%)	9 (30%)
aerosol optical thickness (0 - 0.3)	1.5 (5%)
Pressure profile (±10%)	1.0 (3.3%)
Temperature profile ($\pm 30K$)	0.8 (2.6%)

Table 4.1: Summary of the sensitivity studies tabulating the maximum difference in equivalent IWV for the varying environmental parameters.

the pressure profile has a similar effect on the observed signal as the effect of variations of the temperature profile with an equivalent change in IWV up to 1mm (3.3%).

The results of the sensitivity studies are summarized in Table 4.1. It is shown that the spectral albedo has the strongest influence on the water vapor retrieval. Therefore, the spectral variability of the surface albedo is taken into account in the improved water vapor algorithm.

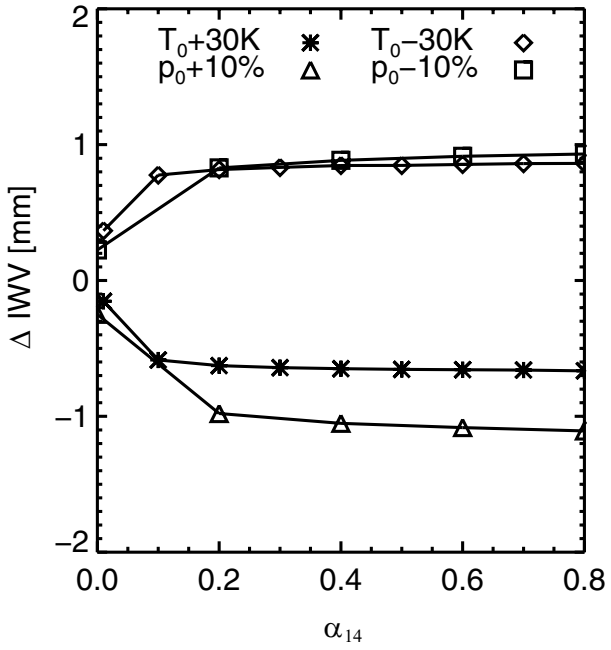

Figure 4.2.4: Equivalent change of IWV as a function of albedo MERIS band 14 (α_{14}), temperature and pressure compared to a US-standard atmosphere. The star line corresponds to a desert and the diamond line to a subarctic winter (SAW) temperature profile. The change in surface pressure of $\pm 10\%$ is illustrated by the triangle and square line, respectively. The the considered IWV is 30mm.

4.3 Forward model parametrization

The well established and validated radiative transfer code MOMO (Fischer and Grassl, 1991; Fell and Fischer, 2001) was used for radiative transfer simulations. MOMO is based on the Matrix Operator Method (Plass et al., 1973) that offers the possibility of a) combination of layers of any given optical properties b) very fast calculation even in the case of optically thick layers with highly anisotropic phase functions c) choice of any desired surface reflectivity, and d) the calculation of up and down welling radiances within the ocean and the atmosphere for all layer boundaries. Scattering and absorption processes due to aerosols and cloud particles are represented by appropriate scattering and extinction coefficients and the corresponding scattering phase function. These parameters are obtained by Mie theory. Air molecules are small compared to the wavelength of the incoming sunlight. Thus, the molecular scattering can be described with Rayleigh theory. The calculation of the gas absorption is based on the HITRAN-2000 dataset

(Rothman et al., 2003), which contains parameters of the single absorption lines of the main atmospheric gases. The absorption is of the atmospheric gases is calculated by using the k-binning Method (Bennartz and Fischer, 2000; Bennartz and Preusker, 2006). The model has been validated by comparisons with models and with spectral radiation measurements (Santer et al., 2005).

With MOMO the light propagation through the atmosphere and generated azimuthally resolved upward radiances in the MERIS bands at top of atmosphere (TOA) for different sun and observer geometries were simulated. A broad range of atmospheric temperature and pressure profiles, aerosol optical depths, surface reflectivities were taken into account to simulate the integrated water vapor. The results of the simulations have been inverted to infer integrated water vapor. Subsequently the input data and the method were described in detail.

4.3.1 Vertical temperature and pressure profiles

The vertical structure of the atmosphere was described by 22 homogeneous model layers. Vertical profiles of temperature, pressure and water vapor were taken from global radio soundings, covering a wide range of natural variations. These were taken from the Global Telecommunication System (GTS). This dataset consists of more than 500,000 global radiosonde profiles over land. Automatic tests for temperature, pressure and water vapor to identify erroneous measurements in the radiosonde data were applied. The radio soundings consisted of at least 15 levels and the cloud fraction, available from considering surface data, had to be less or equal 50%. A reduced dataset of 399 radio soundings was used to ensure maximum variations in surface pressure and water vapor. The total water vapor amount of the radiosondes, ranges from 1.3 to 76.3mm, the surface temperature ranges from -11.5 and 33.2 $°C$ and surface pressure ranges from 986.9 to 1024.3 hPa.

4.3.2 Aerosol optical parameters

Random variances were applied to aerosol types, vertical distribution, and aerosol optical depth. For each simulation, three different aerosol types were considered; stratospheric, tropospheric background, and continental aerosol. The stratospheric and tropospheric background aerosol were placed between 10km and 20km, and the continental aerosol in the lower atmosphere between 0km and 5km. All three atmospheric constituents were allowed to vary randomly within the natural range of variability, as shown in Table 4.2.

Type	Min. opt. depth τ	Max. opt. depth τ at 550nm
Stratospheric	0.005	0.01
Trop. Background	0.01	0.09
Continental (land)	0.01	0.15

Table 4.2: Setup of aerosol models. Minimum and maximum of aerosol optical depth τ taken into account in the radiative transfer simulations.

4.3.3 Spectral surface reflectance

The influence of the absolute value and the spectral behavior of the surface reflectance on the water vapor retrieval is shown in section 4.2. For the simulations, reflectance spectra from an enhanced ALBEDOMAP dataset (Muller et al., 2007) was used. This dataset includes a 16 day average of the spectral surface albedo for the MERIS channels 1 to 10 and 12 to 14. Since the ALBEDOMAP dataset does not include the needed surface albedo for MERIS channel 11 and 15 it was approximated as a linear combination of albedo values of nine standard spectra, with the weight assigned by a linear regression. To ensure a highly independent dataset as a bases for the regression procedure, nine highly independent and representative surface reflectance spectra were taken from the ASTER spectral library (Baldridge et al., 2009). Figure 4.3.1 illustrates the used surface reflectivity spectra.

The actual probability distribution of the reflectance spectra was determined over the land surface of Earth from this completed dataset (FUB-albedo dataset). For each simulation a random spectrum was selected from the dataset based on this probability distribution. The selection was constructed in a way that snow spectras were rejected if the surface temperature of the vertical profile exceeded 283K.

As an example the spatial distribution of the calculated differences of the spectral albedo for channel 15 and 14 is shown in Figure 4.3.2. The differences were calculated from the FUB-albedo dataset for Europe and North Africa for July and October 2003. High differences in Central Europe are observable for the July dataset whereas the differences decrease in October. Since, vegetation in desert is rare no seasonal change is observable for North Africa.

4.4 Inverse model parametrization - the water vapor ANN

The dataset of simulated relations between the integrated water vapor and MERIS spectral measurements acts as a database for the regression. For the inversion of the measured

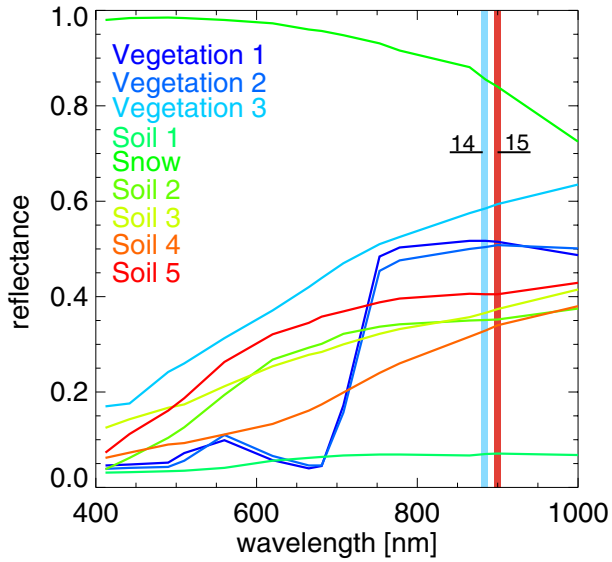

Figure 4.3.1: Nine standard albedo spectra used for the regression to estimate the surface albedo at 900nm. The vertical blue line illustrates the spectral position of MERIS channel 14 and the vertical red line channel 15. The spectra are provided by the ASTER spectral library (Baldridge et al., 2009).

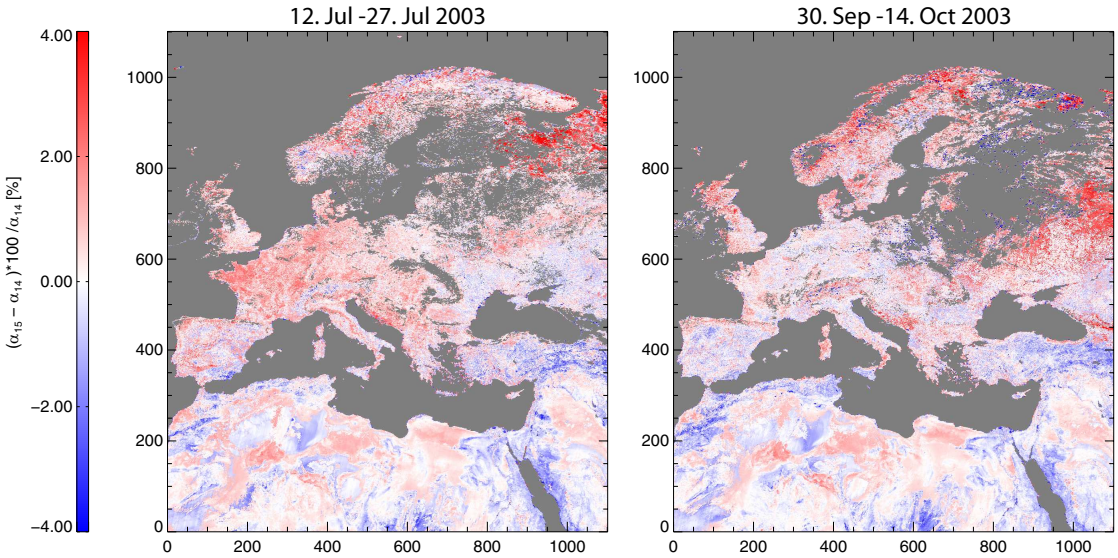

Figure 4.3.2: Calculated differences in spectral albedo of MERIS channel 15 and 14 taken from the ALBEDOMAP dataset given in percentage. The left image show the mean differences for a period from 12 July to 27 July 2003. The right image show the mean difference for a period from 30 September to 22 October 2003.

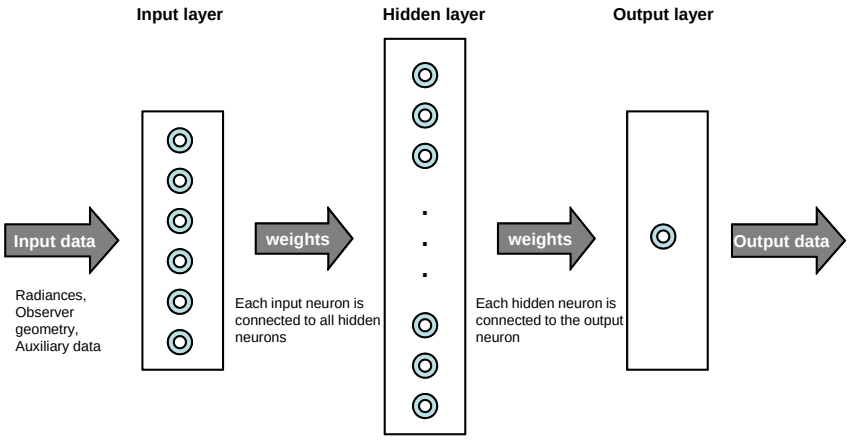

Figure 4.4.1: Conceptual overview of the proposed ANN for the water vapor retrieval

MERIS radiances at top of atmosphere, an artificial neuronal network (ANN) was used. Its free parameters, so called weights were estimated during a supervised learning procedure based on a least mean squares approach. Samples, pulled out from the simulated dataset, were present to the network and its output is compared against the expected output as given in the database. This had to be done sequentially for all datasets until the difference between the network output and the expected output was minimal. For the network training the back-propagation algorithm (Rumelhart et al., 1986) was used.

The network applied here consisted of three layers of neurons, an input layer, an hidden layer and an output layer. A conceptional overview is shown in Figure 4.4.1. It had six input and one output neuron(s), each connected to the 60 hidden neurons. This allowed to perform a highly non linear function approximation. The six input neurons were associated to the input parameters defined in table 4.3, while the output neuron was associated to the integrated water vapor.

4.4.1 Auxiliary data of the water vapor ANN - the surface albedo ratio $\rho_{15/14}$

This section describes the surface albedo ratio auxiliary data that is needed as input for the water vapor ANN. There are two ways to retrieve the surface albedo ratio $\rho_{15/14}$:

1. read it from FUB-albedo dataset, based on the ALBEDOMAP database
2. estimate it by linear extrapolation of measured normalized spectral radiances L^N_{13},

L_{14}^N

The normalized spectral radiance for the channel i (L_i^N) is the ratio of the spectral radiance in this channel and the solar constant in this channel (S_i^0): $L_i^N = L_i/S_i^0$

The FUB-albedo product was retrieved from the ALBEDOMAP datasets applying a regression of nine standard surface albedo spectra (subsection 4.3.3). The dataset was provided as a part of three FUB-albedo products (black-sky albedo[1] band 11, 15 and the ratio of black-sky albedo band 15 and band 14) as a DIMAP 2.3.0[2] data format. Each product is a 16 days mean. The data products are accessible at Brockmann Consult FTP Server.

When the FUB-albedo product was not available due to data gaps within the product, the estimate of the surface albedo ratio between band 15 and band 14 was calculated as a simple linear extrapolation of radiances, measurements in band 13 and band 14:

$$\alpha_{13} = L_{13}^N \cdot \pi / \cos(\theta_{SUN}) \tag{4.4.1}$$

$$\alpha_{14} = L_{14}^N \cdot \pi / \cos(\theta_{SUN}) \tag{4.4.2}$$

$$\alpha_{15} = [7/4 \cdot [\alpha_{14} - \alpha_{13}]] + \alpha_{13} \tag{4.4.3}$$

$$\rho_{15/14} = \alpha_{15}/\alpha_{14} \tag{4.4.4}$$

Both ways were implemented for the water vapor retrieval algorithm, since both have advantages and disadvantages. As an example the surface albedo ratio $\rho_{15/14}$ taken from the FUB-albedo product for a period from 12 July to 27 July 2003 and from 30 September to 22 October 2003 is shown in Figure 4.4.2.

A flowchart of the water vapor algorithm is shown in Figure 4.4.3, showing the input and output data.

4.4.2 Input and output of the water vapor ANN

The input and output of the water vapor over land artificial neuronal network (ANN) which is used for the retrieval of integrated water vapor over land areas is given in this

[1] Black-sky albedo (directional hemispherical reflectance): is defined as albedo in the absence of a diffuse component and is a function of solar zenith angle

[2] http://www.brockmann-consult.de/beam/doc/help/general/BeamDimapFormat.html

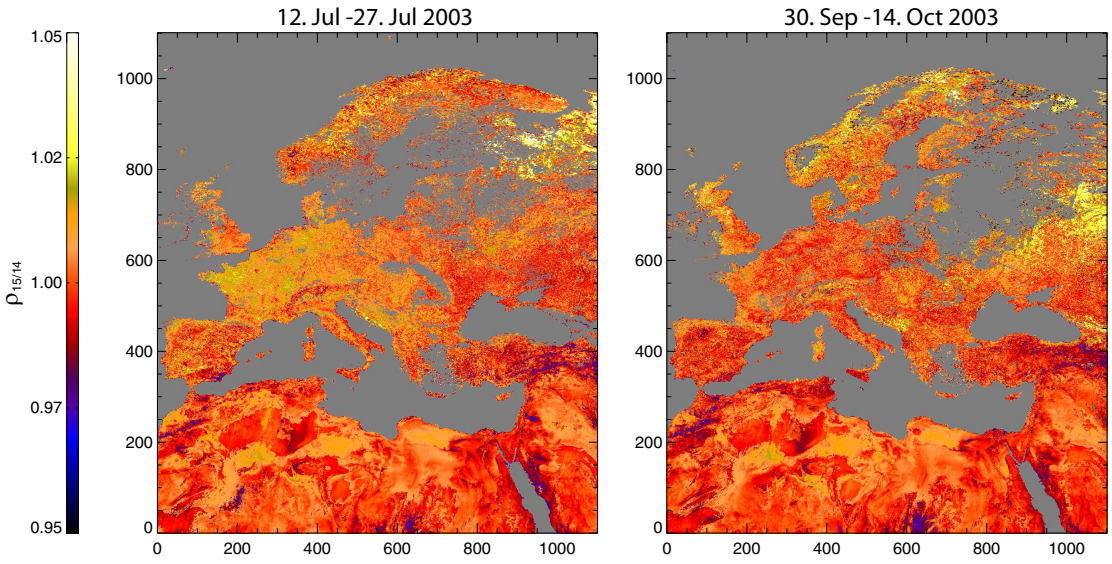

Figure 4.4.2: The surface albedo ratio $\rho_{15/14}$ taken from the FUB-albedo product for a period from 12 July to 27 July 2003 and from 30 September to 22 October 2003. The 16 days period is a result of the used ALBEDOMAP product from which the FUB-albedo product was calculated.

section. All required parameters are tabulated in Table 4.3. The input of the water vapor over land ANN is a 10 element-tuple of floats containing:

1. $\cos(\theta_{SUN})$ the cosine of the sun zenith angle,
2. $\cos(\theta_{VIEW})$ the cosine of the viewing zenith angle,
3. $\sin(\theta_{VIEW})\cdot\cos(\phi_{DIFF})$ the azimuth difference in cartesian coordinates. Note, that ϕ_{DIFF} is defined as in MOMO, which is the opposite to MERIS. As an orientation: For $\phi \approx 0$ sun glint is expected.
4. L_{14}^N the spectral radiance in channel 14. Note: this spectral radiance is normalized by the solar constant S^0: $L_{14}^N = L_{14}/S_{14}^0$
5. $\rho_{15/14} = \alpha_{15}/\alpha_{14}$ the surface albedo ratio of channel 15 and 14. This value will be provided as an auxiliary data file (section 4.4.1).
6. τ_{H_2O} the estimated optical depth of water vapor : $\tau_{H_2O} = -\ln(L_{15}^N/L_{14}^N)$, with $L_x^N = L_x/S_x^0$

The output of the water vapor ANN is the integrated columnar water vapor content (IWV) over cloud free land areas in $\frac{g}{cm^2}$ (Table 4.4). The next section show three

examples of the application of the developed water vapor ANN to MERIS level-1b data[3]. The water vapor algorithm is applicable to reduced resolution and full resolution MERIS level-1b data.

4.5 Application to MERIS data

In this section, examples of successful application of the water vapor algorithm to MERIS level-1b-data are presented. Figure 4.5.1 show the first example based on MERIS level-1b data taken on 9th of May 2008 over Northeast Germany. The left picture shows the retrieved integrated water vapor and the right picture shows the corresponding true color image. The MERIS true color image show an almost cloud free scene. In order to be sure no thin cirrus occurred in that scene, additionally AATSR data was used for clod detection (Figure 4.5.2). The AATSR instrument can detect thin cirrus clouds by measuring its thermal emission. In the AATSR data no cloud over Northeast Germany was detected (clouds would have temperatures below 260K). The MERIS water vapor data show a narrow belt of dry air along a line from the Bay of Kiel to the Erzgebirge. The large scale weather situation for 9th of May is shown in Figure 4.5.4 (b). A so

[3]Level-1b data: level-1a data that have been processed to sensor units ans radiometrically corrected and geolocated

In	Parameter	Type		Minimum	Maximum	Units
1	cosine of the sun zenith angle	float	$\cos(\theta_{SUN})$	3.42E-01	9.48E-01	dim.less
2	cosine of the viewing zenith angle	float	$\cos(\theta_{VIEW})$	6.80E-01	1.00E+00	dim.less
3	azimuth difference in cartesian coordinates	float	$\sin(\theta_{VIEW}) \cdot \cos(\phi_{DIFF})$	-7.33E-01	7.33E-01	dim.less
4	radiance in channel 14	float	L_{14}^{N}	4.10E-03	1.98E-01	sr^{-1}
5	surface albedo ratio	float	$\rho_{15/14}$	8.99E-01	1.07E+00	dim.less
6	estimated optical depth of water vapor	float	τ_{H_2O}	3.56E-02	8.63E-01	dim.less

Table 4.3: Input parameters for the water vapor artificial neuronal network (ANN).

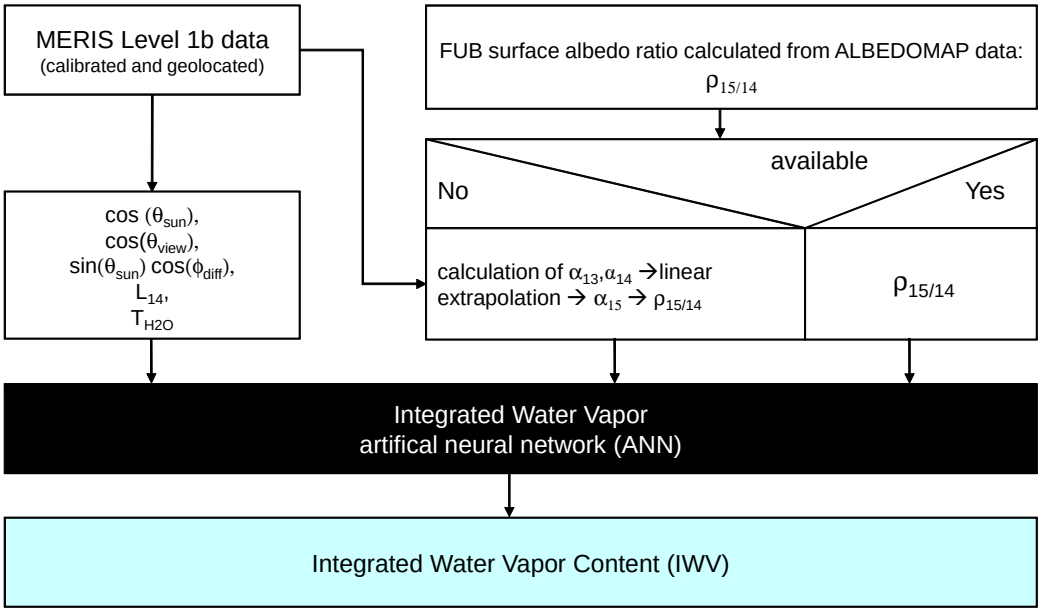

Figure 4.4.3: Flowchart of the input and output of the water vapor artificial neuronal network (ANN).

called "omega" condition is observable. The "omega" condition is characterized by two low-pressure areas that inhibit a move from a between high-pressure area. It is a stable weather condition. At the front side of the high-pressure area, air moves down leading to an air divergence at bottom. That air divergence could lead to the dry air belt shown in Figure 4.5.1.

The application of the water vapor algorithm to full resolution data for the same date is shown in Figure 4.5.3. The advantage of the full resolution mode of MERIS is the high spatial resolution of the data. The full resolution MERIS water vapor data show fine structures. It defines the wind corridor that is shown in Figure 4.5.4 (a).

Two days later, on 11th of May 2008 the large scale weather situation over Central

Out	Parameter	Type		Minimum	Maximum	Units
1	integrated columnar water vapor content over cloud free land areas	float	IWV	1.30E-01	7.63E+00	g/cm^2

Table 4.4: Output parameters of the water vapor artificial neuronal network (ANN).

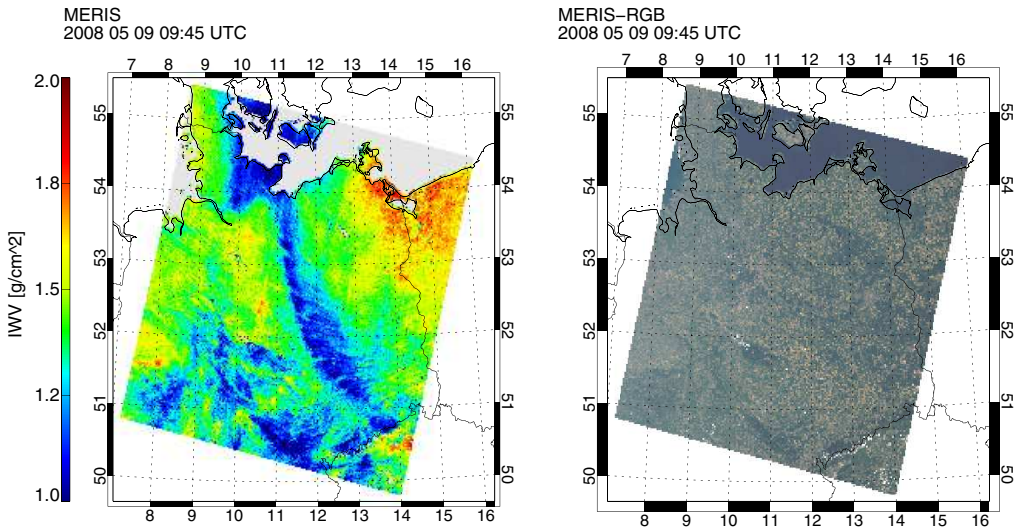

Figure 4.5.1: Integrated water vapor (IWV) retrieved by applying the water vapor artificial neuronal network (ANN) to MERIS reduced resolution level-1b data taken on 9th of May 2008 over Northeast Germany (left). The right picture show the corresponding true color image (RGB).

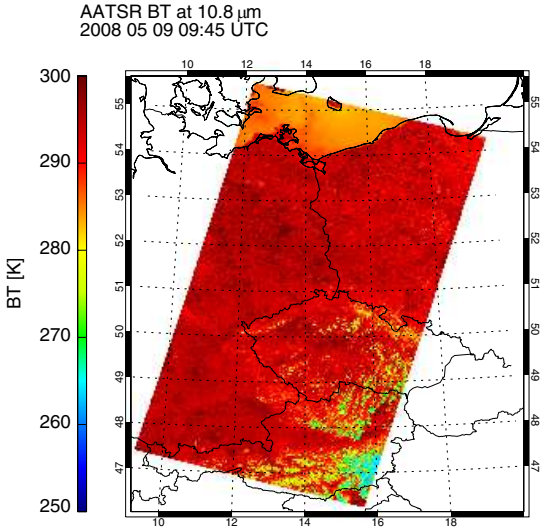

Figure 4.5.2: AATSR brightness temperatures @ 10.8 μm taken on 9th of May 2008 09:45 UTC over East Germany

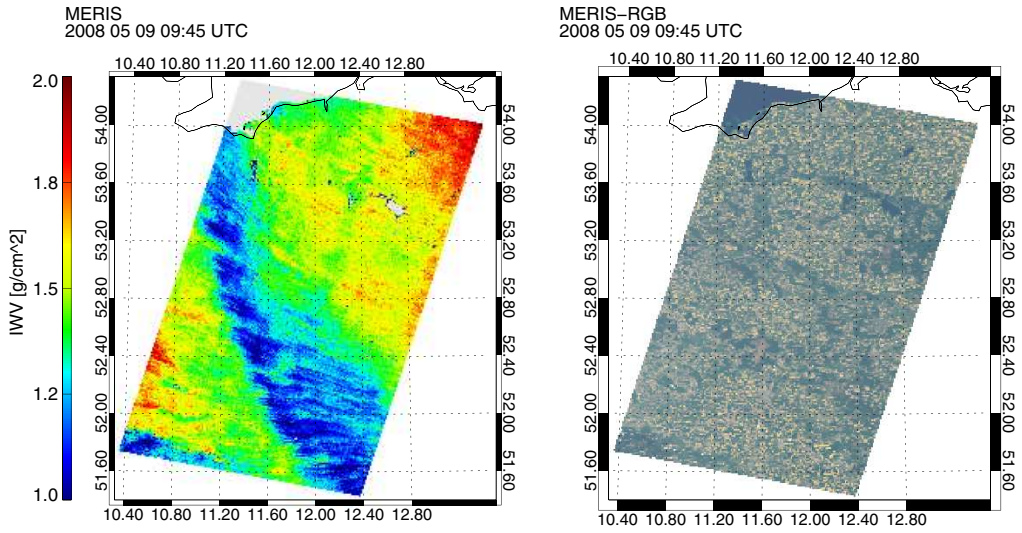

Figure 4.5.3: Integrated water vapor (IWV) retrieved by applying the water vapor artificial neuronal network (ANN) to MERIS full resolution level-1b data taken on 9th of May 2008 over Northeast Germany (left). The right picture show the corresponding true color image (RGB).

Europe was still dominated by a stable "omega" condition. North Germany was under the influence of the high pressure area "MARCO". The MERIS water vapor algorithm was applied to full resolution level-1b-data taken at 10:22 UTC on that day. The upper image in Figure 4.5.5 show the true color image of North Germany. The white square marks the subset of the scene for that the MERIS water vapor algorithm was applied. The resulting water vapor field and the corresponding true color image is shown in Figure 4.5.5. The red square mark the area of interest with high water vapor values. It is possible that the high water vapor values are due to surface evaporation in combination with the lack of air exchange across the high pressure area. The rising sun could initiate this evaporation leading to convective cloud development. To verify this assumption, high resolution visible (HRV) data acquired by the Meteosat Second Generation (MSG) data was analyzed. Figure 4.5.6 show the MSG data for four different times: at 10:15, 10:30, 10:45 and 11:00 UTC. The convective cloud development is clearly visible in the red square.

In the next example, the water vapor algorithm was applied to MERIS reduced resolution data taken 12th of August 2003 over the Western Po basin, the Southwest Alps and the Côte d'Azur. The MERIS water vapor and the corresponding MERIS true color

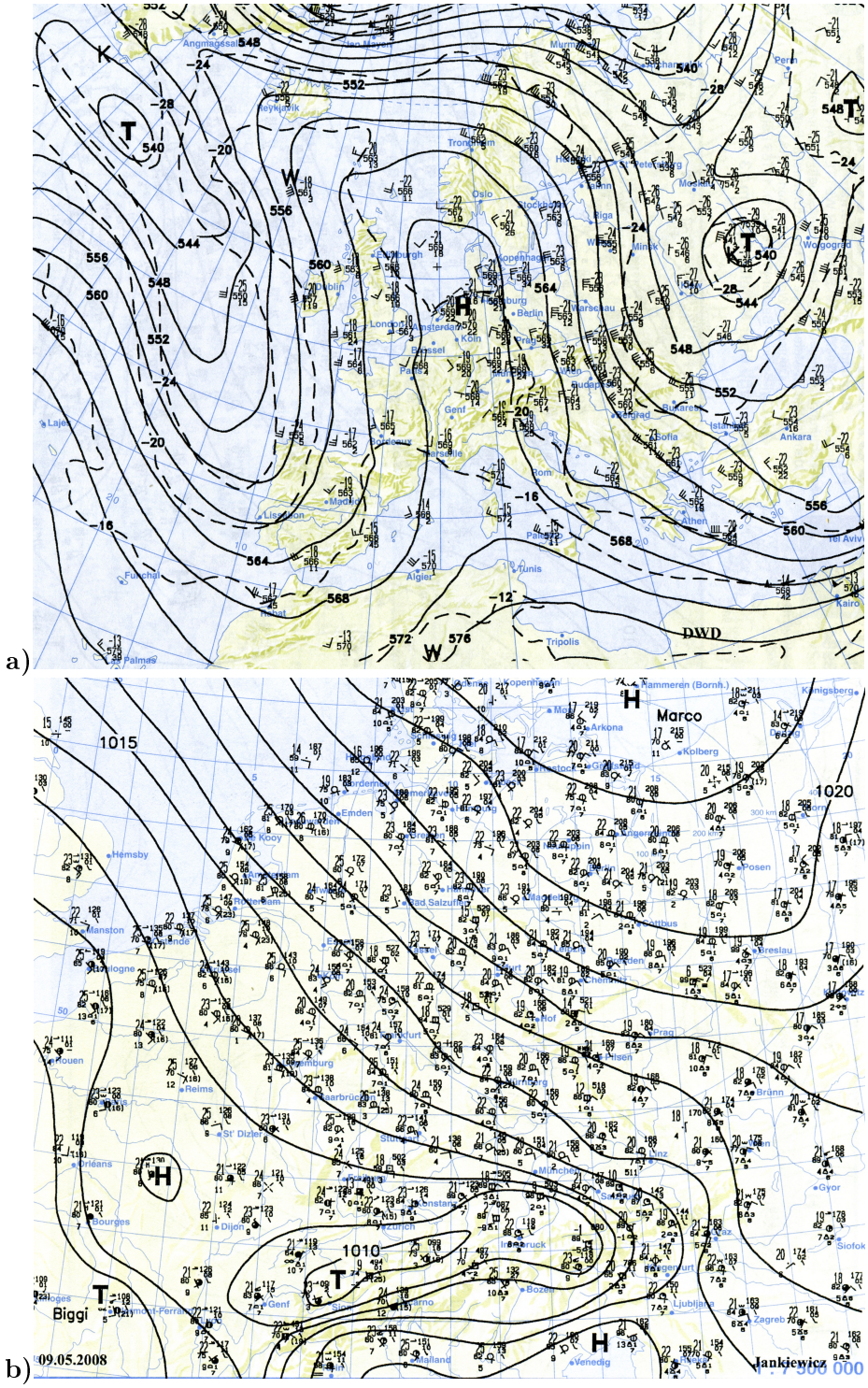

Figure 4.5.4: Isobars and isotherms at 500hPa for 9th of May, 00h UTC (a). The soil pressure and the measurements of the SYNOP stations for 9th of May, 12h UTC are shown in (b). The images are taken from the "Berlinder Wetterkarte" (http://wkserv.met.fu-berlin.de/)

image is shown in Figure 4.5.7 a). The Po basin and the coastal areas are lower than the surrounding mountains and the air next to the Mediterranean Sea can be expected to contain more water vapor, both leading to increased water vapor values. This is well represented in the water vapor field were the Po basin as well as the Côte d'Azure show high water vapor values. The dependency of water vapor on height is also observable in the Alps were the valleys have higher integrated water vapor values compared to the summits of the mountains. The transection in Figure 4.5.7 b) also indicate the height dependence of the water vapor. Over the whole transection the water vapor is generally as expected anti-proportional to the surface height.

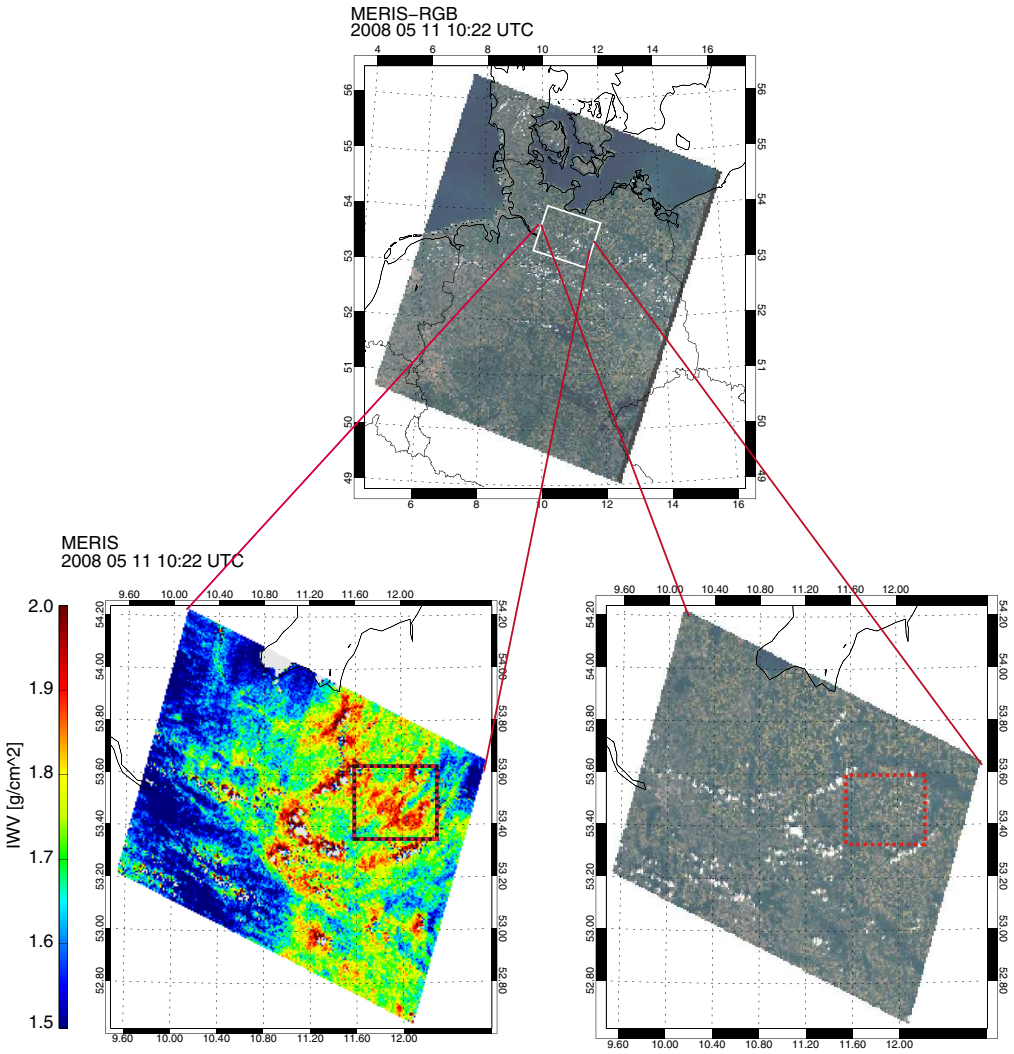

Figure 4.5.5: Integrated water vapor (IWV) retrieved by applying the water vapor artificial neuronal network (ANN) to MERIS full resolution level-1b data taken on 11th of May 2008 10:22 UTC over North Germany (processed by Hannes Diedrich). The upper and lower lower right image show the corresponding true color image (RGB). The red square mark the area of interest with high water vapor values. In the true color image small lines of clouds are observable.

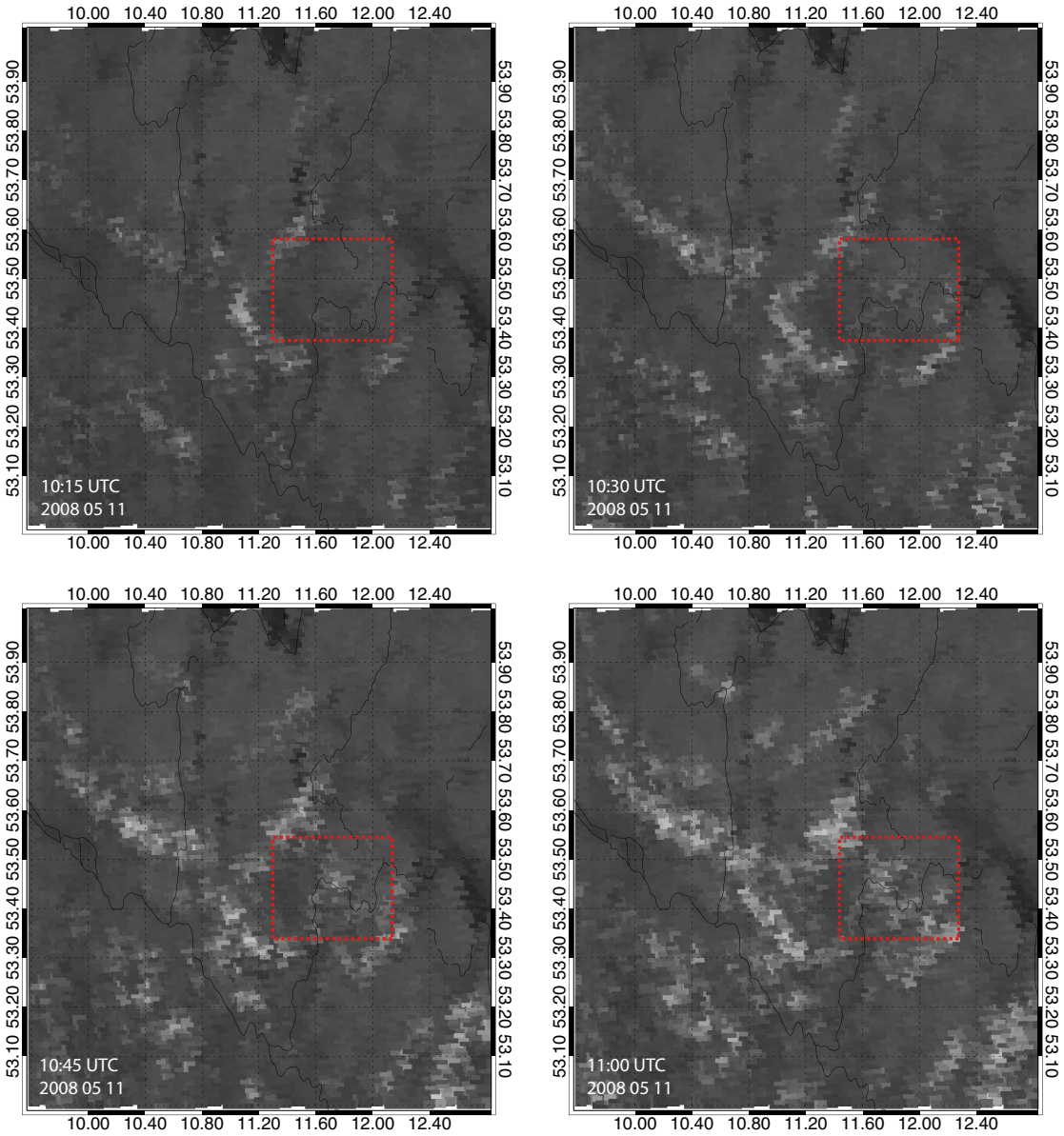

Figure 4.5.6: Shown are high resolution visible (HRV) data taken by Meteosat Second Generation (MSG) on 11th of May 2008 at 10:15, 10:30, 1045 and 11:00 UTC (provided by Stefan Stapelberg, processed by Hannes Diedrich). The bright areas indicate clouds. The red square corresponds with the red square in Figure 4.5.5 and indicate the area of interest where cloud development take place.

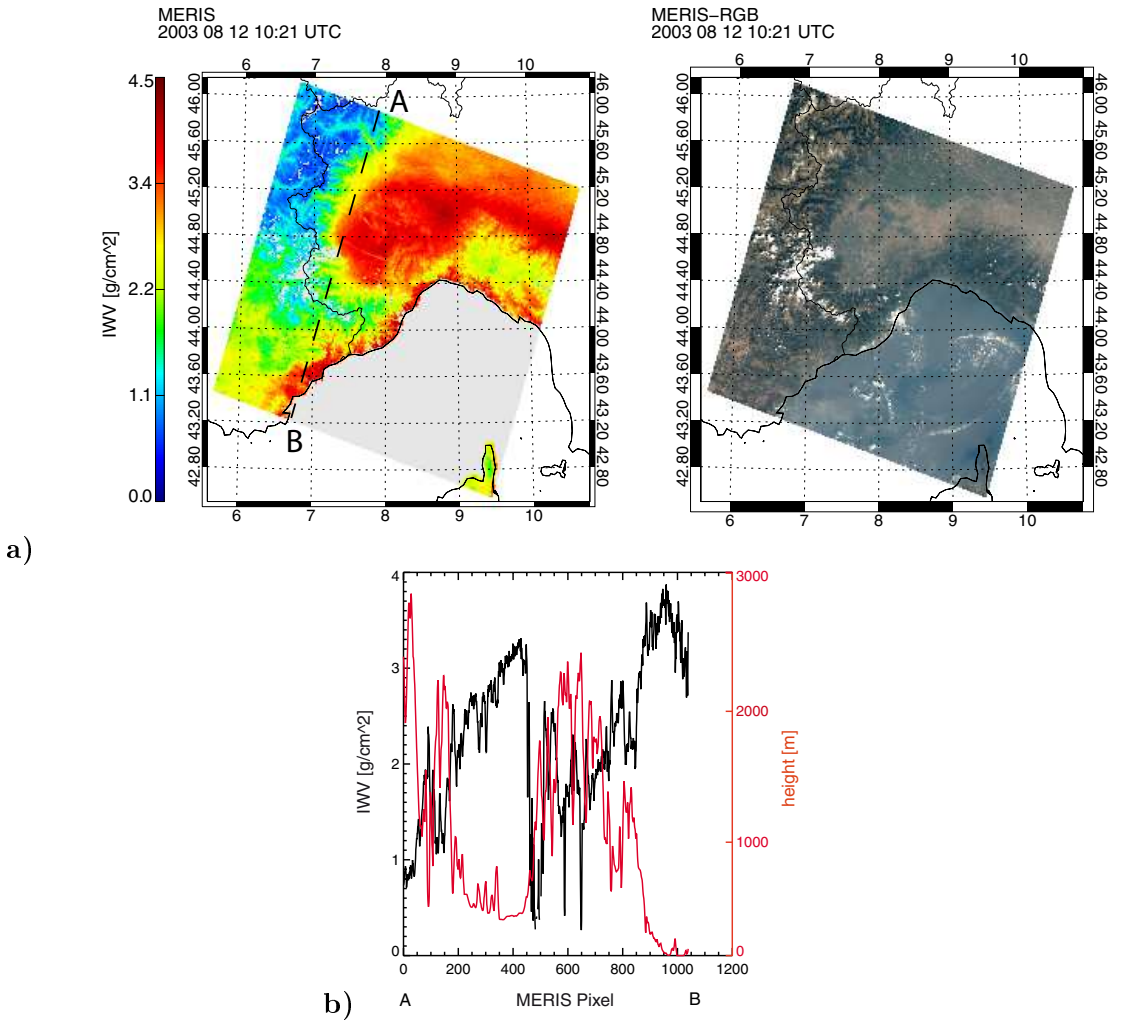

Figure 4.5.7: Integrated water vapor (IWV) retrieved by applying the water vapor artificial neuronal network (ANN) to MERIS FR level-1b data from 12th August 2003 (a). The shown scene covers the Western Po basin, the Southwest Alps and the Côte d'Azur. The upper right image show the corresponding true color image (RGB). A transection of the surface height and the water vapor following a line from point A to point B (image (a)) is shown in (b).

5 Validation of the MERIS water vapor algorithm

For validation purposes, the new MERIS water vapor retrieval were compared to three different sources of in situ measurements: 1. measurements of integrated water vapor taken by Microwave Radiometers (MWR) on the ARM-SGP site in Oklahoma / USA; 2. ground based GPS stations in Germany and; 3. radio soundings over Central Europe. The validation was done for a period of three years from January 2003 to December 2005. In the next sections the validations results are shown.

5.1 Validation with Microwave Radiometers

The Microwave Radiometer (MWR) receives microwave radiation from the sky at 23.8 GHz and 31.4 GHz. Measurements in these two frequencies allow determination of water vapor and liquid water along a selected path. The method is described in Liljegren (2000); Han and Westwater (1995). The accuracy of water vapor measurements is within the very high order of 0.3mm (Turner et al., 2003).

For validation purpose, the data were collected from four different microwave radiometers on the ARM-SGP site in Oklahoma (Figure 5.1.1). The triangle flag the geographical position of the stations. The size of the triangle indicate the number of observations that were used for comparison while the color denote the height of the station. The microwave radiometer water vapor measurements were provided with a temporal resolution of one second. For each day in which microwave radiometer and MERIS data were available and the appropriate MERIS pixel was cloud free, the microwave radiometer measurement was compared to the MERIS pixel. 794 collocations were found within the time frame of three years. The validation result is presented in a scatter plot shown in Figure 5.1.1. The one by one line is plotted in black and the regression line in red, colors denotes data density with small values in blue and large values in red. The agreement between MERIS and microwave radiometer measurements is very high, with a root mean square deviation of 1.64mm and a bias of -0.03mm. This is slightly below the observed trend in

global water vapor, but in the same order of magnitude of 2mm per decade (Vonder Haar et al., 2005; Trenberth et al., 2005).

5.2 Validation with GPS

A second validation was performed using ground based Global Positioning System (GPS) measurements. The Global Positioning System comprises 29 navigation satellites at an altitude of 20,200km. For precise determination of position a ground based GPS receiver receives carrier phase measurements from a part of the satellites simultaneously. It estimates parameters such as receiver coordinates. For precise navigation it is necessary to mitigate all sources of error that affect carrier phase measurement. A major source of error is the atmospheric water vapor affecting the speed of signal propagation. However, since its value depends on the amount of water vapor, it can be used for water vapor retrieval. This delay is defined as Zenith Total Delay (ZTD) and is usually divided into two components, the Zenith Hydrostatic Delay (ZHD) and the Zenith Wet Delay (ZWD):

$$ZTD = ZHD + ZWD \tag{5.2.1}$$

The hydrostatic part can be modeled with high accuracy, while the wet component is poorly predicted by models. The ZWD can be calculated by subtracting ZHD from ZTD and therefore the atmospheric integrated water vapor (IWV) is computed using the relationship:

$$IWV = \pi ZWD \tag{5.2.2}$$

where π is a combination of a constant proportionality, a function of various physical constants, and of the mean temperature in the atmosphere. π is calculated by a linear regression from radio soundings. However, it is the main uncertainty when converting ZWD to IWV.

For the validation GPS measurements provided by the GFZ[1] Potsdam were used. The data were available for 153 Stations located in Central Europe shown in Figure 5.2.1. The size of the triangles indicate the number of valid observations that were used for the comparison. The height of each GPS station is given by the color of the triangle. The water vapor product is generated each hour with a 30-minute time resolution and an accuracy of ±1-2mm (Gendt et al., 2004). For each day in which MERIS data were available, the satellite pixels closest to each GPS station were used for comparison. Cloud free pixels were taken into account if the time difference between the MERIS overpass

[1] Deutsches GeoForschungsZentrum

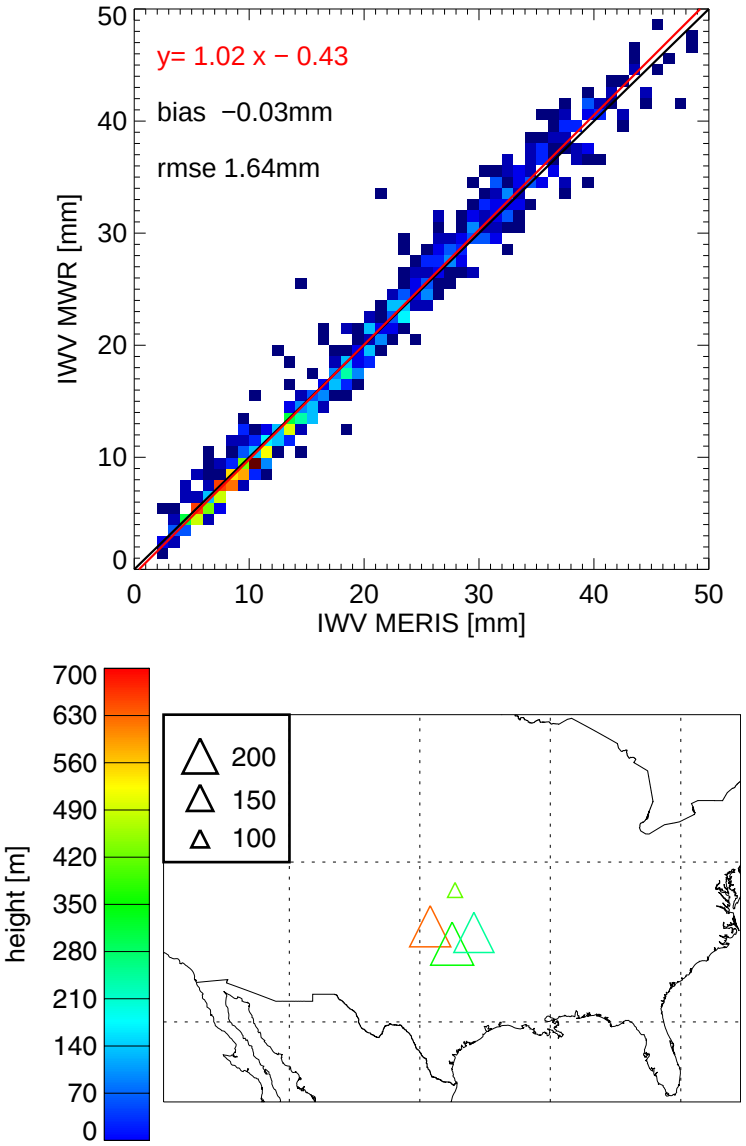

Figure 5.1.1: Integrated water vapor from MERIS and Microwave Radiometer at ARM-SGP site. The upper panel show the scatter plot of 794 collocations for a period of three years. The color indicates the data density of collocations with high values in red and small values in blue. The lower panel illustrates the location of the four used microwave radiometer stations. The size of the triangles denotes the number of observations used for the comparison, while the color indicates the height of the MWR-station.

and the GPS measurements, was less than 30 minutes. 4424 collocations were found. The result for the validation of all 4424 collocations is presented in Figure 5.2.1. The one by one line is plotted in black and the regression line in red, the colors denote the data density. The agreement between MERIS and GPS measurements is very high, with a root mean square deviation of 1.22mm and a bias of 0.97mm. This values are is in the range of the accuracy of the GPS-water vapor product. The bias is higher compared to the validation to microwave radiometer, the root mean square error is slightly below.

In addition to the validation, a study of the bias between GPS and MERIS water vapor measurements was performed. For this study the differences of the water vapor measurements taken by GPS stations and MERIS were plotted against the surface albedo ratio, surface temperature, and surface pressure at the corresponding GPS station. This was done to estimate the influence of each parameter on the MERIS water vapor retrieval accuracy.

Figure 5.2.2 (left) shows the spectral albedo ratio $\rho_{15/14}$ at each GPS station for every validation match-up accumulated in monthly bins for the validation period. The solid line denotes the monthly mean of the spectral albedo ratio $\rho_{15/14}$. A slight seasonal cycle due to the change in vegetation is observable. The right panel shows a scatter plot of the spectral albedo ratio $\rho_{15/14}$ and the water vapor difference between the GPS and MERIS measurement. The color denotes the data density. No significant correlation between the spectral albedo ratio $\rho_{15/14}$ and the difference between the GPS and MERIS water vapor measurement is observable.

Figure 5.2.3 (left) shows the surface temperature at each GPS station for every validation match-up accumulated in monthly bins for the validation period. The solid line denotes the monthly mean of the temperature. The typical seasonal cycle with high temperatures in summer and low temperatures in winter is visible. The right panel shows a scatter plot of the temperature and the water vapor difference between the GPS and MERIS measurement. The color denotes the data density. Again no significant correlation between the temperature and the difference between the GPS and MERIS water vapor measurement is observable.

Figure 5.2.4 (left) shows the surface pressure at each GPS station for every validation match-up accumulated in monthly bins for the validation period. The solid line denotes the monthly mean of the surface pressure. No seasonal cycle is visible for the monthly mean of surface pressure. The right panel shows a scatter plot of the surface pressure and the water vapor difference between the GPS and MERIS measurement with the colors denoting the data density. A slight dependence of the water vapor difference to surface pressures over 1013hPa is visible, however further investigations are needed.

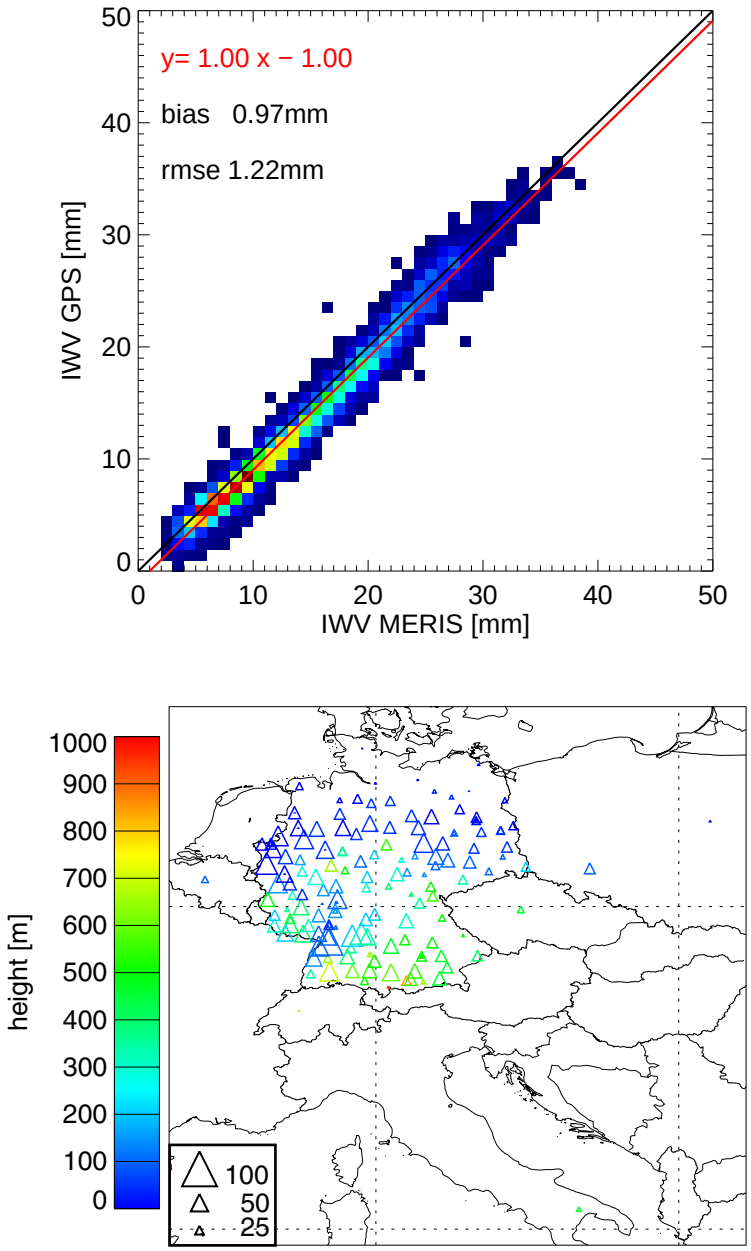

Figure 5.2.1: Integrated water vapor from MERIS and from GPS measurements located in Central Europe. The upper panel shows the scatter plot of 4424 collocations for a period of three years. The color indicates the data density of collocations with high values in red and small in blue. The lower panel illustrates the location of the 153 used GPS-receivers. The size of the triangle denotes the number of observations used for the comparison, while the color indicates the height of the GPS-station.

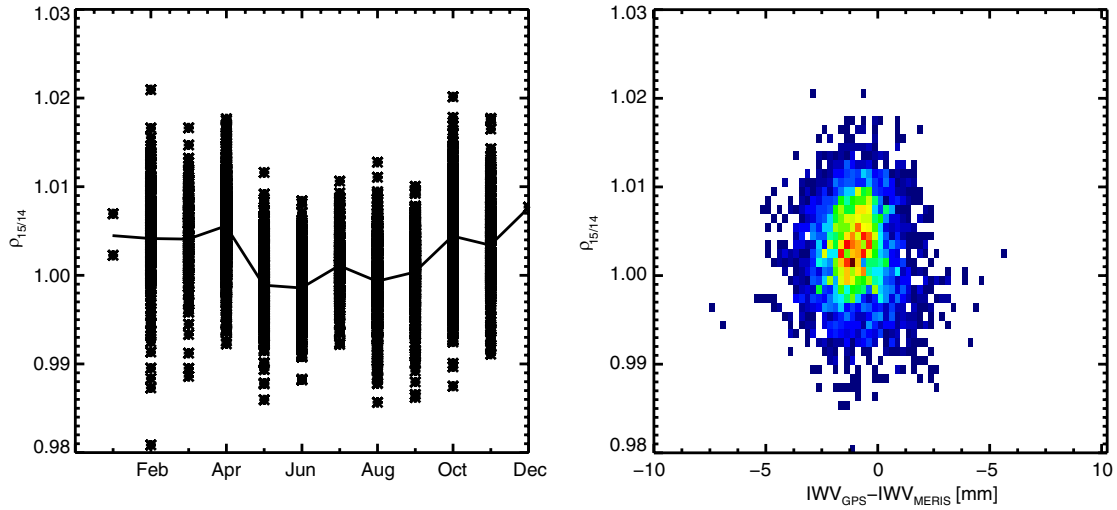

Figure 5.2.2: On the left is shown the spectral albedo ratio $\rho_{15/14}$ at each GPS station for every validation match-up, and with monthly binning for the three year validation period. The solid line denotes the monthly mean of the spectral albedo ratio $\rho_{15/14}$. The right panel shows a scatter plot of the spectral albedo ratio $\rho_{15/14}$ against the water vapor difference between the GPS and MERIS measurement. The color denotes the data density with high values in red and low values in blue.

In summary the study showed that the differences between the GPS and MERIS water vapor measurements are not correlated to the surface albedo ratio $\rho_{15/14}$ and the surface temperature. A slight dependence to the surface pressure is observable but validation data with a wider range of surface pressure cases are needed for further investigations.

5.3 Validation with radio soundings

Furthermore, validation analysis was performed with radio soundings. Radiosondes are designed for operational use in weather forecasting. Currently at least two radio soundings are launched per day. The advantage of radio soundings is that they perform vertical resolved measurements of the temperature, pressure, and relative humidity profile. With these measurements the integrated water vapor amount along the ascent path can be calculated. However, radio soundings are expected to have larger retrieval errors for water vapor measurements in comparison with MWR or GPS measurements (Turner et al., 2003; Miloshevich et al., 2009; Vömel et al., 2007).

For comparison water vapor measurements of 37 radio sounding stations over Europe

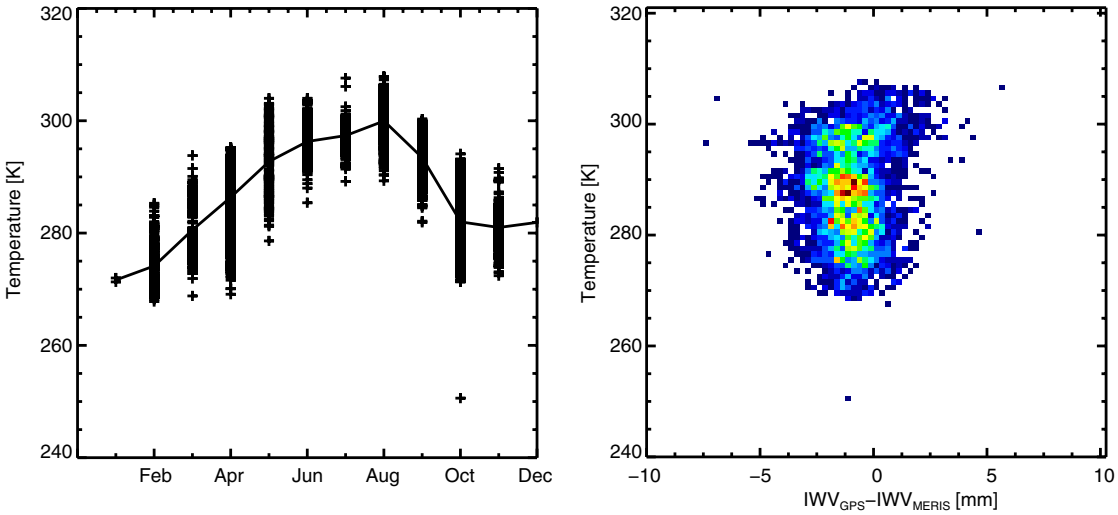

Figure 5.2.3: On the left is shown the temperature in [Kelvin] at each GPS station for every validation match-up, and with monthly binning for the three year validation period. The solid line denotes the monthly mean of the temperature. The right panel shows a scatter plot of the temperature and the water vapor difference between the GPS and MERIS measurement. The color denotes the data density with high values in red and low values in blue.

were used. Figure 5.3.1 shows the geographical location of the radio sounding stations. The size of the triangles indicates the number of observations that were used for comparison while the color of each triangle gives the height of the station. The data was collected from the Department of Atmospheric Science of the University of Wyoming. Since operational radio soundings were launched at 12 UTC while the MERIS crossing time for Western and Central Europe was between 10 UTC and 14 UTC, which led to time differences of up to 4 hours. Therefore, the comparison was performed for all available radio soundings where the satellite overpass was less than two hours before and after the radio sounding launch. Since radiosondes can significantly travel horizontally during ascent, for each satellite overpass the mean water vapor amount for all cloud free pixels in the vicinity (<15km) of each radio sound station was calculated. To ensure cloud free conditions for the comparison of a radio sounding and a MERIS water vapor measurement, the cloud fraction of the 15km vicinity had to be less than 5%. 2626 collocations were found (5.3.1).

The validation results in scatter plots are shown in Figure 5.3.1. The one by one line is plotted in black and the regression line in red. The colors denote the data density with

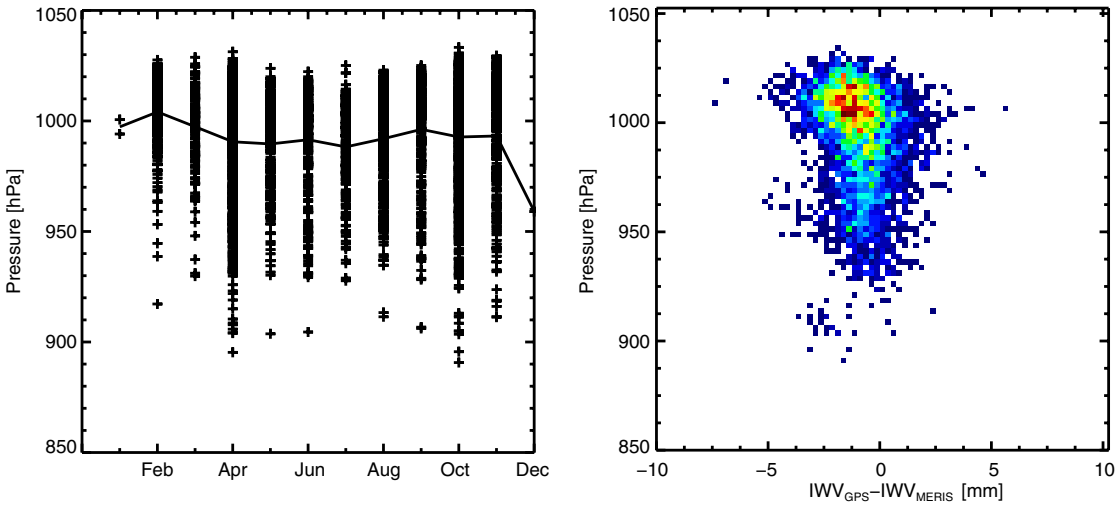

Figure 5.2.4: On the left is show the surface pressure in [hPa] at each GPS station for every validation match-up, and with monthly binning for the three year for the validation period. The solid line denotes the monthly mean of the surface pressure. The right panel shows a scatter plot of the surface pressure and the water vapor difference between the GPS and MERIS measurement. The color denotes the data density with high values in red and low values in blue.

large density in red and small density in blue. The agreement between MERIS and radio sounding measurements is good, with a root mean square deviation of 2.28mm and a bias of 1.63mm. However, for increasing water vapor values the difference between water vapor retrieved from MERIS and radio soundings increases. This feature could not be seen for the validation with microwave and GPS. Also, the tendency of higher differences for higher water vapor corresponds with findings with findings of a long term comparison between water vapor retrieved from radio sounds and microwave radiometers (Turner et al., 2003; Miloshevich et al., 2009; Vömel et al., 2007). The comparison revealed a 5% dry bias of the radio sounds. This is in agreement with the bias of 7% observed in this work.

5.4 Validation summary

All validation results are summarized in Table 5.1. For each validation dataset the root mean square error as well as the bias was calculated. The agreement between MERIS and in situ measurements is very high. The best validation result is observable for

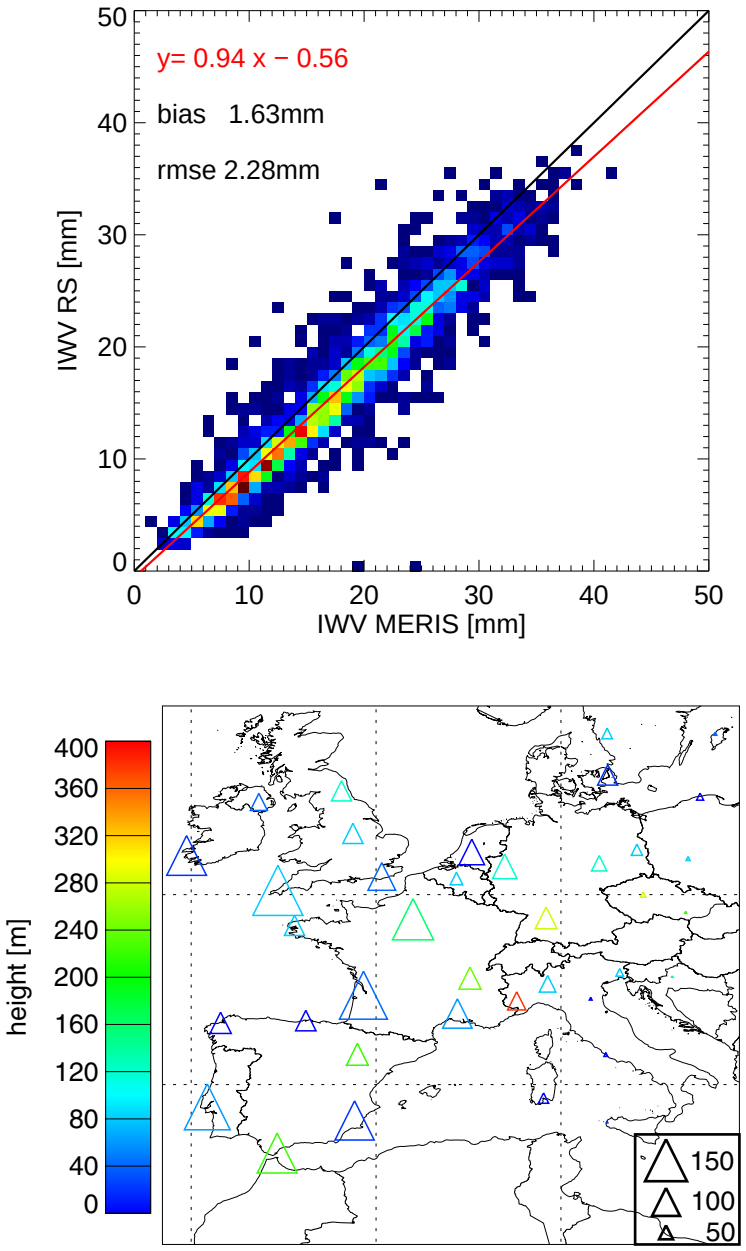

Figure 5.3.1: Integrated water vapor from MERIS and from radio soundings launched in Europe. The upper panel shows the scatter plot of the 2626 collocations for a period of three years. The color indicates the data density of collocations with high values in red and small in blue. The lower panel illustrates the location of the 38 used radiosonde stations. The size of the triangle denotes the number of observations used for the comparison, while the color indicates the height of the radiosonde stations.

	rmse [mm]	bias [mm]
MWR-data	1.64	-0.03
GPS-data	1.22	0.97
Radio soundings	2.28	1.63

Table 5.1: Summary of all validation analysis performed over three years from January 2003 to December 2005.

the microwave radiometers with a root mean square deviation of 1.64mm and a bias of -0.03mm. For the comparison with GPS measurements a bias of 1mm is shown. This indicates a systematic overestimation of the MERIS water vapor measurements in comparison with GPS measurements. The overestimation of MERIS measurements is not observable for the microwave radiometer validation results. The root mean square deviations for the radio soundings with 2.28mm and the for the GPS measurements with 1.22mm are in the range of the measurement accuracy. The validation results show the high accuracy of the proposed new water vapor algorithm.

6 Verification of COSMO-EU/DE IWV analyses with MERIS IWV measurements

The current spatial resolution of the COSMO-EU model is covering the meso-β scale using a 7km grid spacing while the COSMO-DE model is covering the meso-γ scale using a 3km grid spacing. These spatial resolutions are the highest for European Numerical Weather Prediction (NWP) models. The advantage of these high spatial resolution is resolving the underlaying terrain and smal scale atmospheric processes. This leads to an more accurate numerical prediction of near surface weather, focusing on clouds, fog, frontal precipitation, and orographically and thermally forced wind systems. The high spatial resolution of both models allow a direct simulation of severe weather events triggered by deep moist convection that is highly dependent on the atmospheric water vapor. Therefore the accuracy of the data assimilation is important for the model forecast.

In collaboration with the "Deutsche Wetterdienst" the accuracy of the water vapor analyses of the COSMO-EU and COSMO-DE model have evaluated through a direct comparison of COSMO-EU and COSMO-DE water vapor analyses with independent MERIS water vapor measurements. The MERIS water vapor measurements were processed by applying the new water vapor algorithm (described in chapter 4) to MERIS Level-1b data. The comparison was performed for a period of 3 years (July 2006 to July 2009) for the COSMO-DE model system, and 4.5 years (January 2005 to July 2009) for the COSMO-EU model system.

The first section describes the conversion of the MERIS measurements into the COSMO-EU and COSMO-DE grid size. The next two sections contains the results of the comparison of 1.) MERIS water vapor measurements with COSMO-EU water vapor analyses and; 2.) MERIS water vapor measurements with COSMO-DE water vapor analyses.

6.1 Conversion of MERIS IWV measurements into the COSMO-EU/DE grid size

One general problem for the comparison of model and satellite data is the high spatial resolution of the satellite data. The MERIS water vapor measurements used within this work has a spatial resolution of 1km x 1km while COSMO-EU and COSMO-DE operate with resolutions of approximately 7km x7km and 3km x3km, respectively. In order to have equivalent grid sizes, the resolution of the MERIS measurements was therefore reduced in each case to the appropriate grid box size. Accordingly, the geographic coordinates of all MERIS pixels were transformed into the rotated COSMO-EU and COSMO-DE coordinate system (see section 3.2). This was done by calculating the model grid box number for each MERIS pixel. Since the MERIS water vapor retrieval is only applicable for cloud free land areas, the MERIS cloud mask and land-sea mask were applied to the MERIS water vapor measurements. Then the mean water vapor amount for each model grid box that contains over 65% of cloud free MERIS pixel was calculated. Grid boxes containing less than 65% of cloud free MERIS pixel were marked as cloud covered. This converted MERIS dataset was used for the next steps for the comparison with the COSMO-EU and COSMO-DE water vapor analyses.

6.2 Comparison of MERIS IWV measurements and COSMO-EU IWV analyses

For comparison, the reduced integrated water vapor (IWV) dataset from MERIS (see section 6.1) and the COSMO-EU water vapor analyses[1] were used. Additionally the COSMO-EU cloud mask[2] analyses were used for the detection of cloud free grid boxes. The COSMO-EU data assimilation cycle is generating every hour on the hour model analyses. Since MERIS is a sun-synchronous Instrument and due to the extent of Europe, the acquired MERIS data was made up of multiple flyovers of the MERIS Instrument, with each overpass occurring at a progressively later UTC time. This means that the data for the Eastern parts of the model domain were acquired at 7-8h UTC, whereas for the far Western parts of the model domain the flyover occurs at 14-15h UTC. Because the times of the model analyses and the MERIS flyovers do not exactly overlap, the MERIS data were matched up to the model analyses most closely matched in time (max

[1] COSMO-EU code: 54 TQV vertical integrated water vapor $[kg/m^2]$
[2] COSMO-EU code: 71 CLCT cloud cover total

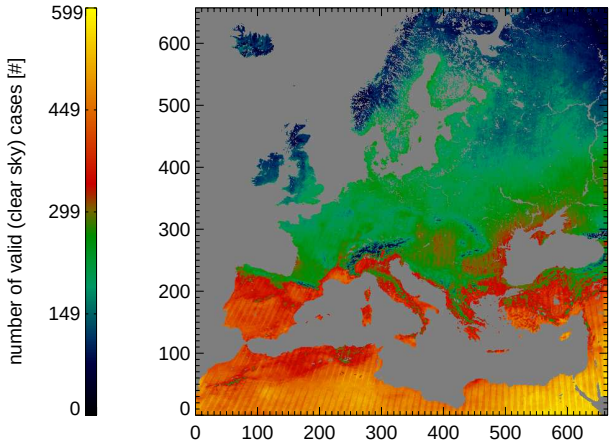

Figure 6.2.1: Total Number of cloud free cases over land detected in the COSMO-EU dataset and in the MERIS dataset for a period of 4.5 years (2005 - 2009)

time difference was 29 minutes). In a next step the COSMO-EU-land-sea-mask[3] was applied to detect land grid boxes. A grid box was detected as land if the land fraction was greater than 0.95 (95%). Finally, each grid box that were detected as cloud free land areas in both datasets were used for the comparison. Only these cases were taken into account for the following statistical analysis.

The resulting total number of cloud free land cases is shown in Figure 6.2.1. For a period of 4.5 years, up to 600 cases per grid box were found for the area of Egypt and Northern Africa. These areas are dominated by desert, leading to more detected cloud free cases. Less cases were found in mountainous areas like the Alps or the Scandinavian Mountains and in the Northern parts of Europe. This could be caused by faulty cloud classifications over snow covered mountain tops of the MERIS cloud mask. These areas are faulty classified as cloud and not taken into account. Additionally due to the seasonal variation in sunlight duration there are less valid cases detected in the Northern parts of the model area. In general a North to South gradient in the total number of cases, with a minimum in the North and a maximum in the South due to the cloud statistic is observable.

Figure 6.2.2 shows the spatial distribution of integrated water vapor for MERIS measurements (left image) and COSMO-EU analyses (right image) averaged for each grid box for the period January 2005 to July 2009. A good qualitative agreement between the two datasets is observable; low water vapor values in mountain regions like the Alps,

[3]COSMO-EU code: 81 FR_LAND land fraction

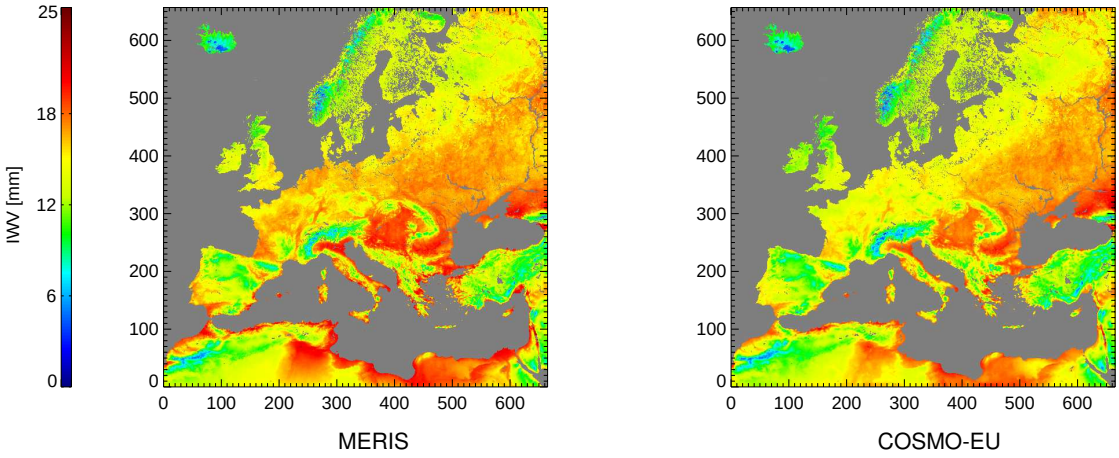

Figure 6.2.2: The mean of integrated water vapor (IWV) for a period of 4.5 years (2005 -2009) retrieved from MERIS (left) and COSMO-EU (right)

the Scandinavian Mountains, the Atlas Mountains, the Pyrenees and the Carpathian Mountains and high values at the Po Basin, the Hungarian Lowlands, the Danube Basin and the coastline of Tunisia, Libya and Egypt are observable. The mean water vapor values ranges from 1mm up to 25mm in both datasets.

A quantitative comparison shows differences between the two datasets in the order of -1mm to -3.5mm (-5.5% to -20%) at regions like Ireland, the Northern Atlantic coastline of France, Denmark, Netherlands as well as for Tunisia and the Nile Delta shown in Figure 6.2.3. In these regions the COSMO-EU water vapor analyses are lower than the MERIS water vapor measurements. COSMO-EU shows higher values compared to MERIS in regions of Russia (North East and Eastern parts of the model area). Differences of up to 2mm (11.1%) are observable for these regions. In general an underestimation of COSMO-EU water vapor analyses in the West and an overestimation in the Eastern parts of the model domain is observed. An inhomogeneous distribution of water vapor differences is apparent for mountainous areas like the Alps, the Dinaric Alps, the Scandinavian Mountains, the Atlas Mountains, the Pyrenees, and the Carpathian Mountains. Representative for these regions the absolute differences for the Alps and Dinaric Alps are shown in Figure 6.2.3. The variability of the water vapor differences is high in high mountains and low in low altitude mountain range. The water vapor differences in regions with significantly surface height variation can be explained by the averaging of the MERIS water vapor measurements. Averaging of MERIS water vapor measurements over different heights should be avoided, because the integrated water vapor does not

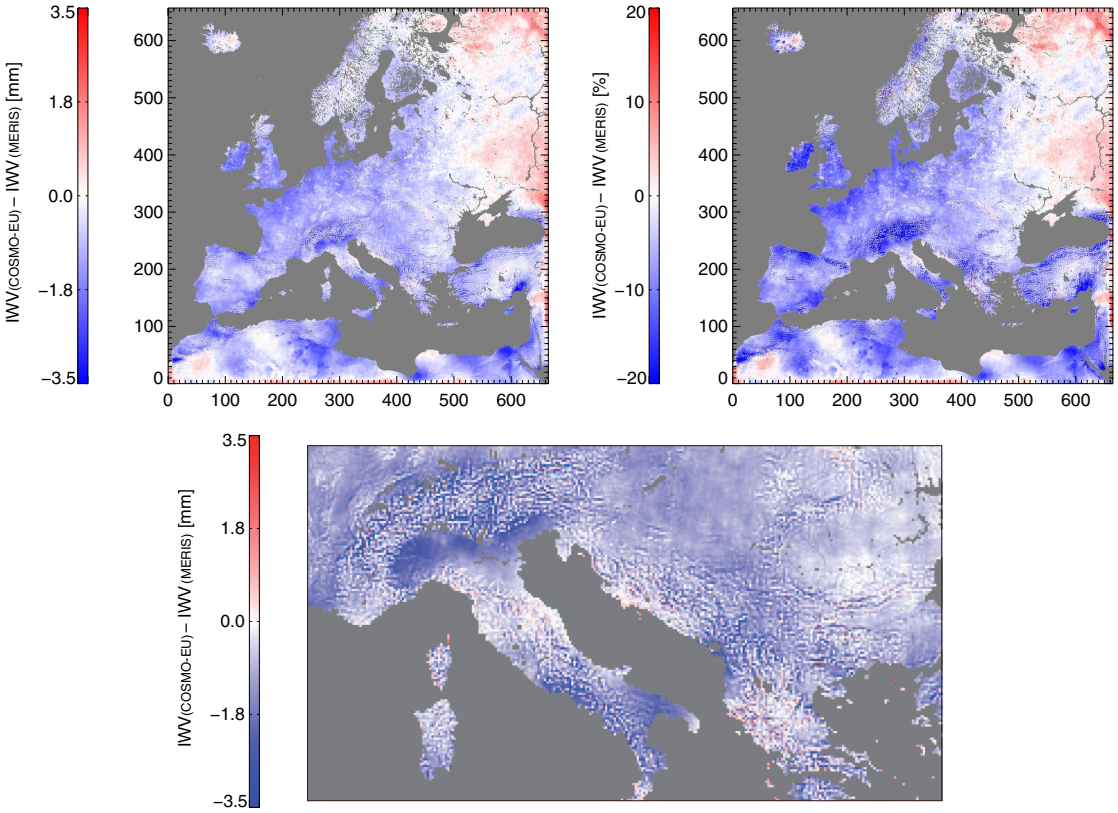

Figure 6.2.3: Differences ($IWV_{COSMO-EU} - IWV_{MERIS}$) of the mean water vapor. The left image shows the absolute values in millimeters [mm] and the right image the relative values in percentage [%]. The lower image shows an enlarged view of the absolute differences in water vapor at the Alps and the Dinaric Alps.

decrease linear with the surface height. However, the comparison was done with the averaged water vapor values that could have led to the deviations in the mean water vapor in the mountains.

Figure 6.2.4 shows the spatial distribution of the variability σ of the MERIS water vapor measurements and COSMO-EU water vapor analyses. The variability σ was calculated for each grid box for a period of 4.5 years. Areas with a high variability of water vapor of up to 10mm are parts of Russia, the Po Basin as well as the Hungarian Lowlands and the Danube Basin. These areas (except the Po Basin) are usually experience by hot summers and colder winters, being far away from the moderating influence of the ocean, which keeps climates milder in winter and cooler in summer. So the high variability of

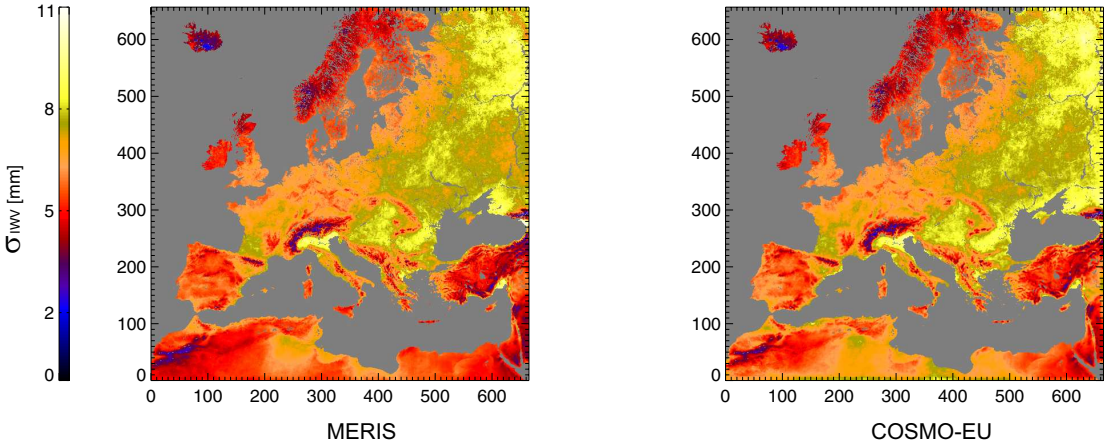

Figure 6.2.4: Variability σ of integrated water vapor for a period of 4.5 years (January 2005 to July 2009) for MERIS (left) and COSMO-EU (right)

the water vapor was expected for these regions. The climate of the Po is typically continental warm in the flat basin area and Mediterranean on the coast leading to the high variability of the water vapor. In Central Europe the variability of the water vapor is moderate with 6mm and for mountainous regions the variability is low in both datasets.

Both datasets are in a good agreement and represents the expected structures in the water vapor variability, however positive differences up to 1.5mm (25%) in North Africa are shown in Figure 6.2.5. In that region the variability σ of the COSMO-EU water vapor analyses are higher compared to the MERIS water vapor measurements. The Central Europe is dominated by heterogeneous distributed small positive and negative differences in the order of 0.5mm (7.5%) and -0.5mm (-7.5), respectively.

Figure 6.2.6 shows the hourly and monthly total number of valid cases of the investigated datasets. Since the MERIS overpass time for the land dominated model domain is between 8h and 11h UTC, a high number of valid cases is shown for that range. The white square marks the range of an adequate amount of valid cases. Only for this time range the results are interpretable. The triangle shaped data gaps for hours between 12h and 15h UTC is a result of the changing sun zenith angle. For low sun zenith angles in winter the water vapor retrieval is not applicable for the very Northern region of the model domain leading to the described data gaps.

The next figures (Figures 6.2.7, 6.2.8, 6.2.9, 6.2.10) show results of hourly and monthly resolutions. Note again that MERIS is a sun-synchronous instrument the data acquired at the different UTC times correspond to different areas in the model domain. So the

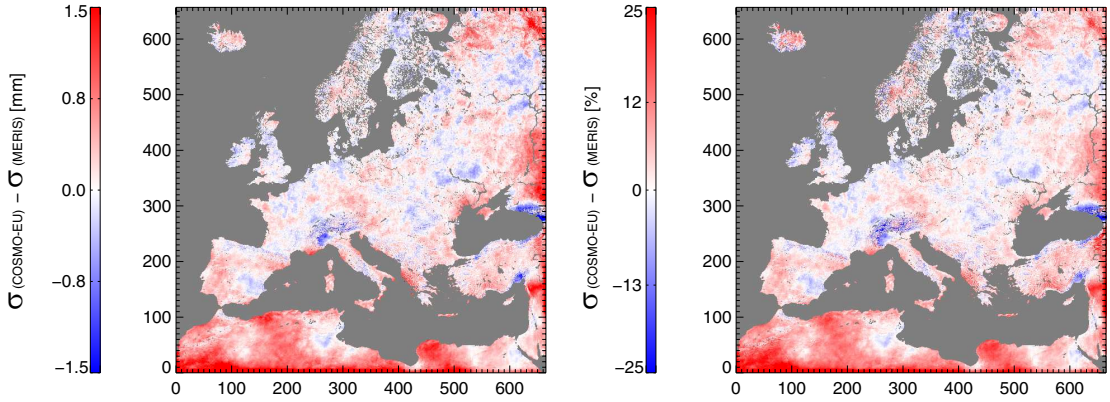

Figure 6.2.5: Differences ($\sigma_{COSMO-EU} - \sigma_{MERIS}$) in variability of IWV. The left image shows the absolute values in millimeters [mm] and the right image the relative values in percentage [%].

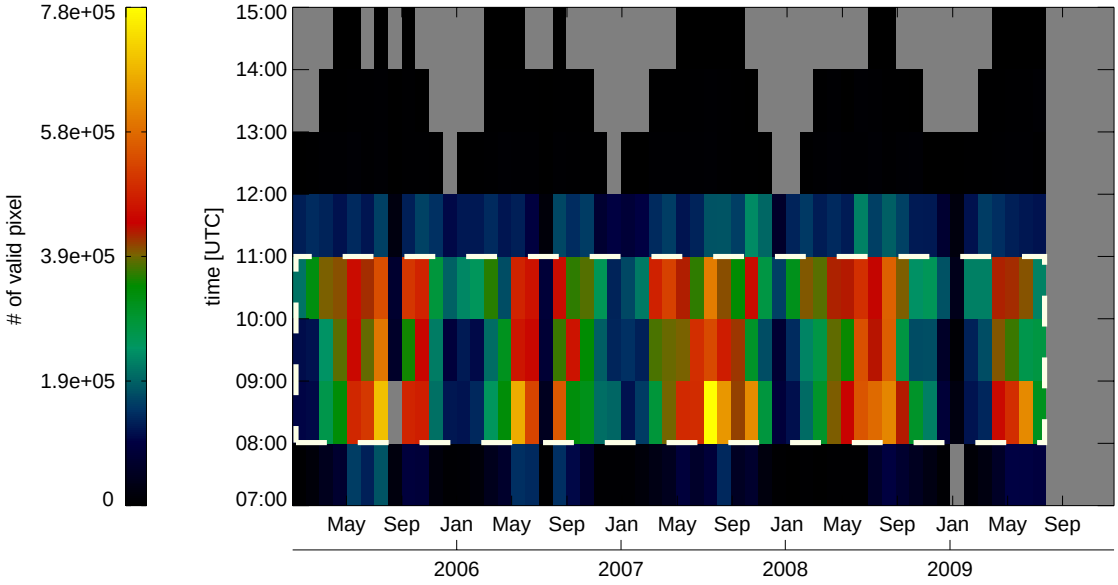

Figure 6.2.6: Hourly and monthly total number of valid cloud free land cases detected in the MERIS and in COSMO-EU dataset. The white dashed square marks the time interval with an adequate number of cases for interpretation.

given variables for each hour represent a particular area of the model domain. The data for the early hours represent the Eastern parts of the domain whereas the late hours represent the Westernmost parts of the model domain. Therefore, the hourly resolved images shows a spatial averaging of the variables rather than a time averaging.

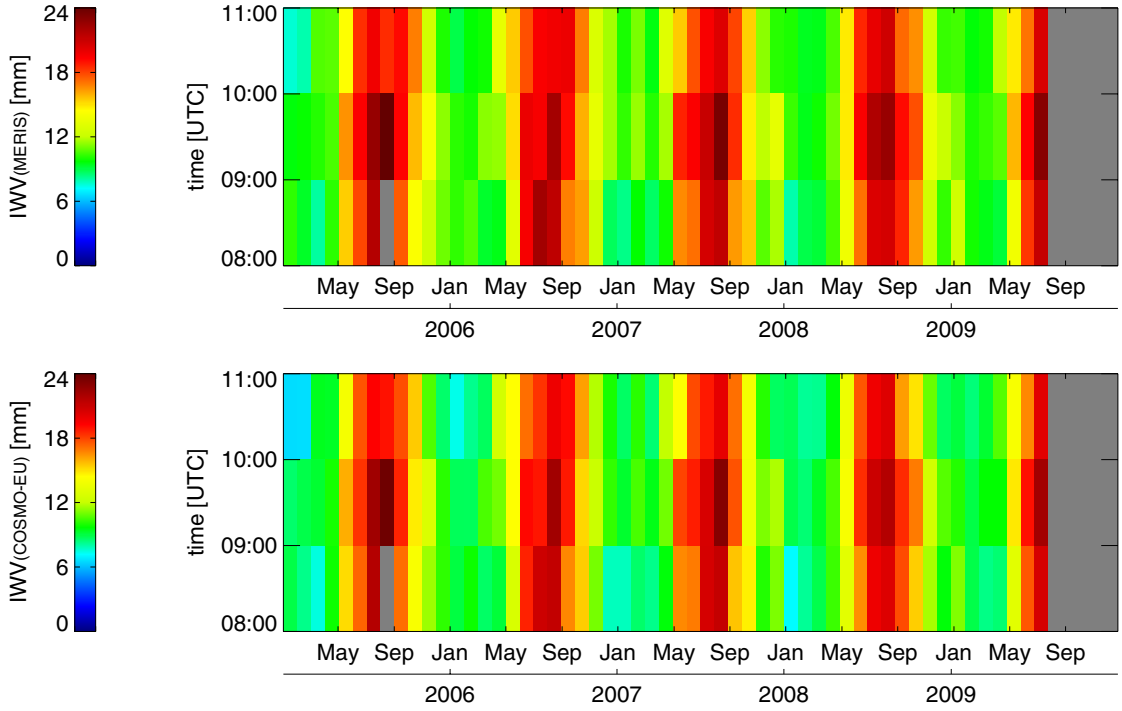

Figure 6.2.7: Hourly and monthly mean of IWV from MERIS (upper) and COSMO-EU (lower). Shown is the region of adequate number of valid cases.

Figure 6.2.7 shows the hourly and monthly averaged integrated water vapor from MERIS and COSMO-EU. The annual cycle of integrated water vapor with low water vapor values in winter increases in spring and a maximum in summer is clearly visible in both datasets. In summer the water vapor values reach up to 25mm for COSMO-EU and MERIS. In winter the MERIS water vapor measurements are slightly higher compared to the COSMO-EU water vapor analyses. The hourly change within the three hours is very weak in both datasets.

Both water vapor datasets show a good agreement between COSMO-EU analyses and MERIS measurements, however the differences between the COSMO-EU and the MERIS water vapor datasets shown in Figure 6.2.8 reveals deviations especially in winter seasons of up to 1.5mm (-15%). In the summer seasons, the deviations are low with up to 0.5mm (5%).

The relative frequency of occurrence of integrated water vapor values, over cloud free land areas, of COSMO-EU and MERIS for 4.5 years is plotted in Figure 6.2.9. The red bars indicate the MERIS dataset and the black bars the COSMO-EU dataset. In

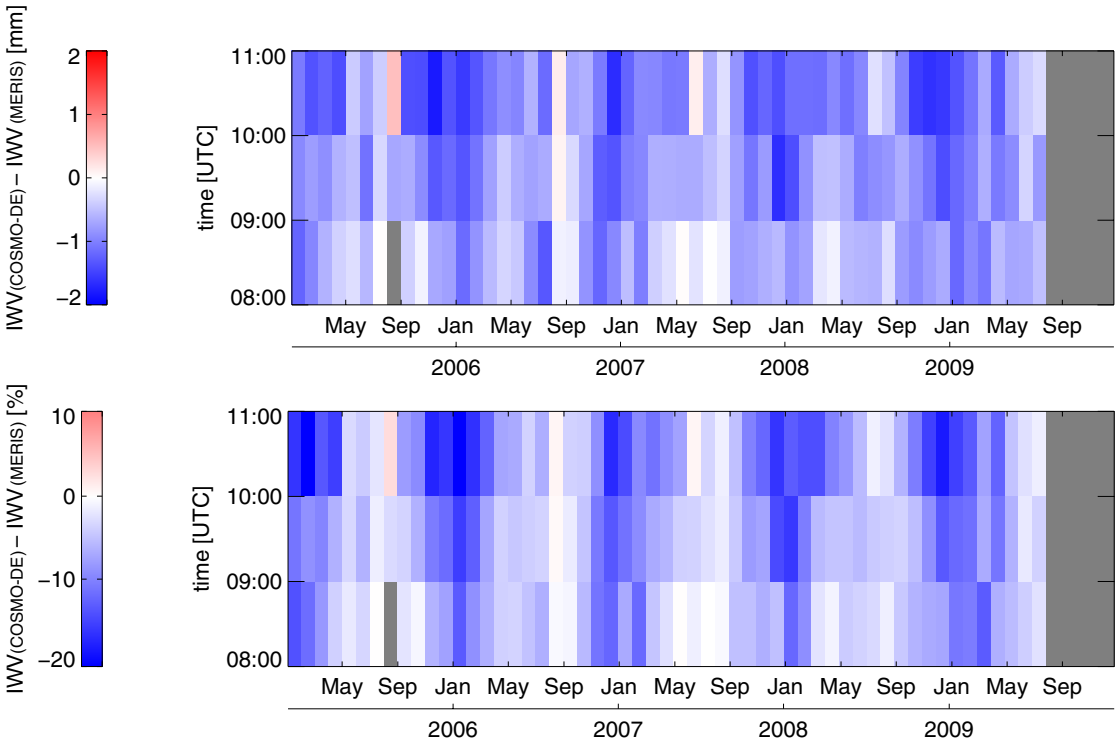

Figure 6.2.8: Differences (COSMO-EU minus MERIS) in the hourly and monthly mean of IWV from MERIS and COSMO-EU. The upper image shows the absolute values in mm and the lower image the relative values in percentage. Shown is the region of adequate number of valid cases.

general an underestimation of the COSMO-EU water vapor analyses to the MERIS measurements is noticeable. The COSMO-EU water vapor analyses show more lower water vapor values of up to 9mm compared to the MERIS water vapor data, whereas for the range of 18mm to 24mm more water vapor values occur within the MERIS dataset. However the differences in the relative frequency distribution is with max 3% weak. For the mean water vapor around 15mm and water vapor values greater than 27mm one can observe a good agreement between the two datasets.

Figure 6.2.10 shows the hourly mean of the datasets. MERIS is indicated by the red line and COSMO-EU by the black line. The error bars shown in the figure denote the standard deviation for the model domain covered at each hour, advising the spatial variations of water vapor. It is noticeable that the error bars as well as the mean water vapor values decrease over time. Since the hourly water vapor means represents a particular area of the model domain (early hours covering the Eastern parts of the model domain and the

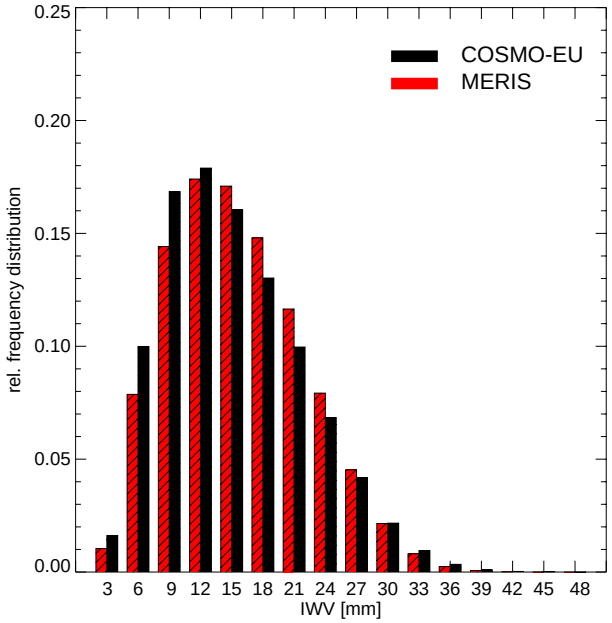

Figure 6.2.9: Relative frequency distribution of integrated water vapor values for MERIS (red) and COSMO-EU (black)

late hours the Western parts) the decrease of water vapor and of the standard deviation with time can be explained by the decreasingly continental climate of Europe. from East to West (6h to 14h UTC). The agreement between both datasets is very good for the hourly means as well as for the standard deviations.

Figure 6.2.11 shows the monthly mean of water vapor values from January 2005 to July 2009. The annual cycle of water vapor is clearly visible. Low water vapor values in winter increasing in spring with a maximum in the summer and decreasing in fall. Typical averaged water vapor values in summer are 20mm and in winter, 9mm. The error bars indicate the standard deviation over the entire COSMO-EU area. The standard deviation range from 5mm to 8mm in summer advising high spatial variations of water vapor. In winter one can find the opposite with values up to 5mm. In comparison with monthly averaged COSMO-EU water vapor values, the MERIS water vapor values are slightly higher in winter. For the summer season both datasets are in a good agreement with differences of not more than to 1mm.

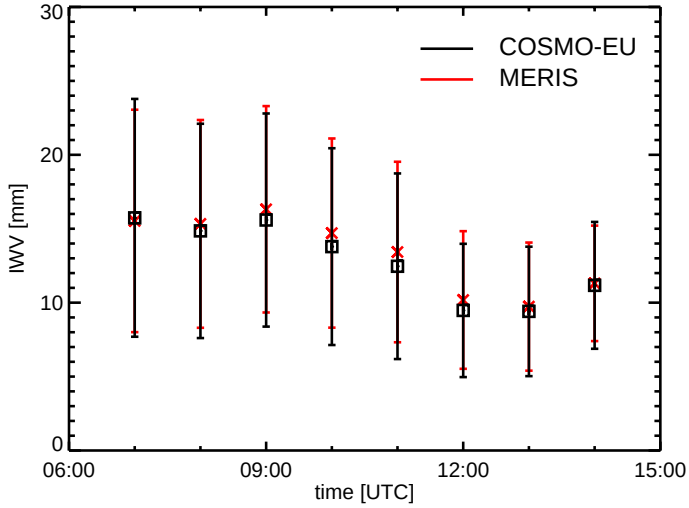

Figure 6.2.10: Hourly mean of IWV for MERIS (red) and COSMO-EU (black) for a period of 4.5 years

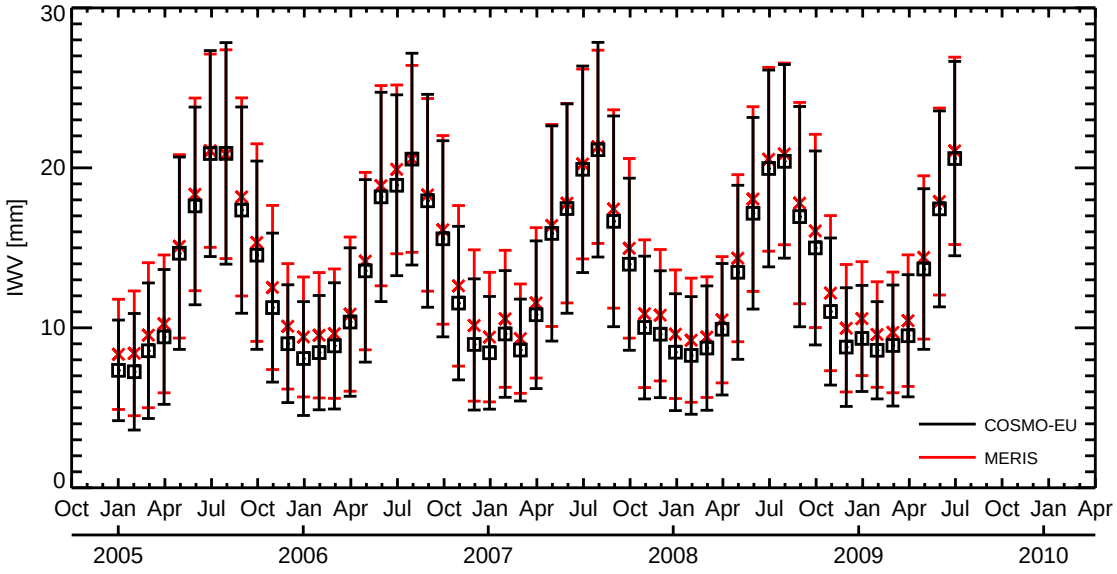

Figure 6.2.11: Monthly mean of IWV data from MERIS (red) and COSMO-EU (black) for a period of 4.5 years

6.3 Comparison of MERIS IWV measurements and COSMO-DE IWV analyses

In this section the results of the comparison of MERIS water vapor measurements with COSMO-DE water vapor analyses are presented. The numerical weather prediction model COSMO-DE is the highest spatial resolution model which is used for operational forecast at the "Deutsche Wetterdienst" with a spacing of 3km x 3km. The model domain covers whole Germany and the Alps.

For the comparison of the MERIS water vapor measurements and COSMO-DE water vapor analyses the preparation of both datasets was performed in the same way as for the COSMO-EU comparison. First the MERIS water vapor measurements were converted into the COSMO-DE grid size then each MERIS dataset was matched up with the COSMO-DE analyses most closely in time. As a result two comparable datasets were produced. Since the COSMO-DE model was introduced in July 2006, the comparison period includes 3 years ranging from July 2006 to July 2009.

The resulting comparable cases (cloud free over land) are shown in Figure 6.3.1. A maximum of 275 cloud free land cases per grid box were detected in areas of the Po Basin. Due to the high spatial resolution of the COSMO-DE grid the orographic structure in the Alps is clearly observable with high numbers of cases detected in the valleys and low cases on the Alp summits. This can be explained by faulty cloud detection over snow covered summits by the MERIS cloud mask algorithm (see section 6.2) leading to more detected cases in the valleys.

Figure 6.3.2 shows the spatial distribution of integrated water vapor for MERIS water vapor measurements (left image) and COSMO-DE water vapor analyses (right image) averaged for each grid box for the period July 2006 to July 2009. A qualitative agreement between the two datasets is observable, low water vapor values in mountain regions like the Alps and low range mountains like the Harz, Thuringian Forest and the Erzgebirge and high values in the Po Basin and parts of the Great Hungarian Plain are observable. The mean water vapor values ranges from 1mm up to 25mm in both datasets.

A quantitative comparison shows differences in water vapor between the two datasets in the order of -1mm to -3mm (-5.7% to -20%) in most areas of the model domain shown in Figure 6.3.3. In these regions the COSMO-DE water vapor analyses are lower compared to the MERIS water vapor measurements. In general an underestimation of COSMO-DE water vapor analyses is shown. For low range mountains small differences are apparent. The variability and the amount of the water vapor differences is high in Alps. The averaging of the MERIS water vapor measurements in region with significantly

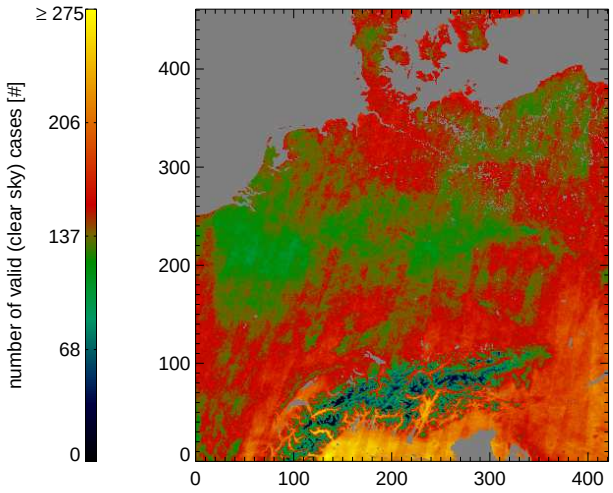

Figure 6.3.1: Total Number of cloud free cases over land detected in the COSMO-DE dataset and in the MERIS dataset for a period 3 years (2006 - 2009)

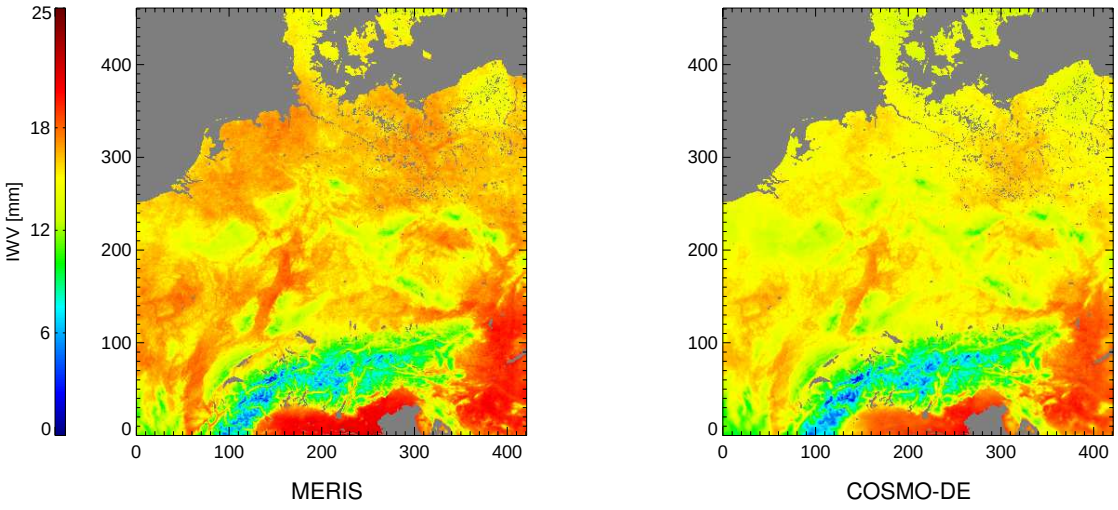

Figure 6.3.2: The mean of integrated water vapor (IWV) for a period of 4 years (2006 -2009) retrieved from MERIS (left) and COSMO-DE (right)

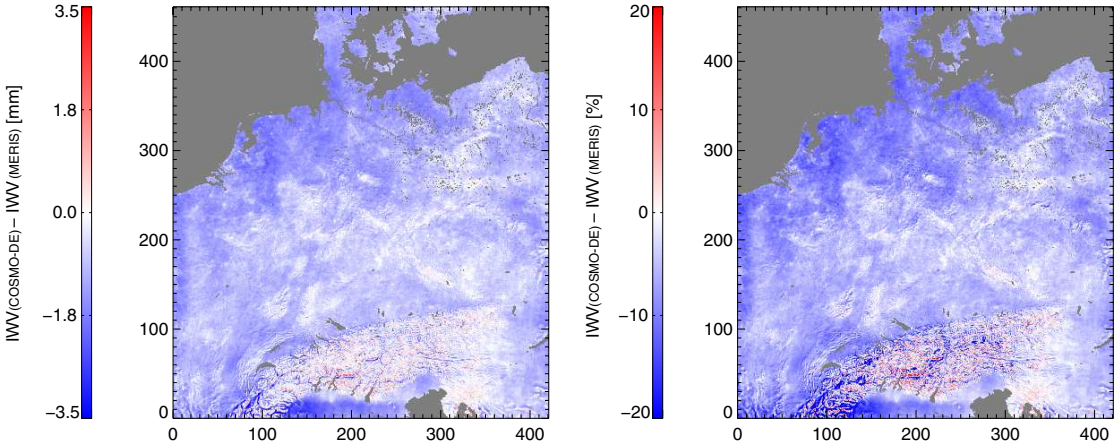

Figure 6.3.3: Differences ($IWV_{COSMO-DE} - IWV_{MERIS}$) of the mean integrated water vapor. The left image shows the absolute values in millimeters [mm] and the right image the relative values in percentage [%]

surface height variation should be avoided, because the integrated water vapor does not decrease linear with the surface height leading to wrong averaged water vapor values. However, the comparison was done with the averaged water vapor values that could have lead to the deviations in the Alps.

Figure 6.3.4 shows the spatial distribution of the variability σ of the MERIS water vapor measurements and COSMO-DE water vapor analyses. The variability σ was calculated for each grid box for a period of 3 years. Most parts of the model domain show a high variability of up to 7mm for MERIS and COSMO-DE. For mountainous regions the variability is low with up to 2mm whereas regions with high water vapor values like the Po basin and parts of the Hungarian lowlands the variability is high with up to 11mm in both datasets.

Figure 6.3.5 shows the differences ($\sigma_{COSMO-DE} - \sigma_{MERIS}$) in variability of integrated water vapor. Differences of up to 1mm (16.6%) in the are shown in central parts of the model domain. In that regions the variability of the COSMO-DE analyses are higher compared to the MERIS dataset. In Switzerland the variability of the COSMO-DE analyses is with -1mm (-16.6%) lower compared to the MERIS water vapor data.

Figure 6.3.6 shows the hourly and monthly total number of valid cases of the investigated datasets. The MERIS overpass time for the center of model domain is between 10h and 11h UTC, a high number of valid cases is shown for that range. For hours between 9h UTC and 12h as well as for 11h UTC and 15h UTC the MERIS flyovers covers only the border areas of the model domain leading to a small amount of valid cases. The

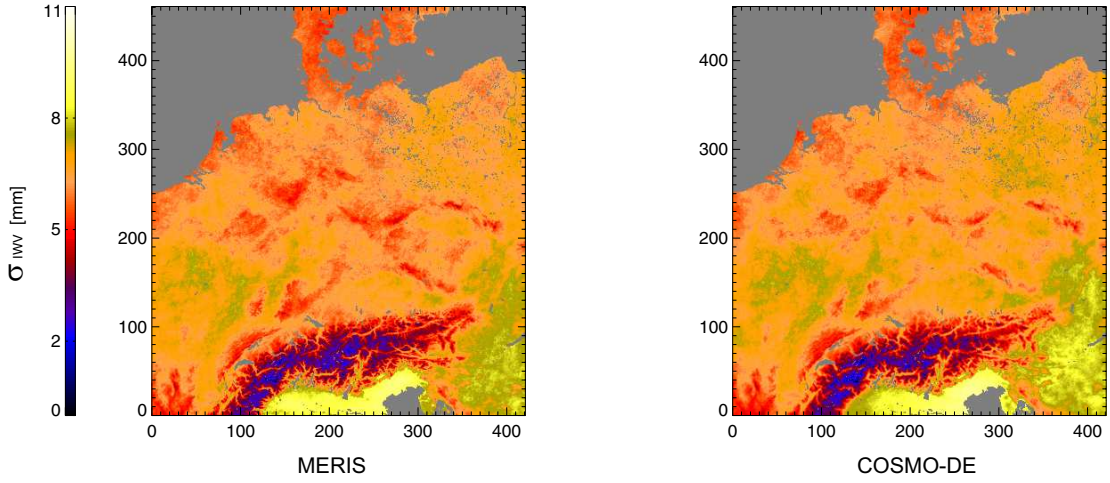

Figure 6.3.4: Variability of integrated water vapor for a period of 4 years (2006 -2009) for MERIS (left) and COSMO-DE (right)

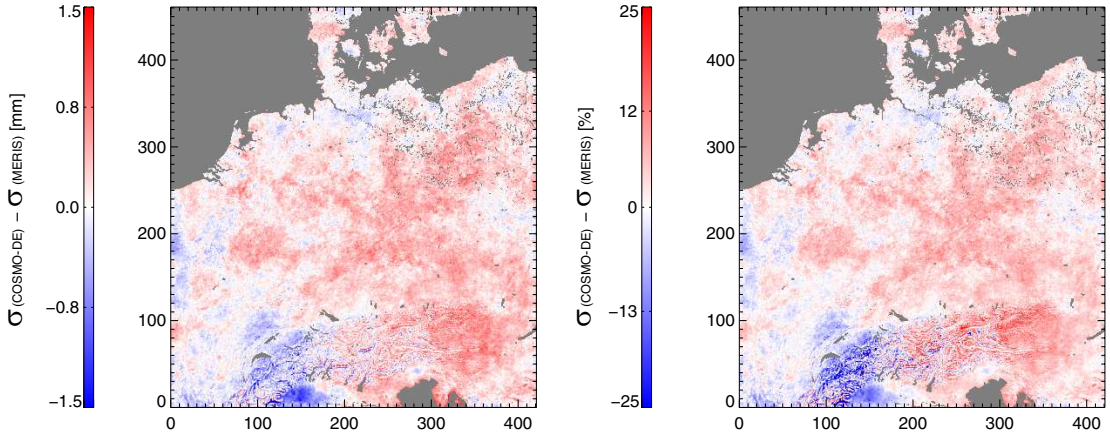

Figure 6.3.5: Differences ($\sigma_{COSMO-DE} - \sigma_{MERIS}$) in variability of integrated water vapor (IWV). The left image shows the absolute values in millimeters [mm] and the right image the relative values in percentage [%].

white square marks the range of an adequate amount of valid cases. Only for this time range the results are interpretable.

In Figure 6.3.7 the hourly/monthly averaged integrated water vapor from MERIS and COSMO-DE is shown. In both datasets the annual cycle of integrated water vapor is clearly visible. Low water vapor values in winter increasing in spring and reaching a maximum in summer are observable. The values of the summer maxima reaches up

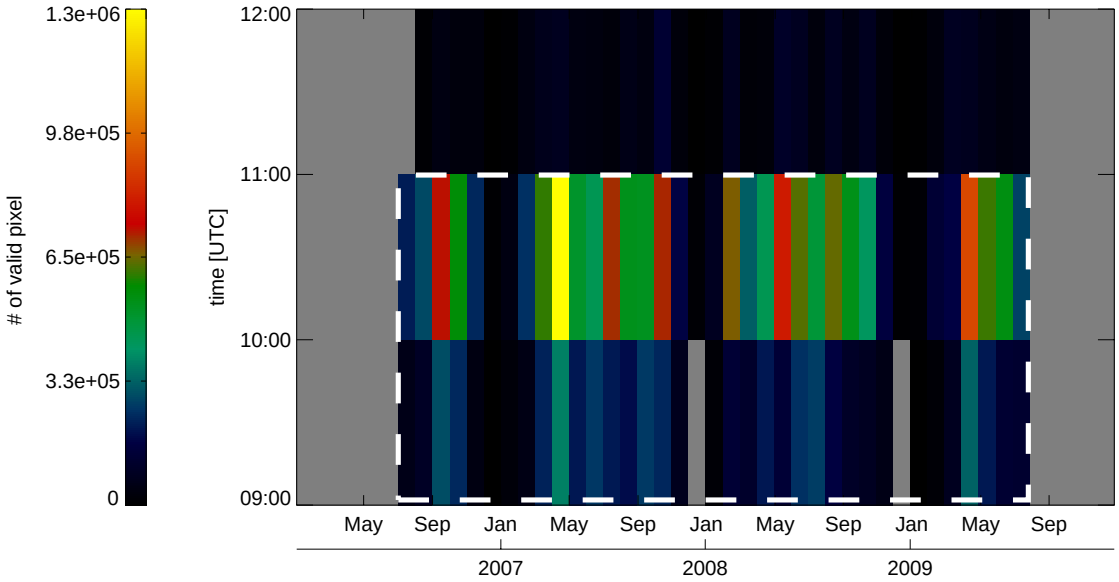

Figure 6.3.6: Hourly and monthly total number of valid cloud free land cases detected in the MERIS and in COSMO-DE dataset. The white dashed square marks the time interval with an adequate number of cases for interpretation.

to 27mm for COSMO-DE and MERIS. The structures in both datasets are in a good agreement.

However differences in the order of about -0.5mm (-5%) are shown in Figure 6.3.8. Generally the mean water vapor values retrieved by MERIS are higher in comparison with the COSMO-DE data. Only for January 2008 and 2009 positive differences are shown, resulting from a small amount of valid cases for that month. A seasonal dependence of the differences in the mean water vapor values is not observable.

The relative frequency distribution of the integrated water vapor analyses of COSMO-DE and MERIS measurements is plotted in Figure 6.3.9. The red bars indicate the MERIS dataset whereas the black bars represents the COSMO-DE dataset. The COSMO-DE water vapor analyses show more low water vapor values of up to 12mm compared to the MERIS water vapor data, whereas for the range of 15mm to 27mm more water vapor values occur within the MERIS dataset.

Figure 6.3.10 shows the hourly mean of the datasets. MERIS is indicated by the red line and COSMO-DE by the black line. The error bars shown in the figure denote the standard deviation for the model domain. The agreement between both datasets is good for the hourly means as well as for the standard deviations. The differences between both datasets increase from 1mm at 9h UTC to 3mm at 11h UTC.

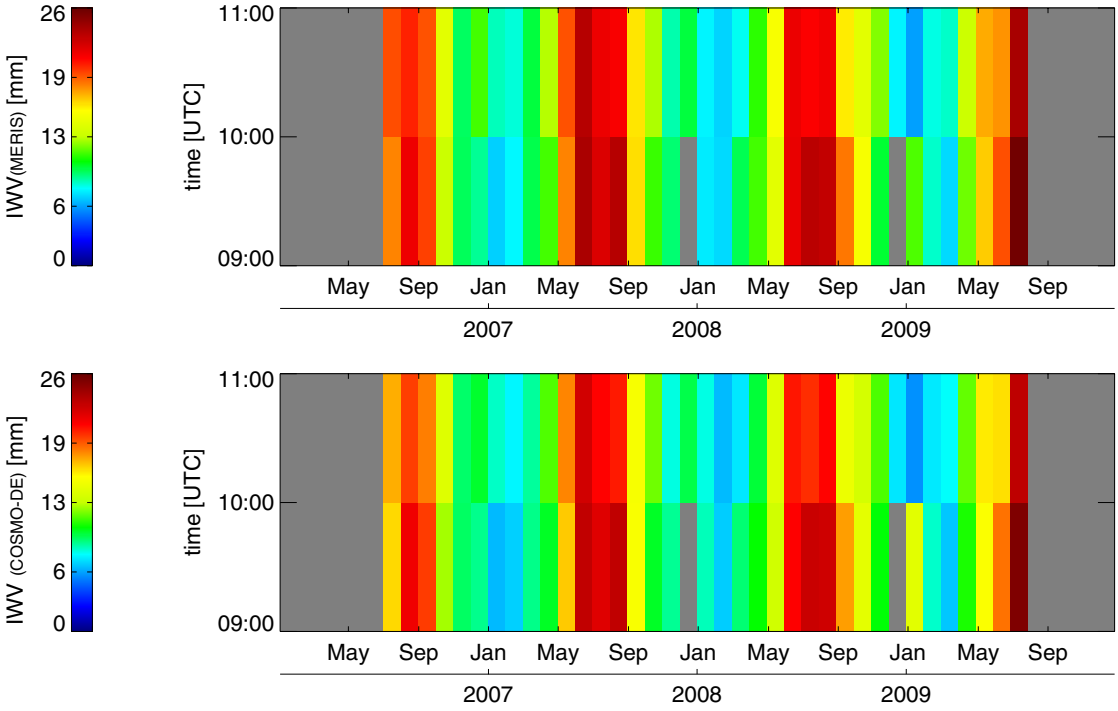

Figure 6.3.7: Hourly and monthly mean of IWV from MERIS (upper) and COSMO-EU (lower). Shown is the region of adequate number of valid cases.

Figure 6.3.11 shows the monthly mean of water vapor values from July 2006 to July 2009. The annual cycle of water vapor is clearly visible. The water vapor amount is low in winter, it increases in spring, reaches a maximum in summer and decreases in fall. Typical averaged water vapor values in summer are 20mm and in winter, 9mm. The error bars indicate the standard deviation over the entire COSMO-DE area. The standard deviation range from 5mm to 8mm in summer showing high spatial variations of water vapor. In winter one can find the opposite with values up to 5mm. The MERIS water vapor values are slightly higher in summer of up to 1mm compared to the mentioned monthly averaged COSMO-DE water vapor analyses. For the winter season both datasets are in a good agreement.

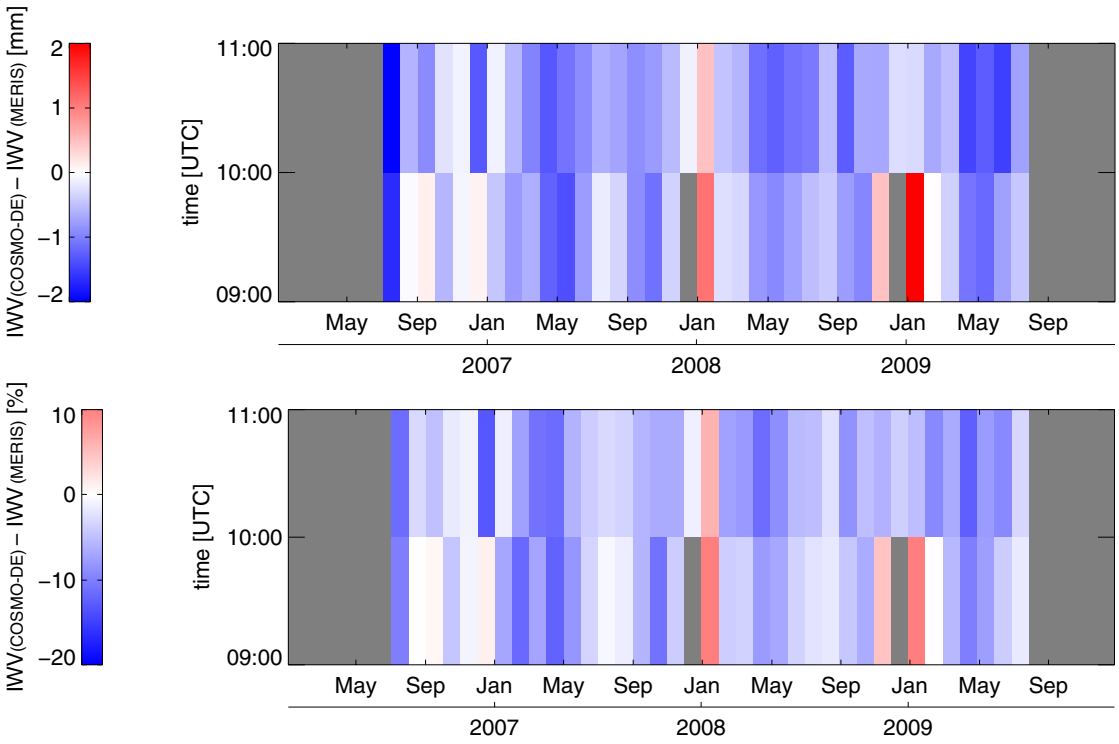

Figure 6.3.8: Differences (COSMO-DE minus MERIS) in the hourly and monthly mean of IWV from MERIS and COSMO-EU. The upper image shows the absolute values in mm and the lower image the relative values in percentage. Shown is the region of adequate number of valid cases.

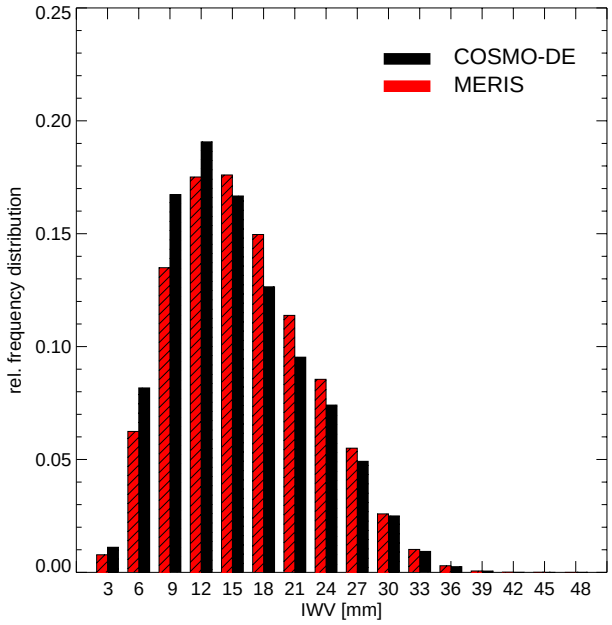

Figure 6.3.9: Relative number of occurrence of IWV from MERIS (red) and COSMO-DE (black)

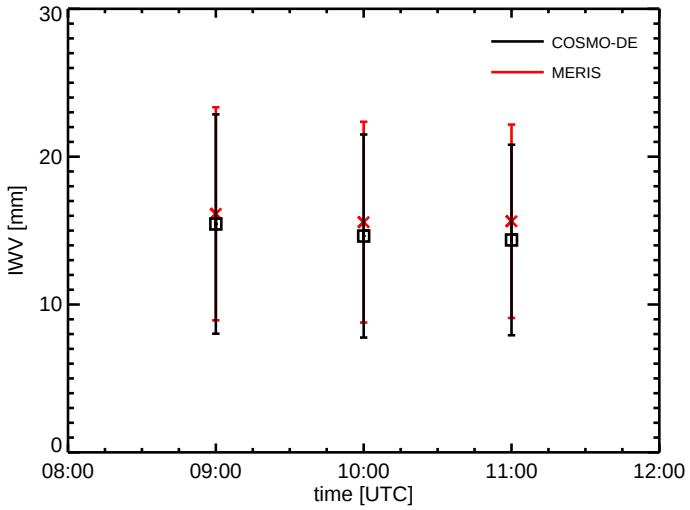

Figure 6.3.10: Hourly mean of IWV for MERIS (red) and COSMO-DE (black) for a period of 3 years

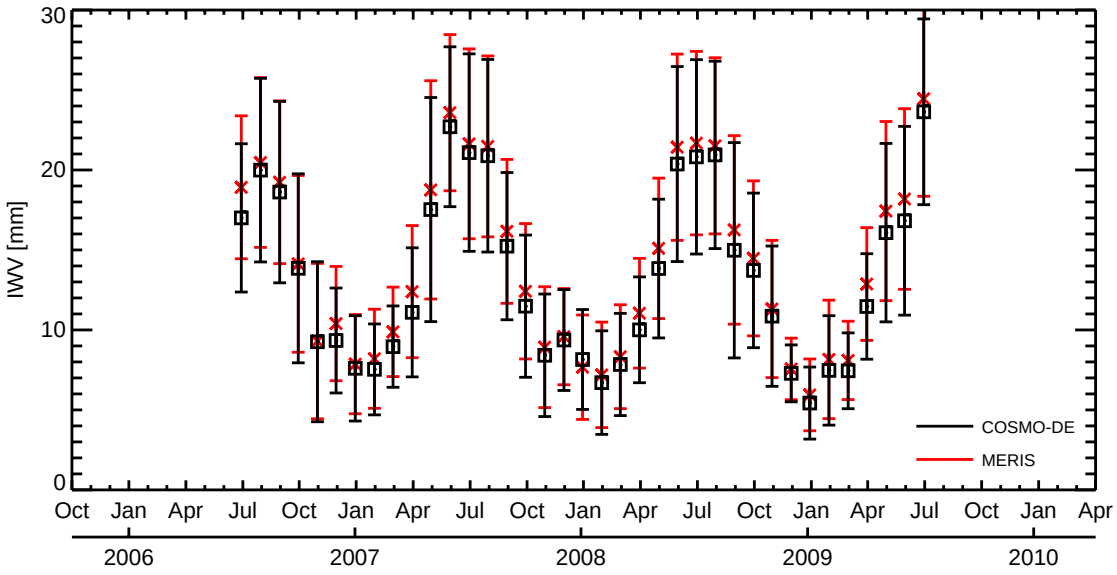

Figure 6.3.11: Monthly mean of IWV data from MERIS (red) and COSMO-DE (black) for a period of 3 years

7 Summary and outlook

Summary: An advanced algorithm for the retrieval of atmospheric integrated water vapor over cloud free land areas is developed. The presented algorithm is for satellite data acquired by the Medium Resolution Imaging Spectrometer (MERIS) on board the polar-orbiting ENVISAT platform. The algorithm is based on the inversion of the radiative transport calculations in the atmosphere by using an artificial neuronal network. The new algorithm accounts for the impact of the spectral variability of the surface reflectance, which is the major improvement compared to the former algorithm (Albert, 2005; Fischer and Bennartz, 1997). The importance of all influencing parameters is demonstrated in sensitivity studies. It is shown that a variability of ±5% in the surface reflectance leads to a 30% uncertainty in the water vapor retrieval. The error produced by an aerosol optical thickness of 0.3 is a 5% uncertainty. A 10% change in the atmospheric pressure leads to a 3.3% error in the retrieved water vapor while a change of ±30K in the atmospheric temperature profile leads to a 2.6% uncertainty in the retrieved water vapor. The errors produced by unknown aerosol optical thickness, vertical temperature and pressure profile are small in comparison to the unknown spectral change in the surface albedo. The improved atmospheric water vapor product is available within the MERIS Level 2 dataset processed by ESA´s ground processor MEGS 8.0 (from 2010 on).

An extensive validation is provided. The new MERIS water vapor product is compared to three different in situ datasets of integrated water vapor measurements: Microwave Radiometers on the ARM-SGP site in Oklahoma / USA; ground based Global Positioning System stations in Germany; and radio soundings over central Europe. The validation is done for a period of three years from January 2003 to December 2005. A high agreement with the data from Microwave Radiometers and the Global Positioning System is found. The root mean square deviation is 1.40mm and the bias is -0.03mm for Microwave Radiometer data. The root mean square deviation is 1.22mm and the bias is 0.97mm for the Global Positioning System. The agreement between MERIS and Radiosonde measurements is good, with a root mean square deviation of 2.28mm and a bias of 1.63mm. The accuracy range of the new retrieval algorithm for water vapor over cloud free land areas is now comparable (in the same magnitude) with the accuracy of

retrievals above open oceans.

Based on the very high accuracy of the presented water vapor algorithm, it is compared to two coupled regional numerical weather prediction models for the first time. The regional weather prediction models are the COSMO-EU and the COSMO-DE of the Deutscher Wetterdienst. The comparison is done for a period of 4.5 years (January 2005 to July 2009) and three years (July 2006 to July 2009) for COSMO-EU and COSMO-DE, respectively. The accuracy is calculated for all valid cloud free match points. The models show the typical annual cycle of water vapor with high water vapor values in summer and low values in winter. Spatial water vapor patterns caused by the orographic/geographic structures are very well resampled by the models. Differences in the mean water vapor of 1 to 2.5mm are found. The mean variability in the water vapor was for both datasets in the order of 6-7mm. In general, the MERIS water vapor is slightly higher and thus the model dryer than the observations. However, there are certain regions, like the Netherlands and north France and northern parts of Germany, with significant differences in the water vapor of up to 20%. Since the models are dryer in these regions in comparison to the MERIS measurements, the differences could be a result of weaknesses in the evaporation and the convective scheme in the COSMO models. Further investigations of these model schemes are necessary to improve the water cycle within the models and therefore the cloud development as well.

Outlook: From both, the excellent validation of the new retrieval algorithm with in situ data and the successful comparison to two regional climate models, one can assume to assimilate the new MERIS water vapor product into climate models. This idea is supported by the continuation of the MERIS measurements by a very similar satellite instrument called the Ocean and Land Color Instrument OLCI. The OLCI sensor will be flown on SENTINEL-3 which is an operational mission scheduled from 2013. Therefore, the outlook of this thesis focuses on a possible assimilation of the new water vapor product into models for numerical weather prediction. The discussion is set into the ongoing and controversial scientific discussion on the assimilation of satellite data into weather models.

Water vapor is one of the key variables in a whole set of prognostic variables in numerical weather prediction models due to its important role in the energy transfer. Different assimilation systems (1D-Var, 3D-Var or 4D-Var) are currently used for different NWP models. The European Center for Medium-Range Weather Forecasts (ECMWF) assimilate directly radiances to their models, using the 4D-Var assimilation method (Courtier et al., 1994). Humidity sensitive data are assimilated from HIRS, AMSU-B, AIRS and

SSM/I on polar orbiting platforms, as well as from the GOES imager, MVIRI and SEVIRI instruments on a number of geostationary platforms (Thépaut, 2003). In addition to this observing system radiance measurements from the SEVIRI water vapor sensitive channels (6.2 and 7.3μm) flying on Meteosat Second Generation (MSG) are used (Szyndel et al., 2005). The Deutsche Wetterdienst uses the 1D-Var and nudging assimilation method. For the regional NWP model systems COSMO-DE and COSMO-EU direct measurements of humidity are assimilated. Since water vapor has a very high temporal and spatial variability, accurate measurements on a high time and spatial resolution are essential for the initialization of NWP models.

The quality of today's numerical weather prediction (NWP) systems is driven by the quality of the data that are used to determine the present state of the atmosphere and the quality of the representation of physical processes in the model Bauer et al. (2007). The present state of the atmosphere in the model are the observations combined with the results from the numerical weather prediction model. This is called an analyses, which is considered to be 'the best' estimate of the current state of the atmosphere. The analyses step balances the uncertainty of the observational data and the numerical forecast.

In 2004, Bengtsson et al. (2004) conclude from an experiment a very limited contribution of humidity observations in general in ECMWF ERA-40 reanalysis (Uppala et al., 2005). The assimilation of observed humidity by satellite in fact led to a more poorly balanced global hydrological cycle.

In contrast to the conclusion of Bengtsson et al. (2004), Andersson et al. (2007) recently showed a significant impact of humidity measurements on the medium range 5 to 6 day forecast of the European Center for Medium-Range Weather Forecasts (ECMWF). A marked impact was also shown for wind and temperature fields. Further, experiments with MERIS water vapor at the ECMWF forecast system during the summer 2006 African Monsoon Multidisciplinary Analysis (AMMA) field campaign period showed a positive impact on forecast accuracy in terms of moisture and dynamics (Bauer, 2009). Due to the extensively developed ECMWF humidity analysis in the recent years, an significant progress with respect to the ERA-40 system has been demonstrated. An improved humidity analysis (Hólm et al., 2002) has been implemented as well as data from several additional instruments from satellites like AMSU-B and AIRS have been introduced. Additionally the humidity physics parametrization for clouds, convection and vertical diffusion have been developed since ERA-40 (Tompkins et al., 2004). Additionally the spatial resolution of NWP models is increasing. Therefore, accurate and high resolution measurements are essential for successful initialization numerical weather prediction models as well as for their validation. This leads to the necessity of accurate

and high resolution global monitoring of water vapor. Both demands are served by the new MERIS water vapor product (by the MERIS satellite instrument).

Zusammenfassung

In der Arbeit wurde ein Algorithmus für die Fernerkundung von integriertem atmosphärischen Wasserdampf über wolkenfreien Landflächen entwickelt. Der vorgestellte Algorithmus verarbeitet Strahldichtemessungen des *Medium Resolution Imaging Spectrometer* (MERIS) an Bord des polar-umlaufenden ENVISAT Satelliten. Der Algorithmus für die Fernerkundung von Wasserdampf basiert auf der Umkehrung von Strahlungstransportberechnungen in der Atmosphäre mit Hilfe eines künstlichen Neuronalen Netzes. Der neue Algorithmus berücksichtigt zusätzlich den spektralen Ganges der Bodenalbedo, welches die wesentliche Verbesserung gegenüber den früheren Algorithmus Albert (2005); Fischer and Bennartz (1997) darstellt.

Der Einfluss des spektralen Ganges der Bodenalbedo, der aerosoloptischen Dicke und des Aerosoltyps sowie des vertikalen Druck- und Temperaturprofiles auf die Genauigkeit des Wasserdampf Algorithmus wurde mit Hilfe von Sensitivitätstudien berechnet. Es wurde gezeigt dass eine Änderung der spektralen Bodenalbedo um ±5% zwischen 885nm und 900nm zu einer 30 prozentigen Ungenauigkeit des abgeleiteten Wasserdampfes. Der Einfluss von Aerosolen auf die Genauigkeit des Algorithmus war gering. Eine aerosol optische Dicke von 0,3 führte zu einer 5 prozentigen Unsicherheit des abgeleiteten Wasserdampfes. Ebenso gering war der Einfluss des vertikalen Druck- und Temperaurprofiles auf die Genauigkeit des Algorithmus. Eine ±10 prozentige Änderung des atmosphärischen Drucks führte zu einem 3,3 prozentigen Fehler im abgeleiteten Wasserdampf, während eine Änderung der im atmosphärische Temperatur-Profil um ±30K zu einer Unsicherheit von 2,6% führte. Der verbesserte Algorithmus zur Ableitung integrierten atmosphärischen Wasserdampfes wird ab 2010 innerhalb des ESA-Boden-Prozessor MEGS 8.0 eingesetzt werden.

Der neue Algorithmus wurde umfassend validiert. Dafür wurde das neue MERIS Wasserdampf Produkt mit drei verschiedenen unabhängigen bodengestützten Wasserdampf Datensätze verglichen. Erstens mit Mikrowellenradiometer der ARM-SGP site in Oklahoma / USA. Zweitens mit bodengestützten *Global Positioning System*-Stationen in Deutschland und mit Radiosondenaufstiegen über Mitteleuropa. Die Validierung wurde für einen Zeitraum von drei Jahren von Januar 2003 bis Dezember 2005 durchgeführt.

Es zeigte sich eine hohe Übereinstimmung der MERIS Wasserdampf Daten mit den Daten aus Mikrowellenradiometer und des Global Positioning System. Für den Vergleich von MERIS Wasserdampfdaten und Mikrowellen Radiometer Daten wurde ein rmse von 1.40mm und ein bias von -0.03mm festgestellt. Ein rmse von 1,22 mm und ein bias von 0,97 mm wurde für den Vergleich mit Wasserdampfdaten des Global Positioning System berechnet. Die Übereinstimmung zwischen MERIS und Radiosonden Wasserdampfmessungen ist gut. Es wurde ein rmse von 2.28mm und bias von 1.63mm berechnet. Die Genauigkeit des neuen Algorithmus zur Fernerkundung von integriertem Wasserdampf über wolkenfreien Landflächen ist jetzt vergleichbar mit der Genauigkeit der Wasserdampf Fernerkundung über offenen Ozean.

Basierend auf der sehr hohen Genauigkeit des präsentierten Wasserdampf Algorithmus wurden Wasserdampfdaten erstmalig mit denen von zwei gekoppelten regionalen numerischen Wettervorhersagemodellen verglichen. Die regionalen Wettervorhersagemodelle sind das COSMO-EU Modell und das COSMO-DE Modell des Deutschen Wetterdienst. Der Vergleich wurde für einen Zeitraum von 4,5 Jahren (Januar 2005 bis Juli 2009 durchgeführt) für COSMO-EU bzw von drei Jahren (Juli 2006 bis Juli 2009) für COSMO-DE durchgeführt. Die Modelle zeigen den typischen Jahresgang des Wasserdampfes mit hohen Wasserdampfwerten im Sommer und niedrigen Wasserdampfwerten im Winter. Räumliche Muster im Wasserdampffeld verursacht durch orographische / geografischen Gegebenheiten, sind sehr gut in den Modellen wiedergegeben. Unterschiede von 1 bis 3,5 mm (5% bis 20%) zwischen Modellanalyse und MERIS Messungen sind erkennbar. Die Unterschiede liegen in der Größenordnung der Messgenauigkeit des neuen MERIS Wasserdampfproduktes. Im Allgemeinen sind die MERIS Wasserdampfmessungen etwas höher und damit das Modell trockener als die Beobachtungen. Die mittlere Variabilität des Wasserdampfes beträgt für beide Datensätze 6-7mm.

List of Figures

List of Tables

Bibliography

Albert, P., 2005: *Remote sensing of atmospheric water vapour for numerical weather prediction*. Ph.D. thesis, Fachbereich Geowissenschaften, Freie Universität Berlin.

Andersson, E., E. Holm, P. Bauer, A. Bejaars, G. A. Kelly, A. P. McNally, A. J. Simmons, J. N. Thepaut, and A. M. Tompkins, 2007: Analysis and forecast impact of the main humidity observing systems. *Quarterly Journal of the Royal Meteorological Society*, **133**, 1473–1485, doi:10.1002/qj.112.

Baldauf, M., J. Förstner, S. Klink, T. Reinhardt, C. Schraff, A. Seifert, and K. Stephan, 2009: Kurze Beschreibung des Kokal-Modells Kürzestfrist COSMO-DE (LMK) und seine Datenbanken auf den Datenservern des DWD. *Deutscher Wetterdienst*.

Baldridge, A., S. Hook, C. Grove, and G. Rivera, 2009: The aster spectral library version 2.0. *Remote Sensing of Environment*, **113**, 711 – 715, doi:DOI: 10.1016/j.rse.2008.11.007.

Bauer, P., 2009: 4d-var assimilation of meris total column water-vapour retrievals over land. *Quarterly Journal of the Royal Meteorological Society*, **135**, 1852–1862.
URL `http://dx.doi.org/10.1002/qj.509`

Bauer, P., P. Lopez, E. Moreau, F. Chevallier, A. Benedetti, and M. Bonazzola, 2007: The european centre for medium-range weather forecasts global rainfall data assimilation experimentation.
URL `http://dx.doi.org/10.1007/978-1-4020-5835-6_35`

Bengtsson, L., K. Hodges, and S. Hagemann, 2004: Sensitivity of large-scale atmospheric analyses to humidity observations and its impact on the global water cycle and tropical and extratropical weather systems in era40. *Tellus Series A: Dynamic Meteorology and Oceanography*, **56**, 202–217.

Bennartz, R. and J. Fischer, 2000: A modified k-distribution approach applied to narrow band water vapour and oxygen absorption estimates in the near infrared. *Journal of Quantitative Spectroscopy and Radiative Transfer*, **66**, 539–553.

Bennartz, R. and R. Preusker, 2006: Representation of the photon pathlength distribution in a cloudy atmosphere using finite elements. *Journal of Quantitative Spectroscopy and Radiative Transfer*, **98**, 202–219.

Bolton, D., 1980: The computation of equivalent potential temperature. *Monthly Weather Review*, **108**, 1046–1053.

Courtier, P., J.-N. Thépaut, and A. Hollingsworth, 1994: A strategy for operational implementation of 4d-var, using an incremental approach. *Quarterly Journal of the Royal Meteorological Society*, **120**, 1367–1387.
URL `http://dx.doi.org/10.1002/qj.49712051912`

Delmas, R., G. Megie, and V. H. Peuch, 2005: *Physique et chimie de l'atmosphere*. ECHELLES, Belin, 640 pp.

Delwart, S., R. Preusker, L. Bourg, R. Santer, D. Ramon, and J. Fischer, 2007: Meris in-flight spectral calibration. *International Journal of Remote Sensing*, **28**, 479–496, doi:10.1080/01431160600821119.

Doms, G. and U. Schättler, 2002: A discribtion of the nonhydrostatic regonal model lm. *Deutscher Wetterdienst*, **Part I - Dynamics and Numerics**.

Doms, G., U. Schättler, E. Heise, H.-J. Herzog, M. Raschendorfer, R. Schrodin, T. Reinhardt, and G. Vogel, 2002: A discribtion of the nonhydrostatic regonal model lm. *Deutscher Wetterdienst*, **Part II - Physical Parameterization**.

Fell, F. and J. Fischer, 2001: Numerical simulation of the light field in the atmosphere-ocean system using the matrix-operator method. *Journal of Quantitative Spectroscopy and Radiative Transfer*, **69**, 351–388.

Field, P., R. Hogan, P. Brown, A. Illingworth, T. Choularton, and R. Cotton, 2005: Parametrization of ice-particle size distributions for mid-latitude stratiform cloud. *Quarterly Journal of the Royal Meteorological Society*, **131**, 1997–2017, doi:10.1256/qj.04.134.

Fischer, J., 1988: High resolution spectroscopy for remote sensing of physical cloud properties and water vapour. *Current Problems in Atmospheric Radiation, ED. Lenoble and Geleyn, Deepak Publishing*, 151–156.

Fischer, J. and R. Bennartz, 1997: *Retrieval of total water vapour content from MERIS measurements*. ESA-ESTEC.

Fischer, J. and H. Grassl, 1991: Detection of cloud-top height from backscattered radiances within the oxygen-a-band. part 1: Theoretical study. *Journal of Applied Meteorology*, **30**, 1245–1259.

Gao, B.-C., A. F. H. Goetz, E. R. Westwater, J. E. Conel, and R. O. Green, 1993: Possible near-ir channels for remote sensing precipitable water vapor from geostationary satellite platforms. *Journal of Applied Meteorology*, **32**, 1791–1801.

Gao, B.-C. and Y. J. Kaufman, 2003: Water vapor retrievals using moderate resolution imaging spectroradiometer (modis) near-infrared channels. *Journal of Geophysical Research (Atmospheres)*, **108**, 4–1, doi:10.1029/2002JD003023.

Gendt, G., G. Dick, C. Reigber, M. Tomassini, Y. Liu, and M. Ramatschi, 2004: Near real time gps water vapor monitoring for numerical weather prediction in germany. *Journal of the Meteorological Society of Japan*, **82**, 361–370.

Han, Y. and E. Westwater, 1995: Remote sensing of tropospheric water vapor and cloud liquid water by integrated ground-based sensors. *Journal of Atmospheric and Oceanic Technology*, **12**, 1050–1059.

Hólm, E., E. Andersson, A. Beljaars, P. Lopez, J.-F. Mahfouf, A. Simmons, and J. Thépaut, 2002: Assimilation and modeling of the hydrological cycle: Ecmwf's status and plans. Technical report, ECMWF Tech. Memo. 383.

IPCC, ., 2001: Climate change 2001: The scientific basis contribution of working group to the third assessment report of ipcc, ISBN: 0521014956.

— 2007: Climate change 2007: The physical science basis. contribution of working group i to the fourth assessment report of the intergovernmental panel on climate change, 996.
URL `http://ipcc-wg1.ucar.edu/wg1/wg1-report.html`

Kiehl, J. T. and K. E. Trenberth, 1997: Earth's annual global mean energy budget. *Bulletin of the American Meteorological Society*, **78**, 197–197.

Liljegren, J., 2000: Automatic self-calibration of arm microwave radiometers. *Microwave Radiometry and Remote Sensing of the Earths Surface and Atmosphere*, 433–443.

Lindstrot, R., R. Preusker, and J. Fischer, in press: The empirical correction of stray light in the MERIS oxygen A band channel. *J. Atmos. Oceanic Technol.*.

Liou, K. N., 2002: *An Introduction to Atmospheric Radiation*. Academic Press, Hampton, USA, second edition.

Miloshevich, L., H. Vömel, D. Whiteman, and T. Leblanc, 2009: Accuracy assessment and correction of vaisala rs92 radiosonde water vapour measurements. *Journal of Geophysical Research*, **114**, doi:10.1029/2008JD011565.

Muller, J.-P., R. Preusker, J. Fischer, M. Zuhlke, C. Brockmann, and P. Regner, 2007: ALBEDOMAP: MERIS land surface albedo retrieval using data fusion with MODIS BRDF and its validation using contemporaneous EO and in situ data products, 2404–2407. doi:10.1109/IGARSS.2007.4423326.

Nakicenovic, N., J. Alcamo, G. Davis, J. F. Bert de Vries, S. Gaffin, K. Gregory, T. Y. J. Arnulf Grübler, T. Kram, E. L. L. Rovere, S. M. Laurie Michaelis, T. Morita, W. Pepper, H. Pitcher, L. Price, K. Riahi, A. Roehrl, H.-H. Rogner, A. Sankovski, M. Schlesinger, P. Shukla, R. S. Steven Smith, S. van Rooijen, N. Victor, and Z. Dadi, 2000: Ipcc special report emissions scenarios: Summary for policymakers: A special report of ipcc working group iii.

Plass, G. N., G. W. Kattawar, and F. E. Catchings, 1973: Matrix operator theory of radiative transfer. 1: Rayleigh scattering. *Applied Optics*, **12**, 314–329.

Ramanathan, V., B. R. Barkstrom, and E. F. Harrison, 1989: Climate and the earth's radiation budget. *Physics Today*, **42**, 22–33.

Rothman, L. S., A. Barbe, D. C. Benner, L. R. Brown, C. Camy-Peyret, M. R. Carleer, K. Chance, C. Clerbaux, V. Dana, V. M. Devi, A. Fayt, J. M. Flaud, R. R. Gamache, A. Goldman, D. Jacquemart, K. W. Jucks, W. J. Lafferty, J. Y. Mandin, S. T. Massie, V. Nemtchinov, D. A. Newnham, A. Perrin, C. P. Rinsland, J. Schroeder, K. M. Smith, M. A. H. Smith, K. Tang, R. A. Toth, J. V. Auwera, P. Varanasi, and K. Yoshino, 2003: The hitran molecular spectroscopic database: edition of 2000 including updates through 2001. *Journal of Quantitative Spectroscopy and Radiative Transfer*, **82**, 5 – 44, doi:DOI: 10.1016/S0022-4073(03)00146-8, the HITRAN Molecular Spectroscopic Database: Edition of 2000 Including Updates of 2001.
URL `http://www.sciencedirect.com/science/article/B6TVR-48J4JXW-3/2/8504902b8508db3e20bd99ccf97b4224`

Rumelhart, D. E., G. E. Hinton, and R. J. Williams, 1986: Learning representations by back-propagating errors. *Nature*, **323**, 533–536, doi:10.1038/323533a0.

Santer, R., F. Zagolski, D. Ramon, J. Fischer, and P. Dubuisson, 2005: Uncertainties in radiative transfer computations: consequences on the meris products over land. *International Journal of Remote Sensing*, **26**, 4597 – 4626.

Schluessel, P. and W. J. Emery, 1990: Atmospheric water vapour over oceans from ssm/i measurements. *International Journal of Remote Sensing*, **No. 5**, 753–766.

Schraff, C. and R. Hess, 2003: A discribtion of the nonhydrostatic regonal model lm. *Deutscher Wetterdienst*, **Part III - Data Assimilation**.

Schulz, J.-P. and U. Schättler, 2009: Kurze beschreibung des kokal-modells europa cosmo-eu (lme) und seine datenbanken auf den datenservern des dwd. *Deutscher Wetterdienst*.

Soden, B. J., R. T. Wetherald, G. L. Stenchikov, and A. Robock, 2002: Global cooling after the eruption of mount pinatubo: A test of climate feedback by water vapor. *Science*, **296**, 727–730.

Sohn, B.-J. and E. A. Smith, 2003: Explaining sources of discrepancy in ssm/i water vapor algorithms. *Journal of Climate*, **16**, 3229–3255.
URL `http://adsabs.harvard.edu/cgi-bin/nph-bib_query?bibcode=2003JCli...16.3229S&db_key=PHY`

Starr, D. and S. H. Melfi, 1991: The role of water vapour in climate, a strategic research plan for the proposed gewex water vapour project (gvap). *NASA Conference Publication*, **3210**, 60 pp.

Szyndel, M. D. E., G. Kelly, and J. Thépaut, 2005: Evaluation of potential benefit of assimilation of seviri water vapour radiance data from meteosat-8 into global numerical weather prediction analyses. *Atmospheric Science Letters*, **6**, 105–111.
URL `http://dx.doi.org/10.1002/asl.98`

Thépaut, J.-N., 2003: Satellite data assimilation in numerical weather prediction: an overview. *ECMWF Seminar on Recent Developments in Data Assimilation for Atmosphere and Ocean*, 75–96.

Tompkins, A., P. Bechtold, A. Beljaars, A. Benedetti, S. Cheinet, M. Janisková, M. Köhler, P. Lopez, and J.-J. Morcrette, 2004: Moist physical processes in the ifs: Progress and plans. Technical report, ECMWF Technical Memo No.452.

Trenberth, K. E., J. Fasullo, and L. Smith, 2005: Trends and variability in column-integrated atmospheric water vapor. *Climate Dynamics*, **24**, 741–758, doi:10.1007/s00382-005-0017-4.

Trenberth, K. E. and D. P. Stepaniak, 2003: Seamless poleward atmospheric energy transports and implications for the hadley circulation. *Journal of Climate*, **16**, 3706–3722.
URL `http://dx.doi.org/10.1175%2F1520-0442%282003%29016%3C3706%3ASPAETA%3E2.0.CO%3B2`

Turner, D. D., B. M. Lesht, S. A. Clough, J. C. Liljegren, H. E. Revercomb, and D. C. Tobin, 2003: Dry bias and variability in vaisala rs80-h radiosondes: The arm experience. *Journal of atmospheric and oceanic technology*, **vol. 20, no1**, 117–132.

Uppala, S., P. Kallberg, A. Simmons, U. Andrae, V. Bechtold, M. Fiorino, J. Gibson, J. Haseler, A. Hernandez, G. Kelly, X. Li, K. Onogi, S. Saarinen, N. Sokka, R. Allan, E. Andersson, K. Arpe, M. Balmaseda, A. Beljaars, L. Van De Berg, J. Bidlot, N. Bormann, S. Caires, F. Chevallier, A. Dethof, M. Dragosavac, M. Fisher, M. Fuentes, S. Hagemann, E. Holm, B. Hoskins, L. Isaksen, P. Janssen, R. Jenne, A. McNally, J. Mahfouf, J. Morcrette, N. Rayner, R. Saunders, P. . Simon, A. Sterl, K. Trenberth, A. Untch, D. Vasiljevic, P. Viterbo, and J. Woollen, 2005: The ERA-40 re-analysis. *Quarterly Journal of the Royal Meteorological Society*, **131**, 2961–3012, doi:10.1256/qj.04.176.

Vömel, H., H. Selkirk, L. Miloshevich, J. Valverde, J. Valdés, E. Kyrö, R.Kivi, W. Stolz, G. Peng, and J. A. Diaz, 2007: Radiation dry bias of the vaisala rs92 humidity sensor. *Journal of Atmospheric and Oceanic Technology*, **24**, 953–963.

Vonder Haar, T., J. Forsythe, J. Luo, D. Randel, and S. Woo, 2005: Water vapor trends and variability from the global nvap dataset. *16th Symposium on Global Change and Climate Variations*.

Acknowledgments

This thesis would not have been possible without the help and support of many people. I would like to thank all the people, that were involved in the realization of this work.

First of all I would like to express my first supervisor Prof. Dr. Jürgen Fischer, who enabled me to work on this topic. I am very grateful for his interest in and support of this work for his patience and flexibility. Furthermore I like to thank Prof. Dr. Ralf Bennartz for agreeing to be my second supervisor and for reviewing this thesis.

Many thanks go to all present and former colleagues at the Institute for Space Sciences in Berlin. I like to sincerely thank Dr. Rene Preusker, Dr. Peter Albert, Dr. Maximilian Reuter and Dr. Rasmus Lindstrot for fruitful discussions, useful suggestions, support and attendance. I would like to thank Gerald Paul for collaborating in the model intercomparisons and for proving unbureaucratic help and fast access to the database of Deutsche Wetterdienst.

Many friends helped me through the years. Special thanks to Dr. Kerstin Ebert for tons of moral support and for keeping me grounded all the time. I would like to thank Henrik Lehmann and Markus Korn for the necessary distraction. Furthermore I would like to thank Stefan Wagner and Lionel Doppler and for thousand of street kilometers on racing bike.

Zu guter Letzt möchte ich mich ganz besonders bei meinen Eltern Cornelia und Peter Leinweber bedanken für die uneingeschränkte und überaus großzügige Unterstützung in all den Jahren. Vielen Vielen DANK!!!

Selbstständigkeitserklärung

Hiermit erkläre ich, Ronny Leinweber, die vorliegende Arbeit ohne fremde Hilfe verfasst und nur die angegebene Literatur und die angegebenen Hilfsmittel verwendet zu haben.

Ort, Datum	Unterschrift